ROYAUME DU MAROC
Université Mohammed V - RABAT -
جامعة محمد الخامس – الرباط –
Faculté des sciences
كلية العلوم
CENTRE D'ETUDES DOCTORALES - SCIENCES ET TECHNOLOGIES

Order number: 3571

THESIS

In order to obtain: ***Doctorate degree***

Research center: *Energy*
Research structure: *Laboratory of Materials and Nanomaterials for Photovoltaic and Electrochemical Storage (MANAPSE)*
Discipline: *Chemistry*
Specialty: *Materials Science - Energy*

Presented and defended on 21/12/2021 by:

Siham IDRISSI

Investigation of tin phosphite $SnHPO_3$ based materials as new anode for Li-ion batteries and doped-reduced graphene oxide as catalysts for oxygen reduction reaction

JURY

Mohammed ABD-LEFDIL	PES, Faculty of Sciences, Mohammed V University in Rabat	President
M'Hamed TAIBI	PES, Higher Normal School, Mohammed V University in Rabat	Reviewer/Examiner
Bouchaib MANOUN	PES, Faculty of Sciences and Techniques, Hassan I University in Settat	Reviewer/Examiner
Mohamed SAADI	PES, Faculty of Sciences, Mohammed V University in Rabat	Reviewer/Examiner
Carlos PEREZ VICENTE	PES, University of Cordoba in Spain	Examiner
M'Hamed OUBLA	PA, Faculty of Sciences, Mohammed V University in Rabat	Invited
Zineb EDFOUF	PES, Faculty of Sciences, Mohammed V University in Rabat	Thesis Co-director
Fouzia CHERKAOUI EL MOURSLI	PES, Faculty of Sciences, Mohammed V University in Rabat	Thesis Director

Academic year: 2020-2021

Acknowledgement

The work presented in this manuscript was carried out within the research structure "Matériaux et Nanomatériaux pour le Photovoltaïque et le Stockage Electrochimique (MANAPSE)" at the Faculty of Sciences of Rabat, under the supervision of Professor CHERKAOUI EL MOURSLI Fouzia, and the co -supervision of Professor EDFOUF Zineb.

First of all, I would like to express my sincere gratitude to my supervisor Professor CHERKAOUI EL MOURSLI FOUZIA for welcoming me into her group, supervising and encouraging me throughout all of these years of my PhD research. I have been extremely lucky to have a supervisor who cared so much about my work, and who responded to my questions and queries so promptly. I would like also to acknowledge her for her tremendous help, expert guidance in the field of electrochemistry and for her never-ending patience in revising my various text submissions. I cannot thank her enough for her continuous support through the often complicated course of this work. I could not have made it this far without her help. Thank you for everything you do and continue to do.

I would also like to deeply thank my co-supervisor Professor EDFOUF Zineb, whose, guidance, insights and knowledge in this field have made this work possible. I am extremely grateful for the encouragement and advice she has provided. Her assistance and suggestions have been invaluable throughout this study. She significantly contributed to the successful completion of this thesis. Thank you for your great kindness and for always taking the time to guide me and for being available for support and help.

Furthermore, I am truly thankful to Professor ABD-LEFDIL Mohammed, who was more than generous in agreeing to preside the jury for the defense. Thank you for welcoming me into your laboratory and for providing me guidance, support and feedback throughout this study.

*I would like to thank Professor TAIBI M'Hamed, from the "*Ecole Normale Supérieure de Rabat"*for accepting the position of thesis rapporteur and to have examined this work.*

I would also like to express my gratitude to Professor MANOUN Bouchaib from the "Faculté des Sciences et Techniques de Settat" for accepting the position of thesis rapporteur and to have examined this work.

I would also like to thank Professor SAADI Mohamed from "Faculté des Sciences de Rabat" for accepting the position of thesis rapporteur and to have examined this work.

My sincere gratitude goes also to Professor PEREZ VICENTE Carlos from "Université de Cordoba-Espagne" for having kindly examined this work.

I would like also to thank Professor OUBLA M'Hamed for all the help he provided and for having accepted to participate in this thesis jury.

Also, a big thank you goes to all my friends and colleagues of the MANAPSE group who I have worked with, for all the support and encouragement I received during the work on this thesis: LALLAOUI Abdelfettah, BENABDALLAH Omar, BATTAS Manale, ROUCHDI Mustapha and EL HAT Abderrahim. I am extremely grateful that so many extraordinary people have surrounded me during this journey.

Finally, I must express my very profound gratitude to my parents for providing me with unfailing support and continuous encouragement throughout my years of study, and to my husband Hassan, my brothers, Nabil and Yacine, and my sister Sanaa. This accomplishment would not have been possible without them. You gave me your unconditional support, strength and love through all this long process.

Thank you to everyone who was there for me throughout this wonderful experience of my PhD research. You will always have a special place in my heart.

This thesis is dedicated to my beloved daughter **Rym**

who has shown me the beautiful side of life

Thank you for giving me unlimited happiness and pleasure

You light up my life

Abstract

This thesis concerns the structural and electrochemical study of different materials and their composites. First, Tin phosphite $SnHPO_3$ and its composite with reduced graphene oxide ($SnHPO_3$/RGO) as new anodes for lithium-ion batteries. Second, RGO based materials doped with nitrogen (N-RGO), phosphorus (P-RGO), both nitrogen/phosphorus (PN-RGO) and both iron oxide/nitrogen composites Fe_3O_4/N-RGO, as catalysts for oxygen reduction reaction (ORR). Third, an original biological route to synthesize RGO using different types of bacterial species is tested. $SnHPO_3$ and its composites are synthesized using the hydrothermal method. Structural and morphological characterizations confirmed the formation of these materials without any impurities. The electrochemical tests for $SnHPO_3$ are performed using two binders. CMC binder has allowed a better electrochemical behavior compared to PVDF. For $SnHPO_3$/RGO, the obtained results proved that RGO plays an important role in enhancing the electrochemical performance of $SnHPO_3$ electrode. The $SnHPO_3$/RGO composite with 5%RGO showed the most stable cycling performance. The RGO doped materials are successfully synthesized and characterized. Electrochemical tests have shown that Fe_3O_4/N-RGO composite has the best catalytic activity for ORR in alkaline solution compared to the other catalysts. The obtained results for bacterial reduction effect on graphene oxide confirmed that bacteria could partially reduce graphene oxide up to 98.2%.

Keywords: Tin phosphite, Anode, Hydrothermal method, Reduced graphene oxide, Lithium-ion batteries, Catalyst, Oxygen reduction reaction, Bacterial reduction.

Table of content

List of figures

Part A

Part B

Appendix

List of tables

Part A

Part B

General introduction

There is an increasing and needed trend towards fossil fuels consumption reduction mainly due to environmental impact. The use of new sustainable and environmentally friendly energy, such as wind, solar, geothermal, water, and tidal energy, has attracted great attention in the past decades as a substitute for traditional primary energy [1].

A much simpler way to improve the utilization efficiency of renewable energy is the energy storage. Therefore, the exploration of high-performance energy storage devices is urgently required in order to most efficiently use renewable energy sources [2].

Currently, electrochemical energy storage technologies are becoming global concerns due to the emergent need for the wireless communication, the electrification of transportation, the space applications and the developed market for mobile electronics [3]. Each of these applications has different requirements. Consequently, there is a long list of energy storage technologies (**Figure i**), of which some are already commercial, while others are still in research and development or demonstration stages. These technologies include lead-acid, lithium-ion, nickel-cadmium, nickel metal hydride and metal-air batteries, among others [4], [5].

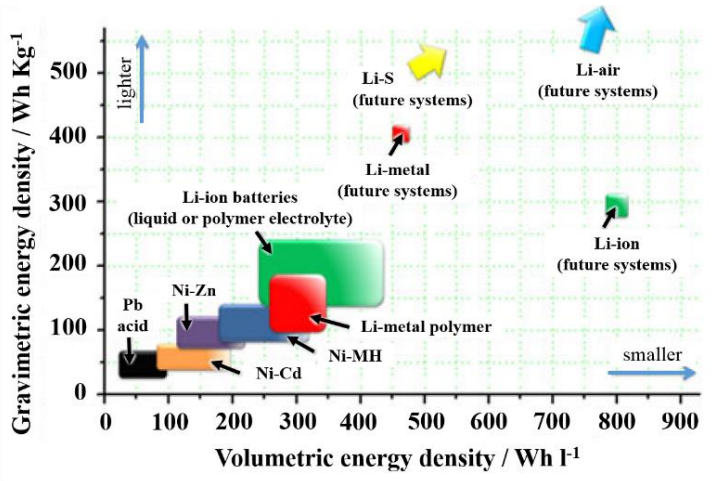

Figure i. Comparison of volumetric and gravimetric energy density for different energy storage technologies [6]

Each energy storage technology has its own performance characteristics that make it more or less suitable for a specific application. While some energy storage systems are strictly

stationary; others are adaptable to mobile applications. Altogether, rechargeable batteries dominate portable and mobile energy storage applications [4].

Compared to other battery technologies, lithium-ion batteries (LIBs) have the most powerful performance such as prolonged service life, larger number of charge/discharge cycles and higher potential for energy storage, as they store much higher energy per unit weight or volume [7]. LIBs are a vital component in everyday life applied in many fields. The largest market has been portable electronics such as smart phones, tablets and laptops. The battery has also found use in medical devices for example in hearing aids and glucose sensing [8]. Additionally, LIBs are used in large-scale smart grids and in aerospace applications, including satellites and aviation. The application targets of LIBs have spread into the electric vehicles (EVs) [9].

The commonly used graphite as anode has good cycle life performance and low production cost. However, two major negative points have led research to find alternative anodes. First, its practical reversible capacity (280 - 320 mAh/g) [10] which is not sufficient for the future market requirements. Secondly, its use causes a risk of short circuit involved by the formation of lithium dendrites at low operating potential (0.1 V Vs Li^+/Li). Therefore, it is urgent to find other anode materials. Many alternatives to graphite, currently used as a negative electrode, have been studied such as lithium alloys, and transition metal oxides [11].

On the other hand, metal-air batteries have been known to provide clean and efficient power sources for a wide range of applications [12]. The theoretical electrochemical performances associated with these technologies are far superior to those of lithium-ion batteries. The energy density provided by current lithium-ion batteries still pales in comparison to the combustion engine [13].

Metal-air batteries are a new development in battery technology that replaces its cathode with an air-breathing electrode. In these systems, one necessary reaction at the cathode is the catalysis of oxygen reduction reaction (ORR), which is the rate-determining factor affecting overall system performance [14]. The Oxygen reduction is considered one of the most important electrocatalytic reactions because of its role in electrochemical energy conversion, several industrial processes, and corrosion. Consequently, for many years it has been the focus of electrochemical interest [15].

The performance and efficacy of these metal-air batteries significantly depend on the reaction kinetics of the oxygen reduction reaction (ORR), which is notorious for its extremely slow kinetics. Thus leading to insufficient performances in corresponding devices. To overcome this, various electrocatalysts cathode with high activity towards ORR are normally used in which precious metal catalysts, especially Pt-based catalysts, are considered the most active [16]. Platinum has been the only commercially available catalysts for ORR and the best catalyst for over 170 years, due to its high activity and stability in both aqueous acidic and alkaline environments. However, these precious metal catalysts are known to be extremely expensive, limited in world supply and not sufficiently efficient [17].

Therefore, developing higher ORR catalytic activity, inexpensive and abundantly found material electrocatalysts for ORR is very demanding. Great efforts have been made to develop new materials as ORR catalysts. Non-precious metal alternatives to replace precious metals in which Fe, Co, Ni, Mg and other metals are being explored to fabricate catalysts with remarkable ORR activity [18]. Moreover, although ORR electrocatalysts have been intensively explored and developed, significant breakthroughs have yet been achieved in terms of catalytic activity, stability, cost and associated electrochemical system performance.

The focus of this research is in these two areas, either in the search for new materials likely to be used as negative electrodes for lithium-ion batteries and as catalysts for metal-air batteries. We were interested in tin phosphite $SnHPO_3$ and its composite with reduced graphene oxide (RGO) as a possible anode material for Li-ion batteries, due to its open-framework with large free channels sizes. In addition, to investigate potential active non-precious catalysts for the oxygen reduction reaction to be used in metal-air batteries, the research focuses too on reduced graphene oxide based materials doped with nitrogen, phosphorus, both nitrogen/phosphorus and both iron oxide/nitrogen composite.

Part A:

Tin phosphite $SnHPO_3$ and its composites $SnHPO_3$/RGO new anode materials for Li-ion batteries

Introduction

Li-ion batteries are a proven technology for providing clean and efficient energy and can be used in a variety of applications. The first lithium battery was built in the 1970s by Michael Stanley Whittingham, who used lithium metal and titanium (IV) sulfide as electrode [19]. However, lithium metal is highly reactive, as a result, these initial lithium battery cells suffered from safety problems. Therefore, this chemistry found no use, but provided the basis for further work. To address this issue, it was more appropriate not to use metallic lithium, but rather compounds that are capable of donating lithium ions (Li^+).

The widespread growth of LIBs has been primarily driven by the introduction of innovative materials. In the same period, reversible intercalation in graphite as anode and cathodic oxides as cathode was researched and proposed by Jürgen Otto Besenhard [20]. In the late 1970s, Samar Basu demonstrated the electrochemical intercalation of lithium in graphite [21]. However, the battery cells experienced rapid deterioration with each recharge. This inconvenience was refined by Rachid Yazami, who tackled this problem in the early 1980s through his research on the reversible electrochemical intercalation of lithium in graphite [22].

Since that, lithium-ion batteries (LIBs) have found a central place in solid-state electrochemistry, and much efforts have been made to develop and improve the battery performance, until they were first successfully commercialized by SONY corporation in 1991 and made them popular energy storage devices [23].

Many alloy systems, such as Li_xAl, Li_xSi, Li_xSn, and Li_xSb have been extensively studied as anode material for LIBs because of their theoretical capacities two or three times higher than that of graphite anodes [24], [25]. One of the most interesting materials as active Li-ion anodes is tin metal (993 mAh/g theoretical capacity to generate $Li_{4,4}Sn$) [26]. However, there are few drawbacks that hinder their practical application. Due to the lithium insertion/extraction (lithiation/delithiation), tin electrode is subjected to a huge volume expansion which causes the pulverization of tin particles and leads to a loss of electrical and mechanical contacts within the active material and with the current collector [27]. As a result, metallic tin electrode performs poor cyclic retentions and thereby leads to severe capacity decay and short cycle life [28].

The performance of tin alloys electrodes can be enhanced significantly when using an active-inactive phase MM' where M (Sn in this case) is the active element and M' the inactive element or matrix toward lithium. This latter provides structural stability to the electrode by holding Sn particles well dispersed and absorbing their volume expansion, minimizing consequently its negative effects [29].

Compounds such tin oxides and tin phosphates have been widely studied [30]. They have received a large attention thanks to their theoretical capacities which are two or three times higher than that of carbon-based materials (SnO_2: 781 mAh/g and $Sn_2P_2O_7$: 572 mAh/g; all for $Li_{4,4}Sn$) [31]. These materials are known to produce a conversion reaction with lithium during the first cycle. Lithium reacts with oxygen in SnO_2 by forming Sn particles that reacts reversibly with Li (Li_xSn alloys) and Li_2O phase [11] which acts as the matrix buffering the volume change, giving more stable cyclability. In the case of SnP_2O_7, the matrix formed is made of Li_3PO_4 and $Li_4P_2O_7$ phases [32].

With the above interesting results, we have focused of other possible active-inactive phase tin based materials. Tin phosphite $SnHPO_3$ seems to be an interesting candidate due to its open-framework with large free channels sizes.

The objective of the present work is to synthesize tin phosphite $SnHPO_3$ using a simple hydrothermal method, and study its electrochemical behavior for the first time as anode for lithium-ion batteries. We demonstrated that the lithiated phosphite phase acts as the matrix that holds Sn particles after the first cycle. The open-framework and the large size channels buffer tin nanoparticles volume expansion while maintaining lithium conduction.

The first chapter describes the fundamental aspects of lithium-ion batteries and the common materials used. The bibliographic research of the use of tin based materials and phosphite in Li-ion batteries are also introduced. This chapter focuses also on the addition effect of reduced graphene oxide and that of binders.

In the second chapter, experimental procedure of the prepared materials, characterization techniques principles and electrochemical measurement methods are addressed.

In the third chapter, the results of structural, morphological and electrochemical characterizations are investigated for the prepared materials.

Chapter I: Literature survey

I.1 Lithium-ion batteries (LIBs)

I.1.1 Electrochemical principles of a lithium-ion battery

Li-ion batteries consist of two lithium-hosting electrodes, anode and cathode, immersed in an electrolyte kept apart by an electrolyte-permeable separator. Each component of the electrode has a specific function [33].

Current commercial batteries are using $LiCoO_2$ or $LiFePO_4$ as cathode materials and graphite as anode material. Although some battery manufacturers have opted for non-graphite anodes as $Li_4Ti_5O_{12}$. The aforementioned compounds are mixed with conductive additives such as carbon material to improve the electrical conductivity and the diffusion coefficient, and a binder (such as Poly Vinylidene Flouride). This latter improves the mechanical stability and flexibility of the electrode [34].

Liquid electrolyte is used in the majority of lithium-ion batteries. It contains a mixture of lithium salt such as $LiPF_6$, $LiBF_4$, $LiClO_4$ which dissolves in a mixture of organic alkyl carbonate solvents like ethylene (EC), dimethyl (DMC), diethyl (DEC) and ethylmethyl (EMC) carbonate with high ionic conductivity. They facilitate the mobility of lithium ions while being electrically insulating in order to prevent short circuits, and hence a key factor in the battery performance [35].

Two types of metallic current collectors are used to deliver electronic current from/to the electrodes to/from posts that connect to the external circuit: aluminum foil for the cathode and copper foil for the anode. The main requirements for current collectors are conductivity and stability/inactivity under the operating conditions inside the cell [36].

The separator, that is ionically transparent and electrically insulating, is sandwiched between the two electrodes, and have the function of preventing direct contact between the anode and the cathode while ensuring lithium ion mobility. The most common separator materials are polyethylene and polypropylene [33].

The rechargeable battery cell stores electrical energy as chemical energy in the two electrodes, anode (reductant) and cathode (oxidant), and has a reversible redox reaction at both electrodes. During cycling, lithium ions migrate back and forth between the anode and the cathode, as illustrated in **Figure A.I.1**. When a LIB is charged, lithium ions are extracted from the cathode ($LiCoO_2$), diffuse across the electrolyte, and are inserted into the anode (graphite) while external electrons move inward to the negative electrode (graphite). During discharge,

the electrons and ions flow in reverse directions. However, in a half-cell consisting of electrode material (can be cathode or anode) and lithium metal, Li ions are extracted from the electrode material and deposited on the surface of the lithium metal during the charge process, and Li ions are inserted into the host electrode material during discharge [37].

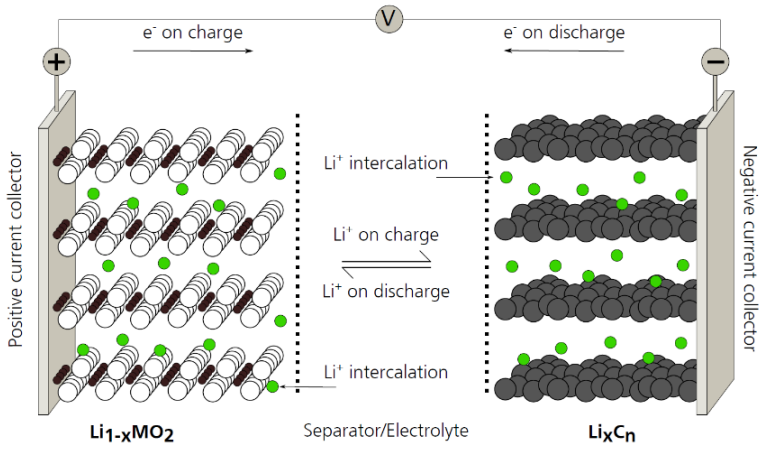

Figure A.I.1. Schematic of the charge/discharge process in a lithium-ion battery [38]

The charging process of a Li-ion battery represented in **Figure A.I.1** is described by redox equations [39]:

Cathode: $LiMO_2 \rightarrow Li_{1-x}MO_2 + xLi^+$

Anode: $xLi^+ + xe^- + C_6 \rightarrow Li_xC_6$

During intercalation of Li ions, the organic electrolyte is simultaneously reduced, and the resulting insoluble products form an irreversible passivating solid-electrolyte interphase (SEI) layer on the graphite surface. The formation of a resistive and unstable layer, sometimes denoted the surface layer (SL), can also occur on the cathode through electrolyte oxidation as a result of irreversible chemical reactions between the electrode and electrolyte [40].

I.1.2 Battery key characteristics

The most relevant characteristics of a battery are its specific energy and power, capacity, durability, cycle life, safety and cost. These parameters are key issues for improving the performance of lithium-ion batteries and are in turn linked to the electrode (anode and cathode) and electrolyte materials used.

The specific energy is one of the central development criteria in Li-ion batteries. It describes how much energy the device can store per mass or volume. It depends on the type of cathode and anode materials used as well as their nano and micro-structures. Current commercial Li-ion batteries store charges through faradic redox reactions with high energy density of about 200 Wh/kg. It can be expressed in Watt-hour (Wh) as the integral of power over time:

$$E = \int_0^t U \times I \, dt \qquad [41]$$

The specific power is often described as how much power in kW could a battery provide for a kWh of capacity. The maximum power a Li-ion battery could provide depends on its voltage, the kinetics of the charge migration and the transfer of the device, the density of lithium ions and the electrodes' conductivity. It corresponds to the product of voltage times current at any instant of time. Its unit is watt (W) and can be expressed by the following equation:

$$P = \int_0^t \frac{U \times I}{t} \, dt \qquad [42]$$

As for the capacity, it quantifies the amount of electric charge it can deliver at the rated voltage. In other words, it is a measure of how much lithium is reversibly incorporated into the anode during charging. The battery capacity is measured in milliAmpere-hour (mAh).

$$Q_{th} = \frac{nF}{3{,}6\ M} \qquad [43]$$

Another important property of a battery is its durability. Battery degradation occurs in tough operating conditions such as low or high operation temperatures, overcharge and deep discharge [44]. The most relevant durability indicator is the cycle life, which is the number of times a battery can be charged and discharged over its lifetime under standard operating conditions, before its key performance metrics (i.e. capacity and power) drop to 80% of initial values. According to the industry standard, a battery has reached the end of its lifetime, when the (specific) capacity has reached 80% of its "initial" value [45].

On the other hand, cycle ageing is additionally subject to the battery charge and discharge conditions. In practical terms, battery ageing is caused by the loss of cyclable lithium and active electrode materials, and is noticed as capacity fade and loss of power. The loss of cyclable lithium is related to side reactions, while the loss of electrode active materials is due

to factors such as dissolution, structural degradation and particle isolation [46]. These are the major problem in the application of lithium-ion battery.

I.1.3 Materials for lithium-ion batteries: Electrolyte, Cathode and Anode

Despite the success of current LIBs designs, the rapid growth of global energy demand necessitates to develop LIBs with substantially better electrochemical performance, including higher power/energy density, longer cycle life and faster charge/discharge rates, especially for transportation applications. To meet these needs, it is more and more necessary to search for alternatives to the different battery components (electrolyte, cathode anode…).

I.1.3.1 Electrolyte for Li-ion batteries

Several types of electrolytes have been used in lithium-ion batteries. The most common can be classified as organic liquid, ionic liquid, polymer and inorganic solid electrolytes [47].

Organic electrolytes are the most well-known form of electrolytes for LIBs owing to their fascinating characteristics, including higher ionic conductivity and good/stable contact with various electrodes. They consist of a solution of a lithium salt in organic solvents. The most commonly studied organic solvents are ethylene carbonate (EC), propylene carbonate (PC), dimethyl-carbonate (DMC), diethyl carbonate (EMC), dimethoxyethane (DME) [38].

Due to being a pure ionic mixture, ionic liquids (ILs) have a higher conductivity than common organic electrolytes. By definition, ionic liquids only consist of ions and are in a liquid state below 100 °C. Ionic liquids are believed to be excellent solvents for battery electrolytes according to recent investigations, owing to their outstanding advantages, including high thermal and electrochemical stability, non-flammable properties, and high ionic conductivities. The most commonly employed ionic liquid cations for electrolytes are BMP^+(Pyr13), $EMIm^+$(C2mim) and $BMIm^+$(C4mim), while $TFSI^-$ and FSI^- are two widely used anions for ionic liquids [48].

Polymer electrolytes offer other advantages over their liquid counterparts, mostly in safety issues. They are a useful component for solid electrolytes, due to their excellent mechanical, thermal and electrochemical stability, which prevents dendrite formation on the anode. Currently, the most widely studied polymer hosts are poly(vinyl chloride) (PVC), poly(vinyl alcohol) (PVA), poly(acrylic acid) (PAA), poly(ethylene oxide) (PEO), poly(acrylonitrile) (PAN), poly(vinylidene fluoride) (PVdF), poly(methyl methacrylate) (PMMA), and PVdF-HFP etc [49]. A solid electrolyte can also act as a separator of the

electrodes. The use of solid electrolytes can also aide in the use of high capacity materials, such as metallic anodes and sulfur cathodes, by suppressing dendrite formation in the case of the anodes, and polysulfide shuttling in the case of sulfur [50].

I.1.3.2 Cathode for Li-ion batteries

The physical and chemical properties of the cathode materials, such as high electronic conductivity, high ionic diffusion, high capacity, low lithium diffusion barrier, good structure stability that can prevent significant structural change after charge/discharge process, are the key factors that determine the electrochemical performance of the LIBs [51].

The cathode materials that have been widely studied are represented by three types: layered oxides, spinel oxides, and phosphates.

- **Layered lithium transition metal oxides $LiMO_2$ (M = Co, Ni, Mn)**

Transition metal oxides are intercalation compounds that have been widely used as cathode materials since the 1990s. Lithium cobalt oxide $LiCoO_2$ is the cathode that dominates the lithium-ion battery market owing to its attractive volumetric energy density, high rate capability and excellent cycling stability. The main disadvantage of this type of electrode is its low inherent safety; due to the limited thermal stability of cobalt-oxide, high cost and toxicity. Also, this electrode suffers from low reversible capacity, which can reach only 120 - 140 mAh/g corresponding to 0,5 lithium for the commercial batteries [52]. These issues make this material used only for small cells and not for large scale applications, and thus the research and development of alternative cathodes is highly recommended.

- **Spinel $LiMn_2O_4$**

Spinel-type lithium manganese oxide $LiMn_2O_4$ is an important type of cathode materials that was first commercialized in 1996. It is an attractive alternative to $LiCoO_2$ cathodes due to its low cost, wider abundance of Mn, low toxicity and higher thermal stability of manganese oxide and excellent structure stability at the discharging voltage around 4 V. Nevertheless, the discharge of $LiMn_2O_4$ proceeds in two steps, around 4 V and 3 V with capacity of only 120 mAh/g. In addition, it was rapidly shown that it suffers from severe capacity fading at high temperatures related to dissolution of manganese into electrolyte, resulting in the deterioration of cathode's cycling performance. This issue could be suppressed significantly by partial substitution of Mn with other metals (Co, Mg, Cr, Ni, Fe, Al, Ti, Cu, Zn etc.) [53].

- **Olivine $LiFePO_4$**

$LiFePO_4$ is one of the most fully developed cathode materials among olivine phosphates and already has been used commercially in LIBs since 1999, with a capacity about 170 mAh/g at discharge potential of about 3.4 V. It is the first cathode material with abundant amount of raw materials and environment friendly. It has satisfactory cycle stability at low currents, better thermal stability and safety upon lithium (de)insertion compared to metal oxides, excellent cycling performances due to the small volume change (approximately 6%) during charge and discharge [54]. Nevertheless, these compounds face a critical challenge of low diffusion coefficient of Li^+, low electronic conduction ionic conductivities, resulting in poor rate performance, which greatly limits the application of $LiFePO_4$ in high rate conditions [46].

Olivine phases containing alternative transition metal ions such as $LiMnPO_4$, $LiCoPO_4$, and $LiNiPO_4$ have also been investigated [40].

I.1.3.3 Anode for Li-ion batteries

In the case of anode, three types of materials have been reported with different reaction mechanisms.

- **Intercalation**

The first mechanism is known as the intercalation reaction, it is based on the insertion of Li^+ ions into layered structures, such as graphite and various carbon nanomaterials.

Graphite with a specific capacity of 370 mAh/g is usually employed as a classical intercalation material in current commercial lithium-ion batteries. In fact, most types of carbon materials possess high capacity (200 - 600 mAh/g) and good power capability [55]. However, they suffer from the lithium dendrites formation that can appear on the anode surface, leading to internal short circuiting of LIBs.

Ti-based oxides, such as TiO_2 or $Li_4Ti_5O_{12}$ are another class of anode materials that have been also extensively studied as intercalation materials [56]. They have been considered as promising materials for lithium storage due to their high safety, good cycle life, low cost and high power capability. However, these materials undergo low theoretical capacities, low electronic conductivity and low energy density during cycling.

- **Alloying**

The second mechanism for anode materials is based on alloying reactions between lithium and some elements to form Li_xM alloys. Si, Sn, Sb and Ge are the most extensively studied alloying anodes for Li-ion batteries. The capacities from alloying reactions reach extremely high values at low operating potentials, with Si and Sn being the most attractive because of their high energy storage capacities, abundance in the earth shell and environmental compatibility. For example, Sn anode can alloy Li with the stoichiometry of $Li_{4.4}Sn$, leading to a capacity of around 993 mAh/g [57]. Unfortunately, practical use of alloy electrodes as a bulk, is handicapped by the huge volume changes (up to about 300%) associated with the (de)alloying process. This causes severe structural destruction, which is accompanied by mechanical and electrical disconnection within the battery components leading to a drastic diminishing of energy storage capacity of electrodes.

- **Conversion**

The third reaction mechanism of anode materials is the conversion reaction. Recently, conversion materials with high capacity provided through reversible replacement redox reactions between Li^+ and transition-metal cations, have been developed as attractive alternatives to the next-generation LIBs. This type of mechanism involves electrochemical reactions that are leading to the formation of new chemical species, often with structures different from the initial structure.

Different conversion-type anode materials has been studied as LIBs anode electrodes, for example, oxides, fluorides, sulfides, selenides, nitrides, phosphides and even hydrides [40]. The main advantage of such alternative reaction pathways is the large increase in electrochemical capacity and lower production cost. They could ensure better safety of the battery by avoiding the problem of lithium dendrite formation with graphite. As a consequence, conversion electrodes can be developed with outstanding capacity improvements over graphite or insertion oxides.

While the prime challenge of the conversion-based materials is to suppress the major structural changes caused by the volume change, leading to severe capacity fading and poor cycling stability. Also, this type of materials suffer from poor electronic and ionic conductivity and continuous electrolyte decomposition.

Some of the above materials such Sn-based compounds (oxides, phosphides, phosphates, etc) can alloy with Li and can undergo a conversion reaction [58]. Such conversion-alloying materials exhibit higher capacity than pure conversion systems.

I.2 Tin and tin based anode materials

Different alloy systems with lithium, such as Li_xAl, Li_xSi, Li_xSn, and Li_xSb have been extensively studied as alternative anode materials for LIBs because of their theoretical capacities two or three times higher than that of graphite anodes [59].

I.2.1 Tin anode materials

Currently, among the most interesting materials as active Li-ion anodes is tin metal which reaches 993 mAh/g theoretical capacity to generate $Li_{4,4}Sn$ alloy [57]. Several alloy compounds are formed during Sn lithiation. Wang et al. [60] have studied the electrochemical behavior of Li-Sn alloys at 25 °C. Each alloy is formed at a different potential Vs pure lithium as it can be seen in the following table.

Table A.I.1. Formation potentials of Li_xSn alloys at room temperature

Alloy potential (V)	Composition interval
0.380	$Li_{3.5}Sn$-$Li_{4.4}Sn$
0.420	$Li_{2.6}Sn$-$Li_{3.5}Sn$
0.485	$Li_{2.33}Sn$-$Li_{2.63}Sn$
0.530	$Li_{0.7}Sn$-$Li_{2.33}Sn$
0.660	$Li_{0.4}Sn$-$Li_{0.7}Sn$

However, its practical application is limited due to the huge volume expansion during cycling (260% of the initial volume compared to 12% for carbon graphite) [61]. This results in important structural changes, which causes cracks and disintegration of tin particles and leads to an electrical and mechanical disconnection within the active material and with the current collector. Consequently, metallic tin electrode suffers from large irreversible capacity loss, short cycle life and a poor cyclability.

The electrochemical behavior of metallic tin is shown in **Figure A.I.2**. The results of the galvanostatic cycling show a rapid drop in capacity during cycling. This is attributed to the strong volume expansion of the element Sn causing loss of electrical contact during cycling and

therefore loss of capacity. These results are in agreement with those of cyclic voltammetry (CV). **Figure A.I.3** shows the presence of several peaks corresponding to the formation and deformation of different alloys. The capacity continues to increase until the 5th cycle as the peaks intensify indicating gradual activation of the material, then decreases considerably (cycle 20) indicating the loss of reversible capacity [62].

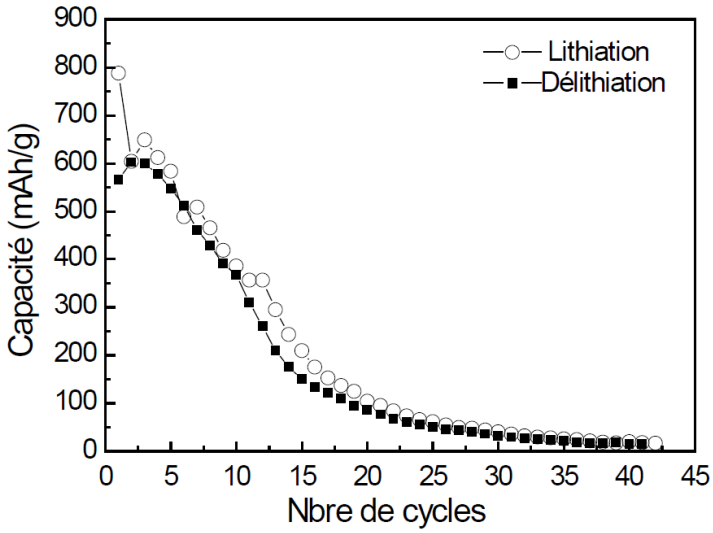

Figure A.I.2. Capacity as a function of the number of cycles during the galvanostatic cycling of Sn metal at C/50 and a voltage range of 0.07 V - 2 V [62]

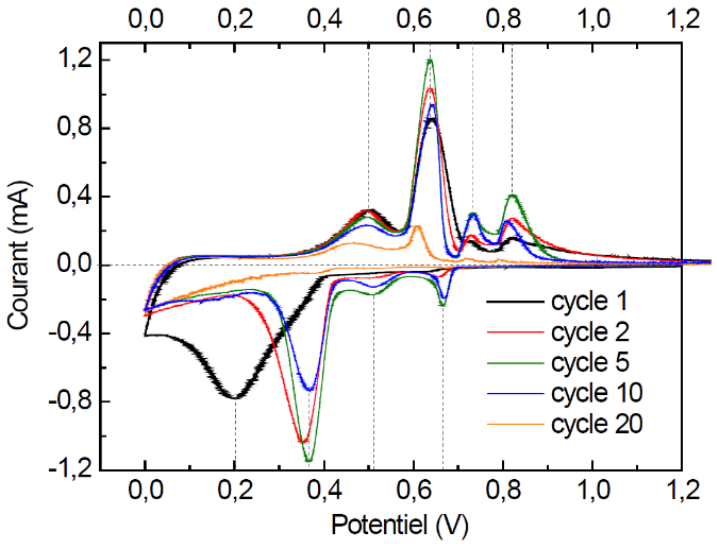

Figure A.I.3. Cyclic voltammetry (CV) of Sn metal at 0.1 mV/s [62]

The performance of this electrode has been enhanced when using tin based materials as alternative to metallic tin.

I.2.2 Tin based anode materials

Tin oxides and tin phosphates materials present higher theoretical capacities compared to carbon anodes (SnO_2: 781 mAh/g and $Sn_2P_2O_7$: 572 mAh/g; all for $Li_{4,4}Sn$) [63], [64]. In addition, they exhibit better reversible capacity and capacity retention than metallic Sn. These compounds are known to produce a conversion reaction with lithium during the first cycle. In the case of tin oxide SnO_2, lithium reacts with oxygen to form Li_2O phase and metallic tin [65]:

$$SnO_2 + 4Li^+ + 4e^- \rightarrow 2Li_2O + Sn$$

As for tin pyrophosphate $Sn_2P_2O_7$, lithium reacts with phosphate group to form Li_3PO_4 and $Li_4P_2O_7$ phases and metallic tin.

$$4Li^+ + Sn_2P_2O_7 + 4e^- \rightarrow Li_3PO_4 + LiPO_3 + 2Sn \text{ [66]}$$

$$4Li^+ + Sn_2P_2O_7 + 4e^- \rightarrow 2Li_4P_2O_7 + 2Sn \text{ [63]}$$

The metallic tin produced in both electrodes is dispersed within these phases, which form an active or inactive matrix toward lithium for the following cycles. When metallic tin Sn particles react reversibly with lithium, it forms intermetallic alloys Li_xSn:

$$xLi^+ + xe^- + Sn \rightarrow Li_xSn \text{ [66]}$$

The matrix such lithium oxide and lithium phosphate phases provides structural stability to the electrode by holding Sn particles well dispersed and buffers their volume expansion, giving more stable cyclability. In addition, the matrix acts as a good electrical conductor that can significantly improve the electron transport and facilitates rapid diffusion of Li ions. As a result, the electrode presents better electrochemical performance. However, in some cases after several cycling, it still suffers from capacity fading due to tin nanoparticles aggregation to form clusters again and volume changes become problematic.

I.2.3 Tin based materials composite with graphene

Alloying materials are often made into composite structures to accommodate expansion and increase conductivity, for example, as composites of porous carbons, graphene, CNTs, etc.

Several studies have investigated the effect of graphene on the electrochemical performance of tin oxide SnO_2 [67]. It has been found that the incorporation of carbonaceous materials is a common solution to attenuate the structural deformation of SnO_2-based anodes.

Due to the elastic characteristic and good conductivity of carbon-based materials, these matrices can not only limit the volume variation, but also improve the conductivity of the electrode and improve the electron transport, which could greatly improve the lithium storage performance of SnO_2-based anodes [68]. As an ideal conductive and flexible matrix, graphene has been used extensively to prepare SnO_2-graphene nanocomposites as anodes for LIBs due to its fascinating structure and electronic properties. Hybridization of SnO_2 with graphene has been shown to effectively promote reversible capacity, battery life and performance [69].

Song et al. [70] demonstrated that the Sn/SnO_2/Graphene nanocomposite electrode strongly contributes to improving the electrochemical performance of LIBS. This electrode exhibited excellent performance with higher specific capacities, increasing to 1270 mAh/g after 100 cycles. This can be explained by the reversible conversion reaction of SnO_2 and lithium and which indicates the reversible decomposition of Li_2O.

These results show that this nanocomposite contributes to strengthening the electrochemical performance of Sn-based anode materials for LIBs.

I.2.4 Phosphite as an alternative matrix

Among other matrices, the investigation of phosphite poly-ions, regarded as the development of phosphates poly-ions, is attractive [71]. The synthesis of open-framework metal phosphites by incorporating the pseudo-pyramidal phosphite groups $[HPO_3]^{2-}$ in place of tetrahedral phosphate units $[PO_4]^{3-}$ into the frameworks has resulted in a new class of metal phosphite compounds with more open frameworks [72]. Both oxoanion units have similarities but compared to the phosphate group, metal phosphites exhibit rich compositional and structural diversity, because the presence of three-connected $(HPO_3)^{2-}$ centers favors to reduce the M-O-P connectivity. Furthermore, the hydrogen phosphite group has fewer available coordination centers and low-average charges per oxygen, which can lead to the formation of more open interrupted open frameworks with large pore sizes and low framework density [73].

I.3 Phosphites materials for lithium-ion batteries

By aiming at new materials, the phosphite oxoanion $(HPO_3)^{2-}$ has been the source of many new inorganic and organic phosphites [74]. To date, a large amount of alkaline, alkaline earth and transition metal phosphites open frameworks with different properties and interesting structures have been synthesized and characterized [75], [76].

Organic phosphite has been investigated in literature as electrolyte additive to improve the safety characteristics of LIBs and as flame retardants to improve the thermal stability of the electrolyte. Inorganic phosphite has been studied as cathode for Li-ion batteries.

I.3.1 Phosphite as electrolyte additive

Organic phosphite has been largely studied in electrochemistry field as electrolyte additive for Li-ion batteries. Under high operating voltage of 4.6 V - 4.8 V, organic carbonate solvents in the electrolyte are thermodynamically unstable and easily undergo oxidative decomposition, which is accompanied by the formation of a resistive and unstable surface layer on the cathode. This results in a large initial irreversible capacity loss, poor cyclic stability, cathode destruction and serious fading of the electrochemical performance of the cathode materials, hindering their practical application in lithium-ion batteries [77]. Thus, electrolyte additives contribute to the formation of a protective solid electrolyte interphase (SEI) film on cathode, which could effectively passivate the cathode and results in a decrease in detrimental electrolyte oxidative decomposition reactions on the cathode surface. A variety of phosphite-based additives are well known in improving the electrochemical performance of high-voltage LIBs, such Trimethyl phosphite (TMP) [78], Tris (trimethylsily) phosphite (TMSPi) [79] and Triphenyl phosphite (TPPi) [80]. They all have shown a good impact on improving the cycling performance of the cathode compared with the baseline electrolyte.

Among other interesting applications of organic phosphite-based additives are the flame retardants. Safety concerns have been an obstacle for the development of high power and large size Li-ion batteries. These latter suffer serious hazards resulted from the chemical reactions between electrode materials and electrolyte constitutes at high temperatures. These reactions are known to be very exothermic. Consequently, the cell can be violently vented and the flammable electrolyte solvents can be ignited to combust [81]. To suppress the electrolytic flammability of Li-ion batteries, various phosphite-based flame-retardant (FR) additives into the normal liquid electrolytes have been investigated such Tris (2,2,2-trifluoroethyl) phosphite

TTFP [82]. Its presence favors the formation of solid electrolyte interface (SEI) film on the graphite electrode and increases thermal stability of $LiPF_6$-based electrolytes.

I.3.2 Phosphite as cathode for Li-ion batteries

Few inorganic phosphite has been also studied in electrochemistry field as cathode for Li-ion batteries. Chung et al. [83] reported $Li_{1.43}[Fe^{+II}_{4.43}Fe^{+III}_{0.57}(HPO_3)_6]\cdot 1.5\ H_2O$ as the first phosphite oxoanion compound for lithium exchange reaction. This lithium-mixed-valency iron (II,III) phosphite showed a reversible capacity equivalent to 12 mAh/g for more than 100 galvanostatic cycles.

Asl et al. have studied two new lithium iron (III) phosphite, $LiFe(HPO_3)_2$ [84] and $Li_3Fe_2(HPO_3)_3Cl$ [85] as cathodes. Cyclic voltammetry (CV) results of both cathodes showed the high reversibility of the redox processes. These new phases exhibit acceptable capacity retention upon successive cycling and a reversible capacity of only 70 mAh/g.

However, the capacities of all these phosphites based cathodes are very low and cannot fulfill the demand for high performance batteries.

I.3.3 Phosphite as anode for Li-ion batteries

With all these interesting applications of phosphite materials, very few attention has been received on the use of this latter as anode for Li-ion batteries. Our group is the first who has conducted research on the synthesis of new inorganic phosphite anode materials. The synthesis technique used is hydrothermal method. Titanium (III) phosphite $Ti_2(HPO_3)_3$ was synthesized for the first time [86]. Galvanostatic measurements of the prepared cells proved that $Ti_2(HPO_3)_3$ is electroactive toward Li^+ insertion/extraction at low potential. However, the phosphite anode shows a subsequent capacity fading issues and poor cycling life. Our preliminary interpretation suggests that this probably the result of a large volume change of $Ti_2(HPO_3)_3$ during the charge-discharge processes. One of the solutions to improve the electrochemical performance of this material consists of its synthesis in the form of a composite with graphene: the material $Ti_2(HPO_3)_3$/r-GO [87]. This composite exhibits better reversibility of the delithiation lithiation process with good resistance to electrochemical cycling after the first cycle.

Another new phosphite material has been synthesized by our group $LiTi(HPO_3)_2$ [88]. It shows a good stability of cycling performance. Besides, its operating voltage of 0.7 V, being reduced compared to what has been observed in the case of pure phosphates or oxides, would

result in a high energy density system and could overcome the safety problems related to the decomposition of the electrolyte.

With this research work we are aiming to establish that inorganic phosphite compounds could also find application as anode materials for LIBs. To circumvent this limitation, pursuing for other possible inorganic phosphite based anode would be an ideal way to accommodate the volume expansion resulting from lithium insertion.

Using inorganic phosphite as matrix for tin anode seems to be interesting. Thus, tin phosphite $SnHPO_3$ would be an attractive candidate. To the best of our knowledge, this phosphite has never been studied before as material for LIBs.

I.4 Tin phosphite $SnHPO_3$ structure

The single crystal X-Ray Diffraction (XRD) analysis shows that $SnHPO_3$ crystallizes in the monoclinic space group *C 1 c 1*. It displays a layer structure similar to graphite sheets. However, the inter-layer interaction in $SnHPO_3$ is weak [89].

Its structure is composed of sheets that extend perpendicular to the long b axis (**Figure A.I.4**) and consisting of SnO_3 and PO_3 trigonal pyramids fused together at their bases. The PO_3 group has almost exact trigonal symmetry. The SnO_3 pyramids are less symmetric [90]. The layered topology of $SnHPO_3$ is demonstrated using Scanning Electron Microscopy (SEM), showing the bulk stacking of the $SnHPO_3$ nanosheets.

The $(HPO_3)^{2-}$ anion offers three P-O bonds and one P-H bond. Each tin atom coordinates three separated PO_3 groups. Each oxygen atom bridges one tin and one phosphorus atom. Although the hydrogen atom in $SnHPO_3$ was not determined. It must be bonded directly to the phosphorus atom as shown by spectroscopy for other phosphites [91]. If this is indeed the case, then the hydrogen atom lies at the top of the PO_3 pyramid at roughly tetrahedral angles with the oxygen atoms.

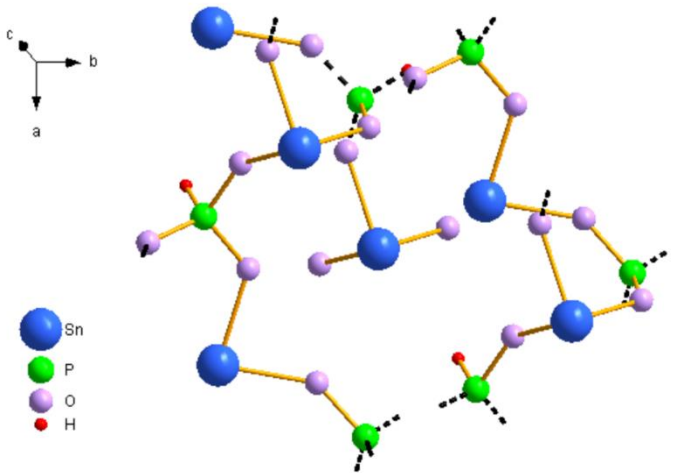

Figure A.I.4. Unit cell structure of $SnHPO_3$ on the ab plane

I.5 Effect of binders

In addition to the active material, other components such as binders also have significant influence on the electrochemical performance of LIBs, including the cycle life and irreversible capacity loss, an appropriate binder can bring better electrochemical results [92]. Binders play a crucial role in assuring a structural stability and mechanical performance of the anode material by holding active materials and conductive additives together and adhering them onto metal current collectors. Thereby, the anode material can resist large volume changes during cycling [93].

Polyvinylidene difluoride (PVDF) is the traditional binder used in the negative electrodes for commercial LIBs, owing to its good electrochemical stability and good binding strength with the other electrode components [94]. However, organic solvents like N-methyl pyrrolidone (NMP) is required as a dispersant to form the slurry, which are costly, flammable, volatile and causes environment pollution. Also, the reaction of F atoms existing in the binder's structure with lithium metal to form stable LiF can cause deterioration of the binder during the charging-discharging cycling performance of batteries. This reaction between Li and PVDF is exothermic and can cause self-heating. Therefore, PVDF is highly unstable in presence of lithium salts [95]. Consequently, an eco-friendly and cost-effective binder is needed to substitute the PVDF binder used in commercial lithium ion batteries to further enhance the electrochemical performance of this latter.

Carboxymethyl cellulose (CMC), a new water-soluble binder, has been successfully used in electrode material for LIBs as alternative to PVDF. CMC shows better accommodation

of volume change during cycling and environmental-friendly features. Further it is significantly less expensive compared to PVDF [96]. CMC is a cellulose derivative with carboxymethyl groups bounded to some cellulose hydroxyl groups. Many studies have confirmed that binders containing functional carboxyl groups and hydroxyl groups present a better function in Si-based anodes than non-functional groups such as PVDF [97]. The surface functional groups of the binder are believed to generate stronger hydrogen and/or covalent chemical bonds among the electrode components, that is, active materials, carbon black and the current collector. The deionized water introduced while making electrodes leads to the free carboxylic acid (-COOH) which can resist the detachment of the active material from the current collector and effectively inhibiting the volume expansion and pulverization of the particles [93]–[95]. This strong interaction has been found to favor the long cycle stability of the anode material and to provide better cycle performance than the electrodes with PVDF binders which bind via weak Van der Waals interactions.

In this study, the synthesis and the electrochemical performances of tin phosphite $SnHPO_3$ as anode material for LIBs have been comparatively investigated by using PVDF and CMC as binders.

I.6 Research context

Taking into account the advantages of the open framework of phosphites, we have imagined using it as matrix for Sn. For this reason, in our research study, we have focused on the synthesis and electrochemical study of tin phosphite based materials as anode for Li-ion batteries.

We demonstrated that the phosphite matrix could help holding tin particles after the first cycle and buffer their volume expansion while maintaining lithium conduction. Also, we have studied the effect of the addition of graphene. This latter is very famous in enhancing the electrochemical performance of several studied materials. The results of structural, morphological and electrochemical characterizations of the tin based anode materials are discussed.

The work presented in this thesis is the result of a collaboration between Mohammed Vth University and Laboratory of Materials and Environmental Chemistry at the Faculty of Science and Technology of Cadi Ayyad University in Marrakech. This work is financially supported from Moroccan Ministry of National Education, Vocational Training, Higher

Education and Scientific Research-Mohammed Vth University under project PPR (Development of new nanomaterial for electrochemical energy storage: Na-air and Li-ion batteries).

Chapter II: Experimental setup

II.1 Material synthesis

II.1.1 Hydrothermal synthesis method

Hydrothermal synthesis is one of the most commonly used methods for preparation of new materials exhibiting a wide variety of properties. It has found its place in several branches of science and technology, covering a range of fields. It is basically a solution reaction-based approach in a closed system under conditions of high pressure and moderated temperature. Hydrothermal synthesis can be used in so many ways primarily because it can utilize a wide temperature range, with a wide variety of compatible precursors. The process dissolves and recrystallizes a substance that is poorly soluble or insoluble under normal conditions [98].

Hydrothermal reactions are often carried out in standard acid digestion bombs. These bombs consist of a PTFE crucible insert that fits into a stainless steel sleeve, or autoclave. Reactants are loaded into the PTFE liner or Teflon, which provides excellent chemical inertness. The liner is loaded into the autoclave, which serves as the pressure vessel by sealing the PTFE liner and providing structural support [99].

There are significant advantages of hydrothermal synthesis method over others; Hydrothermal synthesis can generate materials which are not stable at elevated temperatures. Materials with high vapor pressures can be produced by the hydrothermal method with minimum loss of materials. Also, hydrothermal method produces higher quality crystals in greater yield with controlled morphologies [100].

II.1.2 Synthesis of tin phosphite ($SnHPO_3$)

Tin phosphite ($SnHPO_3$) was synthesized using a simple hydrothermal method. A stoichiometric mixture of phosphorus acid H_3PO_3 (0.8199 g) (Aldrich, 99%), tin (II) chloride dihydrate $SnCl_2$. $2H_2O$ (0.2395 g) (Sigma-Aldrich, 98%) in a molar ratio of 10:1 and oxalic acid $C_2H_2O_4$ (0.1764 g) (SDS, 99.5%) was placed in 40 mL Teflon-lined steel autoclave and heated at 180 °C for 3 days. The obtained white precipitate was filtered and washed with distilled water several times and was left to dry at ambient temperature. The role of oxalic acid in the reaction was to avoid the oxidation of phosphite to phosphate [101].

II.1.3 Synthesis of tin phosphite/reduced graphene oxide composites ($SnHPO_3$/RGO)

The $SnHPO_3$/RGO composites are prepared using the hydrothermal method by a two-step method. In the first step, graphene oxide (GO) and tin phosphite ($SnHPO_3$) were synthesized.

II.1.3.1 Synthesis of graphene oxide (GO)

Graphene oxide (GO) has been synthesized chemically. The first step of the process is to prepare graphite oxide (GTO) from natural graphite using the Hummers method [102] as follows:

A 9:1 mixture of concentrated sulfuric acid and phosphoric acid 97% H_2SO_4 : 85% H_3PO_4 (135:15 mL) was added to a mixture of graphite (1.125 g) and potassium permanganate $KMnO_4$ (6.75 g) and left to stir for 30 min. The reaction was then heated gradually to 50 °C and stirred for 24 h. The reaction was cooled to room temperature (20 min) and then poured onto a beaker of ice (600 mL), followed by the addition of hydrogen peroxide 30% H_2O_2 (9 mL). Then, the mixture was centrifuged and the remaining solid material was washed with hydrochloric acid 5% HCl (200 mL) for three times to remove the impurities and with deionized water for several times until a neutral pH was obtained. The final resulting material was dried for 14 h at 70 °C to obtain graphite oxide powder (GTO).

The second step is to prepare graphene oxide (GO). Graphite oxide powder (GTO) was added to a mixture of deionized water and ethanol, and treated with ultrasound for 1 h to obtain graphene oxide (GO).

II.1.3.2 Synthesis of tin phosphite/reduced graphene oxide composites ($SnHPO_3$/RGO)

Different percentages of GO were tested in this study. We have used 3%, 5%, 8%, 10%, 90% and 100% of graphene oxide (GO).

The $SnHPO_3$/RGO composites was prepared by adding the previously synthesized tin phosphite ($SnHPO_3$) to the graphene oxide suspension (GO), followed by stirring for 2 h. The mixture obtained is then poured into a 40 mL Teflon-lined steel autoclave and placed in an oven at 175 °C for 20 h. Finally, the resulting precipitate is obtained after washing with distilled water and drying at 60 °C. The as-prepared $SnHPO_3$/RGO composites were denoted

$SnHPO_3$ + 3%RGO, $SnHPO_3$ + 5%RGO, $SnHPO_3$ + 8%RGO, $SnHPO_3$ + 10%RGO, $SnHPO_3$ + 90%RGO and 100%RGO (pure RGO).

II.2 Lithium-ion battery cell assembly and testing

II.2.1 Cell assembly

The electrochemical performance of $SnHPO_3$ and $SnHPO_3$/RGO materials as anode for Li-ion batteries were investigated using CR2032 coin cells. The cells were assembled inside an argon-filled glovebox with H_2O and O_2 contents below 0.1 ppm and $SnHPO_3$ or $SnHPO_3$/RGO as the working electrode, metallic lithium foil as both the counter and reference electrode, Whatman paper as separator and a 1 M solution of $LiPF_6$ dissolved in ethylene carbonate and diethyl carbonate (EC:DEC, 1:1 in volume ratio) as electrolyte.

The working electrode consisted of 75% (wt.%) of the prepared $SnHPO_3$ or $SnHPO_3$/RGO as the active material, 15% (wt.%) carbon black as a conductive agent and 10% (wt.%) polyvinylidene fluoride (PVDF) or carboxymethyl cellulose (CMC) as binders blended all together using an agate mortar. Then, N-methyl-2-pyrrolidone (NMP) as solvent in the case of the PVDF binder or deionized water in the case of the CMC binder were added to the mixture until sufficient homogeneity is obtained. The resulting slurry was then coated on a copper foil current collector using a doctor blade instrument, cut into disks, and finally vacuum dried at 110 °C for 12 h.

II.2.2 Electrochemistry testing

The battery cycling was performed using an MPG-2 Bio-Logic multichannel potentiostat. Galvanostatic cycling tests of the cells were conducted at a rate of C/20 for $SnHPO_3$ electrodes with PVDF and CMC binders and at a rate of C/10 for $SnHPO_3$ and $SnHPO_3$/RGO electrodes with only CMC binder in a voltage range of 0.01 - 2.5 V Vs Li^+/Li at room temperature. Cyclic voltammetry (CV) were performed to determine the characteristics of lithium insertion/extraction reactions for the electrodes investigated. The tests were carried out in the same voltage range with a scan rate of 0.01 mV/s.

Chapter III: Results and discussions

In this section results of different structural and electrochemical characterization methods are presented and discussed. Raw tin phosphite phase and its composites with reduced graphene oxide (RGO) have been synthesized with hydrothermal method. Different amounts of graphene oxide (GO) have been used during composite syntheses for comparison. Techniques such as XRD, FTIR, SEM and EDX have been used. Electrochemical characterization has been carried out with galvanostatic cycling and cyclic voltammetry. Two different binders have been tested when preparing the slurry of raw tin phosphite. Their effect on its electrochemical performances is given here.

III.1 Characterizations of tin phosphite ($SnHPO_3$)

III.1.1 Structural and morphological characterizations of $SnHPO_3$

III.1.1.1 X-Ray Diffraction (XRD)

Powder X-Ray diffraction pattern of the prepared $SnHPO_3$ and a simulated pattern based on their single crystal data are shown in **Figure A.III.1.a**. The diffraction positions on experimental pattern are in good agreement with the simulated one and no other peaks were observed, which confirms the purity of the $SnHPO_3$ phase. Refinement of this phase has been done with Rietveld analysis using a Fullprof program and pseudo-Voigt function was chosen to describe the line shape of diffraction peaks. In a first step refinement, correction parameters for systematic line shift errors due to sample (zero shift), unit cell parameters, background coefficients, Caglioti coefficients *U*, *V* and *W* which describe the full width at half maximum (FWHM) of the line and γ parameter which manages the Pseudo-Voigt weighting have been refined. In a second step refinement, scale factor, atomic positions, occupancy factors, isotropic displacement parameters and preferred orientation were refined. All diffraction peaks can be indexed in the monoclinic symmetry with *C1 c1* space group and unit cell parameters a = 7.0818 (3) Å, b = 12.3377 (5) Å, c = 4.6845 (1) Å and β = 120.8854 (11) °. This result is in adequacy with a previous report of Macdonald et al. on $SnHPO_3$ phase [90].

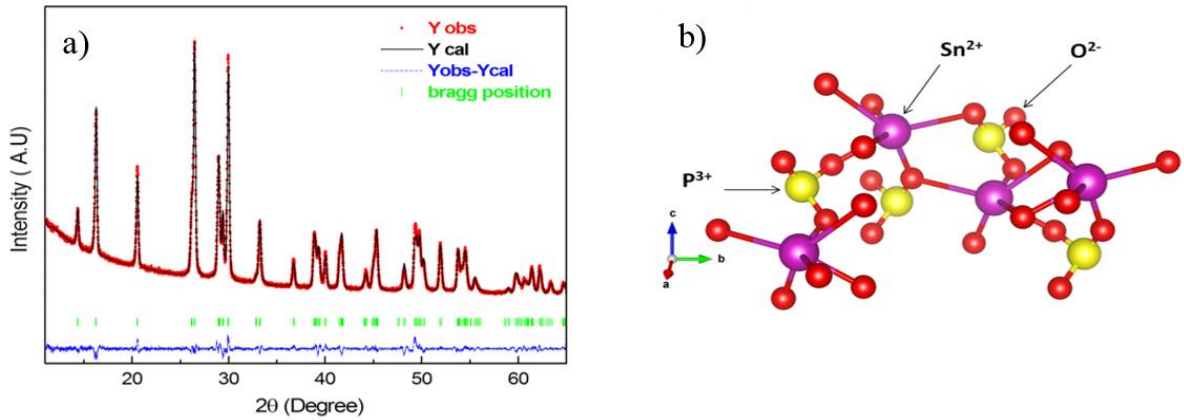

Figure A.III.1.a. Rietveld refinement patterns of $SnHPO_3$ (The upper symbols illustrate the observed data (circles) and the calculated pattern (solid line). The vertical markers show calculated positions of Bragg reflections. The lower curve is the difference diagram **b.** unit cell structure of $SnHPO_3$

Table A.III.1 gathers the structural and microstructural refinement parameters of the Monoclinic structure of phosphite $SnHPO_3$ data obtained from the Rietveld method of the analyzed powder. The unit cell structure of $SnHPO_3$ is represented on **Figure A.III.1.b**. In this structure Sn atoms fully occupy the site with Wyckoff position 4*a*, P atoms fully occupy the site with Wyckoff position 4*a*, whereas O atoms occupy 3 types of 4*a* positions with the following labels: O (1), O (2) and O (3).

The crystallite size (D) is determined using Scherrer's formula expressed by equation:

$$D = K\lambda / \beta \cos\theta$$

With K = 0.9 (Scherrer's constant), θ is the Bragg angle, λ (nm) is the wavelength and β (rad) is the full width at half of the maximum (FWHM). The values of mean crystallites size of are 33 nm.

Table A.III.1. Refined Structural parameters by Rietveld method for tin phosphite $SnHPO_3$

$SnHPO_3$	$\chi^2 = 3.281$
Molecular weight (g/mol) = 198.69 Monoclinic, *S.G : C1 c1*	$R_F = 1.484$, $R_B = 2.440$
$a = 7.0818\ (3)$ Å , $b = 12.3377\ (5)$ Å , $c = 4.6845\ (1)$ Å , $\beta\ (°) = 120.8854\ (11)$, $V = 351.26\ (2)$ Å^3 , Crystallite size (D) = 33 (5) nm	$R_p = 10.2$ $R_{wp} = 8.87$ $R_{exp} = 5.21$

Atomic coordinates, (Biso) isotropic displacement parameters (Biso) and Occupancy

Atom	**Wyckoff sites**	***x/a***	***y/b***	***z/c***	**Biso (Å^2)**	**Occupancy**
Sn	4*a*	0.38782	0.36380	-0.04887	3.22216	1
P	4*a*	-0.00316	0.37197	0.12003	1.68430	1
O (1)	4*a*	0.13637	0.41699	0.40577	1.85729	1
O (2)	4*a*	-0.14791	0.29497	0.18165	3.89100	1
O (3)	4*a*	0.09430	0.30741	-0.06020	1.83922	1

III.1.1.2 Fourier Transform Infrared Spectroscopy (FTIR)

Figure A.III.2 shows the FTIR spectra of the as-prepared $SnHPO_3$. It represents the bands corresponding to the vibrations of the $(HPO_3)^{2-}$ phosphite oxoanions. At higher wavenumbers, a strong and sharp peak observed at around 2391 cm^{-1} which corresponds to the stretching vibrational mode υ(P-H), and a peak at around 1019 cm^{-1} corresponding to the deformation mode δ(P-H) [103]. At lower wavenumbers, approximately 1071 cm^{-1} and 970 cm^{-1}, appear the bands corresponding to the anti-symmetrical stretching mode υ_{as}(P-O) and to the symmetrical stretching mode υ_s(P-O) respectively. Finally, the symmetrical and anti-symmetrical deformation vibrations, δ_s(P-O) and δ_{as}(P-O) are detected in the range of 550 - 451 cm^{-1} of the $(HPO_3)^{2-}$ anion [104].

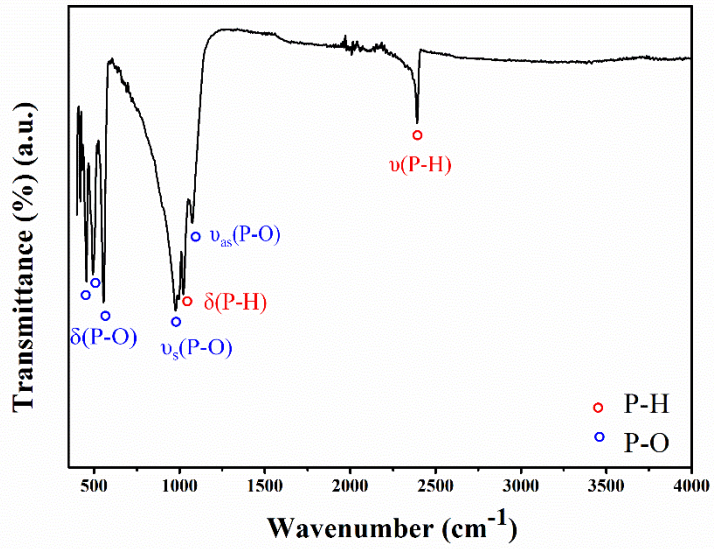

Figure A.III.2. FTIR spectrum of $SnHPO_3$

Table A.III.2. Wavenumbers and attributions of vibration modes of $SnHPO_3$

Wavenumbers (cm^{-1})	Assignments	Reference
2391	υ(P-H)	[103]
1071	υ_{as}(P-O)	[104]
1019	δ(P-H)	[103]
970	υ_{s}(P-O)	[104]
550 - 451	δ_{s}(P-O) and δ_{as}(P-O)	[104]

III.1.1.3 Scanning Electron Microscopy (SEM)

The morphology and structure of the prepared $SnHPO_3$ was investigated using scanning electron microscopy (SEM) analysis which was performed before and after grinding. The sample has been crushed into powder shape to perform the electrochemical tests.

The SEM images of the as-obtained sample in **Figures A.III.3.a** and **b** show long needle-like crystals at two different magnifications ×1300 and ×5000 respectively. The surface aspect of the needles seems to be smooth. The crystals sizes are between 12 and 100 µm in length and between 7 and 10 µm in width. The image **b** further displays that the sample presents a flower-like structure composed of the interconnected needles. No other structure appeared in the sample indicating the formation of a pure crystalline phase of $SnHPO_3$. **Figures A.III.3.c** and **d** show the morphology of the sample after grinding. The long needle-like crystals shape is

lost giving rise to inhomogeneous crushed elongated particles with overlapping layers having various sizes and shapes. These stacking sheets are indicated by red arrows. However the sizes keep much more smaller than those of the needles.

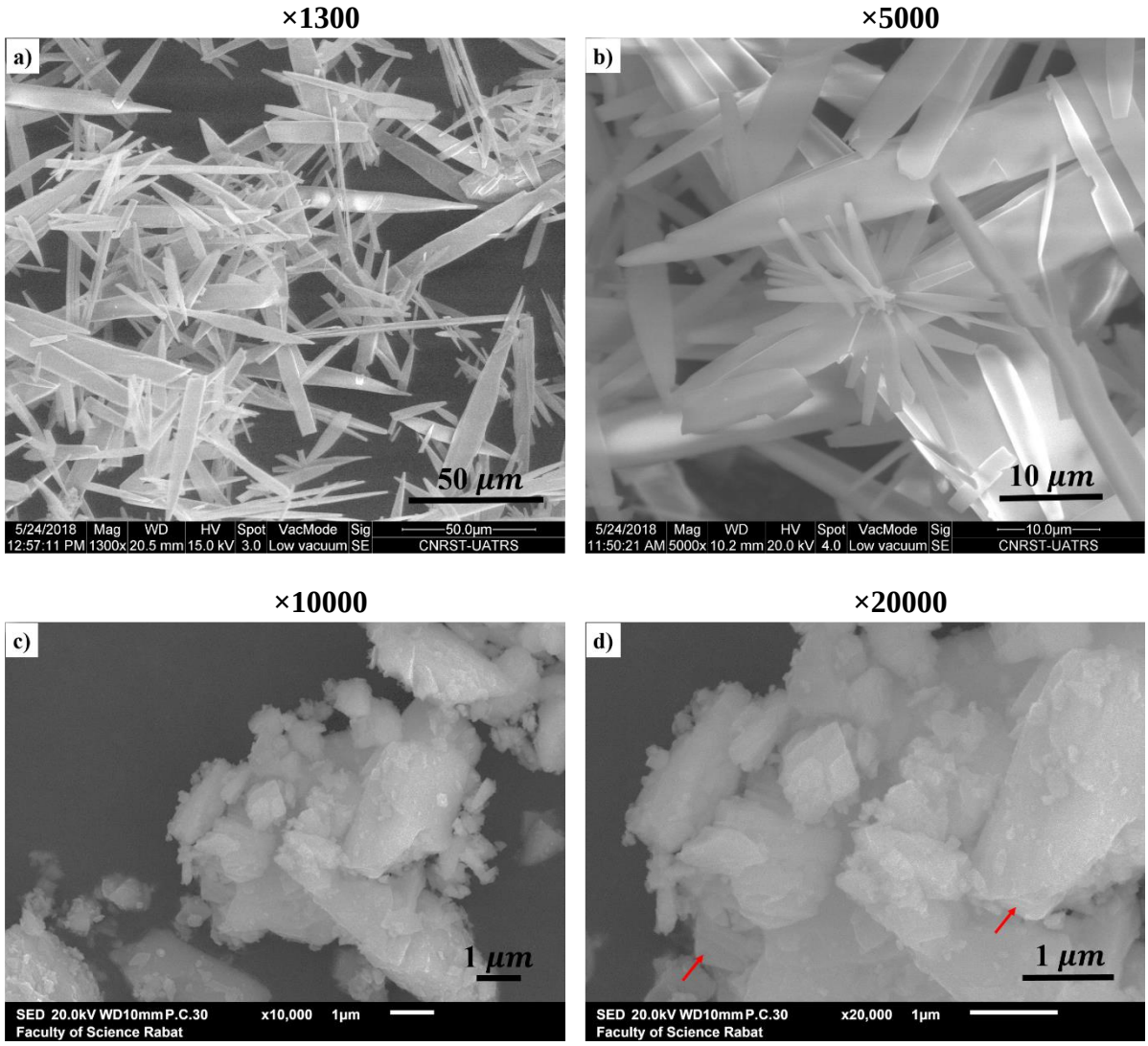

Figure A.III.3. SEM images of $SnHPO_3$ **a.** and **b.** as prepared, Magnifications ×1300 and ×5000, **c.** and **d.** after grinding, Magnifications ×10000 and ×20000

Energy dispersive X-Ray (EDX) analysis (**Figure A.III.4**) reveals the presence of exclusively Sn 23% (at.%), P 29% (at.%) and O 48% (at.%) and no other element was detected which confirms the purity of the sample. The EDX mapping was carried out for Sn, P and O elements. It shows that the areas colored with white and pink represent the high percentage of these elements in the sample. Comparing the three maps, one can conclude that there is a homogeneous distribution of these elements among the sample.

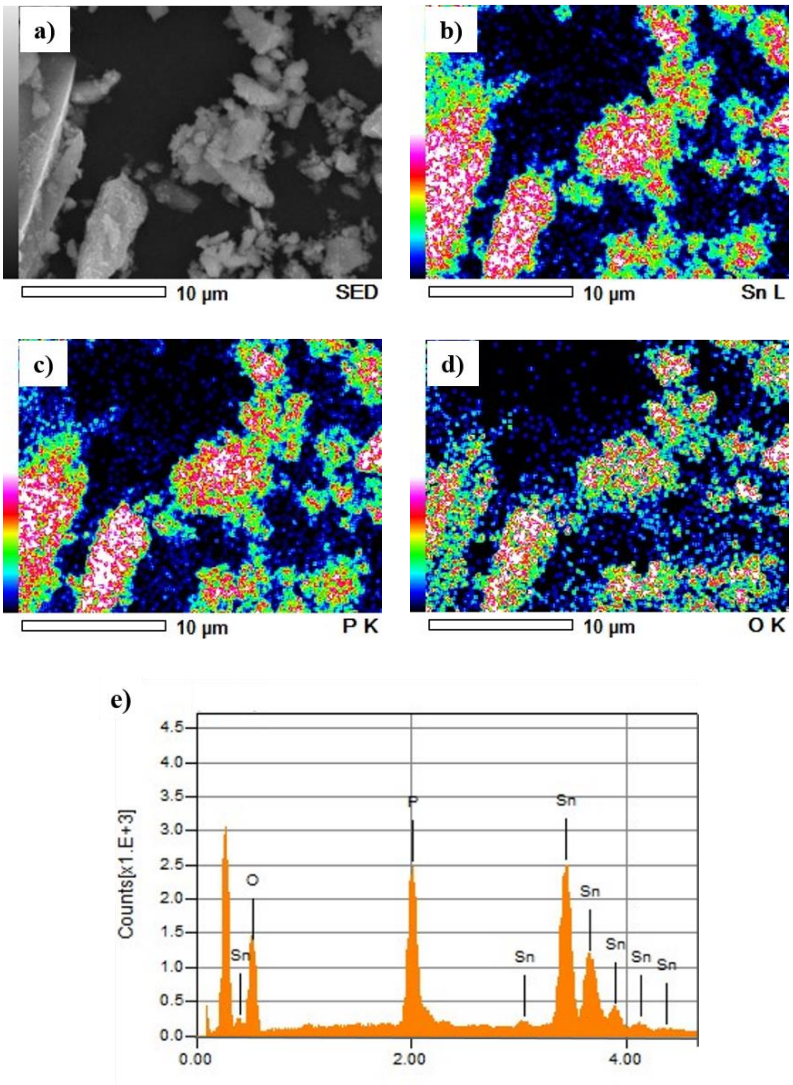

Figure A.III.4.a. SED image of $SnHPO_3$ **b. c.** and **d.** EDX mapping of Sn, P and O in $SnHPO_3$. The color scale varies from low (black) to high (white) concentration **e.** Element spectrum

III.1.2 Electrochemical measurements of $SnHPO_3$

Electrochemical characterization has been done using two different binders PVDF and CMC to evaluate the effect of each on $SnHPO_3$ electrochemical behavior. In this section we present galvanostatic cycling and cyclic voltammetry results of raw $SnHPO_3$.

III.1.2.1 Cyclic Voltammetry (CV)

Figure A.III.5.a. shows the cyclic voltammetry (CV) of the 1st three cycles for $SnHPO_3$ scanned in a potential range of 0.01 - 2.5 V with a scan rate of 0.01 mV/s using PVDF binder. All potentials are referred to Li^+/Li electrode. We observe three peaks during the first cathodic scan. One at around 1.3 V corresponding to the decomposition of tin phosphite upon initial

reaction with Li producing the reduction of the Sn^{2+} into metallic Sn and probably lithium phosphite phases. A second weak peak at 0.7 V, which corresponds to the formation of solid electrolyte interphase (SEI) layer. These two peaks only appeared in the first scan cycle indicating that the reaction occurring at this point is irreversible. Finally, the last cathodic peak observed at around 0.2 V corresponds to the formation of tin alloys Li_xSn. Whereas, upon the reverse anodic scan, a peak observed around 0.48 V is related to the dealloying of Li_xSn. These peaks are visible in the second and third cycles, revealing a reversible reaction.

This reversible reaction of Li alloying with Sn is presented below [105]:

$$xLi^+ + Sn + xe^- \leftrightarrow Li_xSn$$

Quite similar voltammetric profile has been obtained for tin (IV) pyrophosphate SnP_2O_7, based on literature studying the electrochemical behavior [64], [66], [106]. The three first cathodic peaks are often assigned to the electrolyte decomposition on the active anode surface to form the SEI and to the reduction of tin pyrophosphate to form irreversible lithium phosphate phases and metallic tin. Based on a ^{31}P MAS-NMR study, Edfouf et al. reported that the lithium phosphate matrix consists of $Li_4P_2O_7$ and Li_3PO_4 [63]. In our case, the precise electrochemical reactivity of the phosphite matrix is not yet known.

For CMC sample in **Figure A.III.5.b**, the first scan exhibits a quite similar voltammetry profile compared with PVDF. However, some differences can be noted. The reduction peaks around 1.3 V and 0.2 V and the oxidation peak at 0.49 V are sharper and more intense when using PVDF binder. This indicates that for this later, other irreversible reactions are probably happening during this first reduction.

In the next cycles for CMC, the reduction and oxidation peaks almost overlap, which shows the excellent cycling stability of electrodes using this binder. These features demonstrate that after expansion and shrink of active material, the electrode can still remain good electrical contact and ionic conductivity.

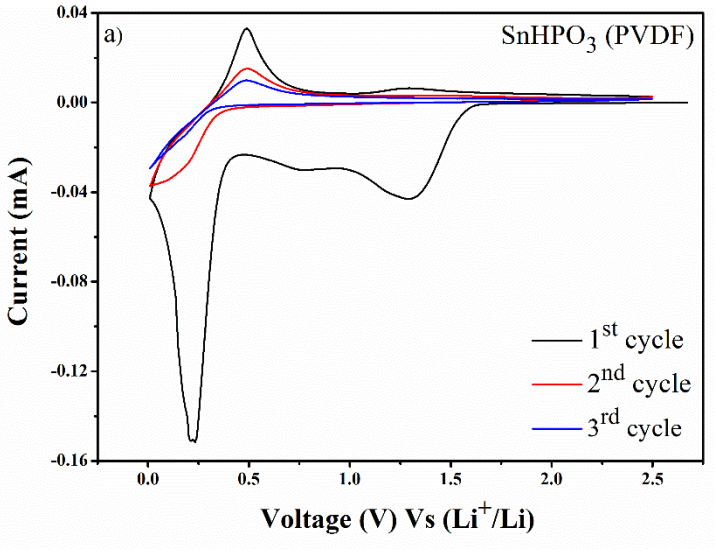

Figure A.III.5.a. Cyclic voltammograms (CV) results of tin phosphite $SnHPO_3$ using PVDF binder Vs Li^+/Li at 0.01 mV/s scan rate and 0.01 V - 2.5 V Vs Li^+/Li as voltage range

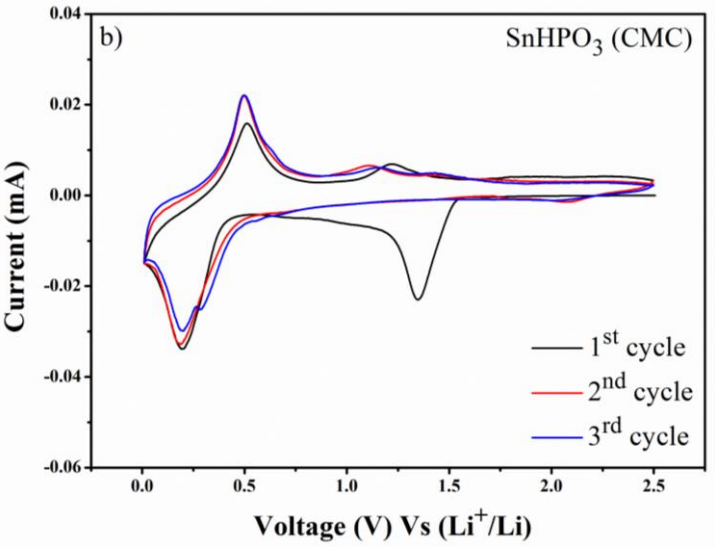

Figure A.III.5.b. Cyclic voltammograms (CV) results of tin phosphite $SnHPO_3$ using CMC binder Vs Li^+/Li at 0.01 mV/s scan rate and 0.01 V - 2.5 V Vs Li^+/Li as voltage range

In the CMC sample, one can observe a small oxidation peak around 1.2 V which is probably due to a re-oxidation of the lithium-phosphite matrix, as in the case of the mesoporous tin-phosphate [64] and lithium-oxide matrix in SnO_2 [11]. This peak is observed also for the second and third cycles in the case of CMC sample and only in the first cycle for PVDF sample. This is an indication of a quasi-reversible reaction of formation and deformation of lithium phosphite compounds.

III.1.2.2 Cycling performance

Figure A.III.6.a and **b** show the 1st, 2nd and 3rd cycles of the tin phosphite electrode $SnHPO_3$ using PVDF and CMC binders respectively at C/20. In this initial cycling, we suppose the insertion of one Li (x=1).

The processes of lithium ions insertion-de-insertion into $SnHPO_3$ can be divided into three stages. Upon discharging, one plateau at around 1.5 V is observed corresponding to the irreversible reduction of Sn^{2+} to metallic tin Sn^0 (Stage I) [106]. The region between 1.4 V and 0.5 V (Stage II) corresponds to the formation of a solid electrolyte interphase (SEI) layer on the surface of the active material and the lithium phosphite compounds [66]. In stage III, metallic tin is then cycled reversibly and forms lithium tin alloys Li_xSn, which corresponds to the second reversible plateau at 0.4 V [95].

Subsequent charging, a first reversible plateau at about 0.46 V is observed and is attributed to the dealloying of Li_xSn to metallic Sn and Li, followed by a second plateau at around 1.1 V mainly originates from the re-oxidation of the lithium phosphite matrix as observed in CV scans [107].

The discharge capacity of the electrode using PVDF fades rapidly from the initial 1247 mAh/g to 480 mAh/g in the second cycle. In contrast, the electrode using CMC binder shows higher capacity of 711 mAh/g in the second cycle. This first capacity loss is caused by the huge irreversible reaction between Li and tin phosphite and also by the formation of the SEI layer.

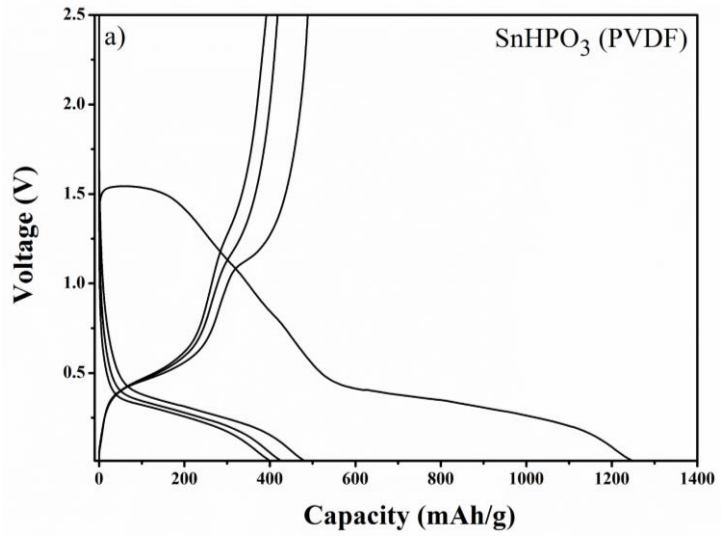

Figure A.III.6.a. Discharge-charge curves results of tin phosphite $SnHPO_3$ using PVDF binder at C/20 Vs Li^+/Li and a voltage range of 0.01 V - 2.5 V Vs Li^+/Li

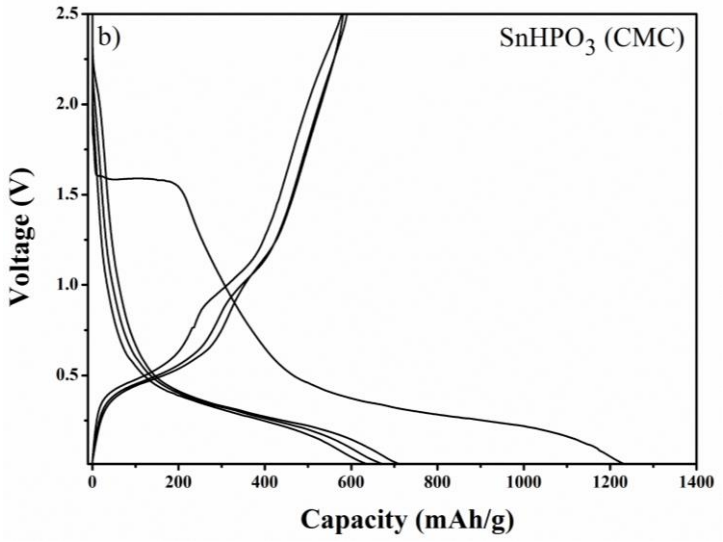

Figure A.III.6.b. Discharge-charge curves results of tin phosphite $SnHPO_3$ using CMC binder at C/20 Vs Li^+/Li and a voltage range of 0.01 V - 2.5 V Vs Li^+/Li

Figure A.III.7 compares the cyclability of both electrodes. The electrode using CMC binder displays a better cycle performance compared to that of using PVDF, indicating PVDF is not an effective binder for this kind of electrode. This is mainly attributed to the effective binding and better contact among the binder CMC and the active material. As a result, CMC supply a good accommodation for the huge volume change of tin during cycling and it is

proposed to be advantageous to stabilize the electrochemical performance, resulting in an interesting capacity retention.

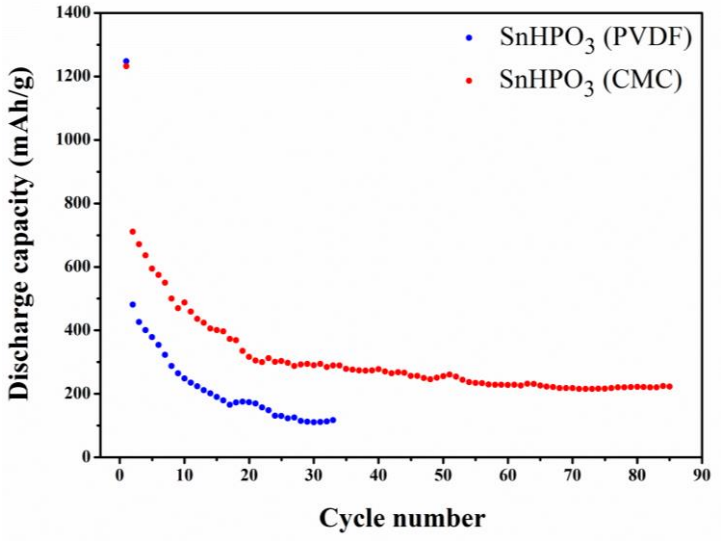

Figure A.III.7. Discharge capacity Vs cycle number results of tin phosphite $SnHPO_3$ using PVDF binder (blue) or CMC binder (red) at C/20 Vs Li^+/Li and a voltage range of 0.01 V - 2.5 V Vs Li^+/Li

Figure A.III.8 shows the cyclability of tin phosphite $SnHPO_3$ using CMC at two different rates C/5 and C/50. In this result we suppose the insertion of eight Li (x=8). The figure demonstrates that the use of CMC binder can help maintaining the capacity at about 300 mAh/g from the 30^{th} cycle and up to 100^{th} cycle which is consistent with the previous results.

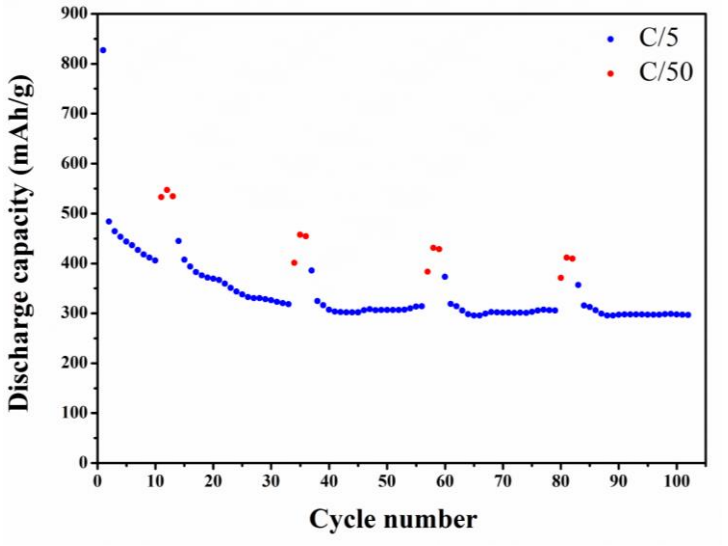

Figure A.III.8. Discharge capacity Vs cycle number results of tin phosphite $SnHPO_3$ using CMC binder at C/5 (blue) and C/50 (red) Vs Li^+/Li with x = 8 and a voltage range of 0.01 V - 2.5 V Vs Li^+/Li

In order to further improve the electrochemical performance of raw tin phosphite, we have synthesized its composite with reduced graphene oxide. This latter is known to enhance the electrical conductivity within the electrode and to accommodate the volume expansion of tin element during cycling. In the following, structural, morphological and electrochemical characterizations of the composites using different GO percentage are given in comparison with raw $SnHPO_3$.

As a result of the comparison study done on raw tin phosphite using different binders, we have decided to use CMC binder to prepare the slurries used to test electrochemical performances of the following composite materials.

III.1.2.3 *In situ* XRD analysis of $SnHPO_3$ electrode

In order to investigate the lithium extraction/insertion mechanism of the $SnHPO_3$ electrode, *in situ* XRD was performed, in Materials Science and Nano-engineering (MSN) laboratory at Mohammed VI Polytechnic University (UM6P), Ben Guerir, Morocco, according to the following protocol:

A specific in situ cell composed with a beryllium window and electrically insulated, was assembled in an argon-filled glove box with H_2O and O_2 contents below 0.01 ppm, using 70% of the active material and 30% black carbon with lithium metal as anode. The electrolyte

was 1 M $LiPF_6$ in ethylene carbonate (EC) and dimethyl carbonate (DMC) with 1:1 v/v. Whatman GF/D borosilicate glass fibres was used as separator. After assembling, the cell are connected to a potentiostat (Biologic SP150 type measurement) and placed in a Bruker D8 DISCOVER diffractometer, with copper $k_{\alpha 1}$ radiation (λ = 1.54056 Å). A galvanostatic discharge/charge cycle is carried out at C/5 rate, between 0.01 V and 2.5 V Vs Li^+/Li. The diffraction patterns were collected at room temperature, every 30 min in 2θ angular ranges 10°-28° and 29°-45°. **Figure A.III.9** shows the *in situ* X-Ray diffractograms obtained during the first cycle of discharge and charge as well as the corresponding galvanostatic curves.

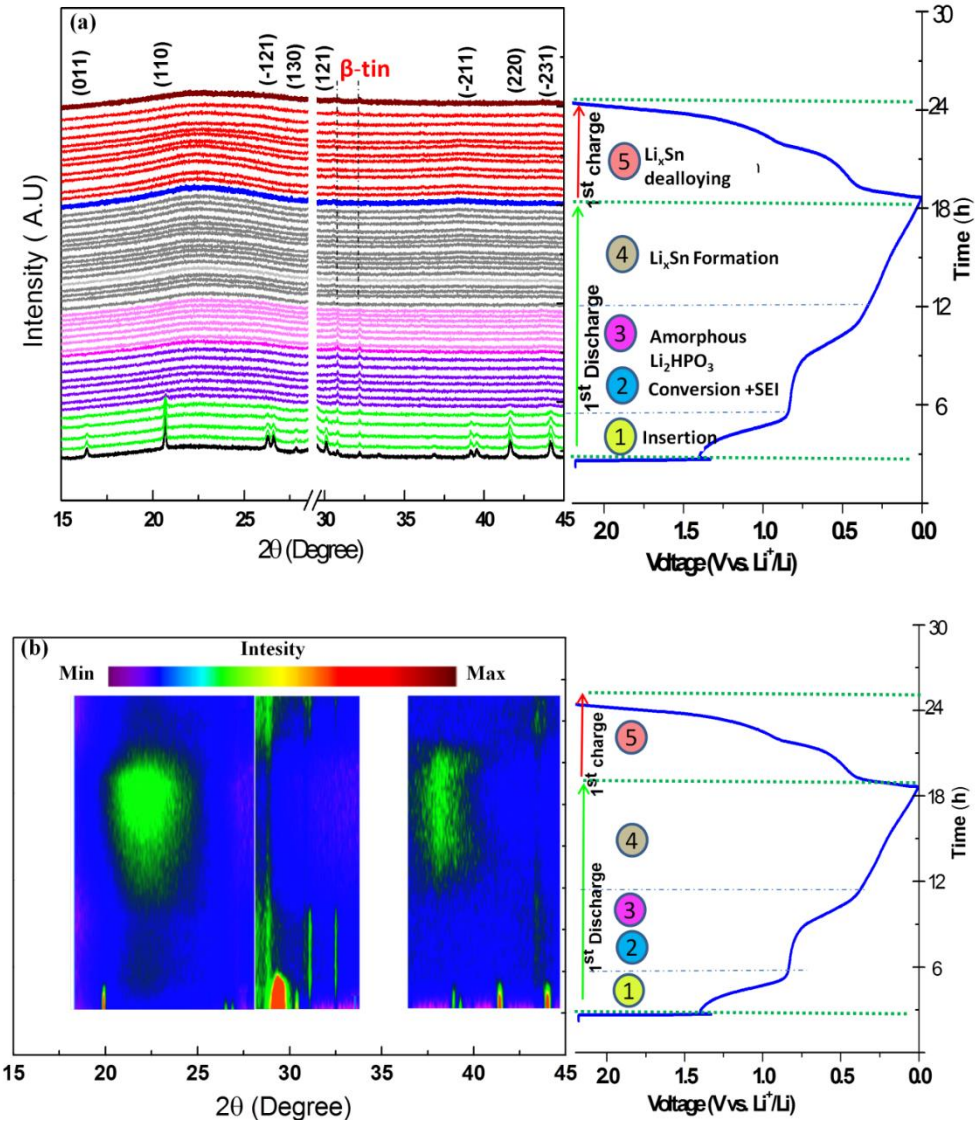

Figure A.III.9.a. *In situ* XRD of the $SnHPO_3$ electrode during the first cycle in the voltage window of 2.5 V - 0.01 V Vs Li^+/Li **b.** High resolution *In situ* XRD of the $SnHPO_3$ electrode during the first cycle in the voltage window of 2.5 V - 0.01 V Vs Li^+/Li

To better understand the structural evolution of $SnHPO_3$ during the first cycle of discharge and charge, we can divide the electrochemical reactions sequence, based on *in situ* X-Ray diffractograms as well as the corresponding galvanostatic curves into four stages (**Figure A.III.9**):

- **Stage 1: 2.5 V - 0.7 V**

We observe that all peaks belong to the monoclinic phosphite structure of the pristine material from the beginning of the discharging process until the 0.7 V with same diffraction peaks located at the identical 2θ positions. We notices on the difractogramms at the discharge starting two packs with very weak intensity located at 30.70° and 32.08°, corresponds a typical reflections of β-Sn structure (Tetragonal system with space group *I*41 /amd and unit cell parameters a = 5.8190 Å and c = 3.1753 Å in good agreement with the expert highscor PDF # 001-0926 of β-Sn . The existence of the β-Sn phase with small amount is probably due to the partial reduction of Sn^{2+} cations to the Sn metallic state, by the effect of carbon and manual grinding. No significant shift in 2θ was observed on the in situ X-Ray diffractograms and no sudden appearance of other peaks was observed, this implying an electrochemical solid solution reaction mechanism associated in potential range 1.5 V - 0.7 V. This phenomenon can be assigned to the intercalation of Li ions into the tin phosphite structure without destroying it. The unit cell volume structure corresponding of the X-Ray diffractograms in solid solution restricted range (Sloping profile part) was calculated by Bail method using the Rietveld technique (**Figure A.III.10.a**). The results are illustrated in Figure **A.III.10.b**. Essentially, a slight increase in the cell volume is observed (350.4 $Å^3$ at 1.5 V to 352 $Å^3$ at 0.7 V), corresponding to a very small volume change (> 1%).

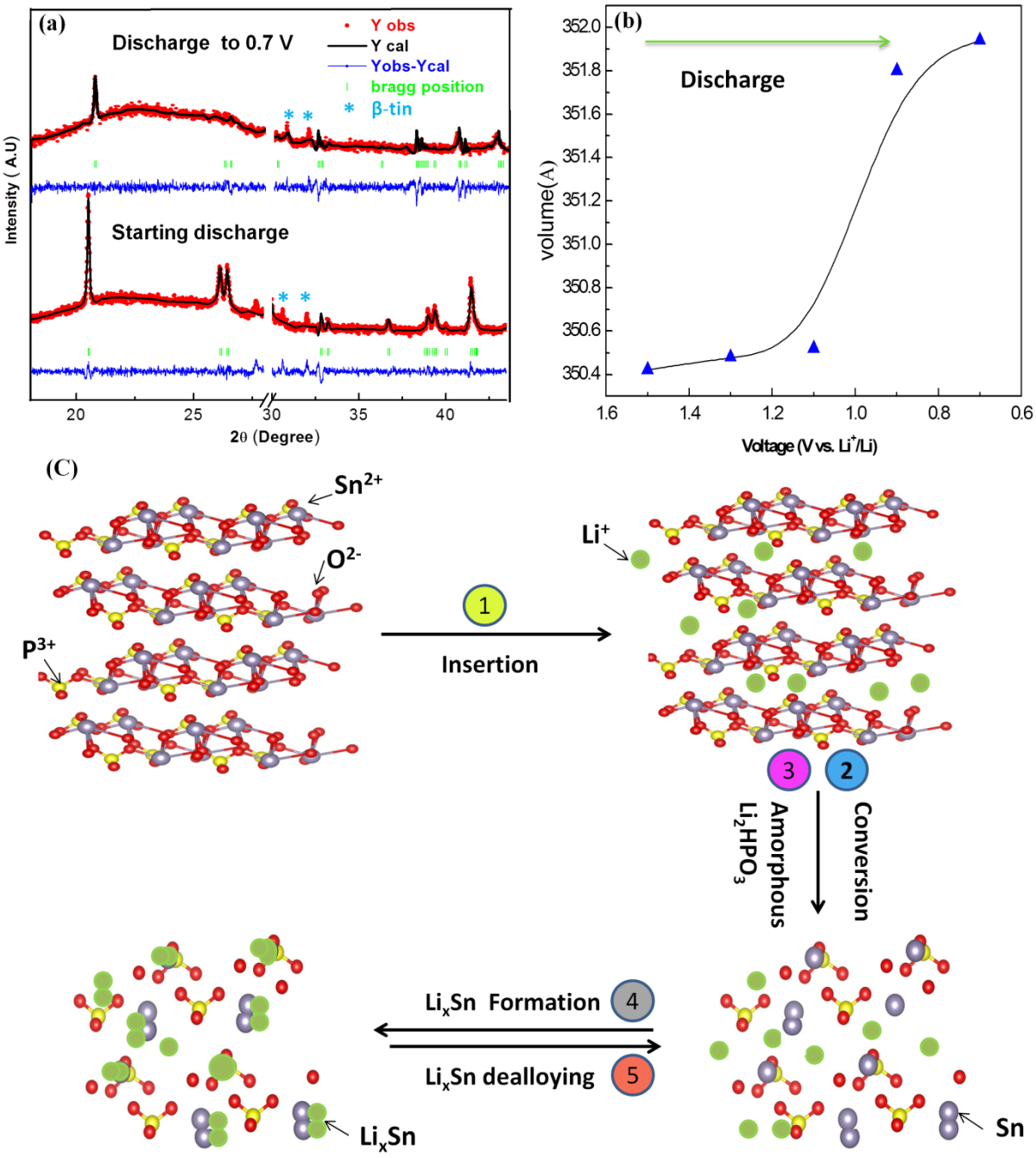

Figure A.III.10.a. Rietveld refinements of *in situ* XRD data of $SnHPO_3$ electrodes at starting discharge and at the discharged to 0.7 V of $SnHPO_3$ **b.** Lattice volume variation versus potential in the lithium ions insertion range of $SnHPO_3$ **c.** Illustrative schema of structure evolution of $SnHPO_3$ during the first cycle of discharge-charge

This slight increase in volume is directly related to the progressive occupation by the lithium ions between the host structure located in parallel planes to (a, c). In this step, $SnHPO_3$

reacts with Li to form a lithium phosphite matrix while the Sn (II) is reduced to metallic Sn, according to the following electrochemical reaction:

(1) $SnHPO_3 + xLi^+ + xe^- \rightarrow Li_xSn_{1-0.5x}^{2+}HPO_3 + 0.5xSn^0$

The maximum lithium amount inserted into the host structure of $SnHPO_3$ was drawn into the discharge capacity at the end of solid solution part (at potential 0.7 V) of the first discharge in galavanostatic curve, (knowing that the maximum theoretical capacity of $SnHPO_3$ corresponding to the exchange of two lithium per formula is equal to 270 $mAhg^{-1}$) this quantity of capacity is equal to 25 mAh/g which is equivalent to $x \approx 0.18$ per formula as the maximum quantity of lithium ions per formula can be inserted before the host structure destruction, according to the following equation:

(2) $SnHPO_3 + 0.18Li^+ + 0.18e^- \rightarrow Li_{0.18}Sn_{0.91}HPO_3 + 0.09Sn^0$

- **Stage 2 and 3: 0.7 V - 0.4 V**

No reflections from $SnHPO_3$ are detected in the diffraction pattern in this range, while a large diffusion peak representing the amorphous fraction of the composite appears in the range $20° \leq 2\theta \leq 28°$.

Reflections from β-Sn phase are also presented. This step is accompanied by irreversible reduction of the Sn (II) in phosphite to tin metal Sn (0), and a conversion of the phosphite matrix, where the HPO_3^{2-} units are reacting with Li to form at the end an amorphous phase as described in following electrochemical reaction below:

(3) $Li_{0.18}Sn_{0.91}HPO_3 + 0.82Li^+ + 0.82e^- \rightarrow 0.91Sn^0 + Li_2HPO_3$ (amorphous)

This step is also accompanied by the formation of a passivation layer solid electrolyte interphase (SEI) owing to electrolyte decomposition on the electrodes. The octahedral asymmetry hosted by Sn^{2+} cations caused by second order Jahn-Teller distortions (SOJT) is the main reason of the lithium insertion limit and conversion of $SnHPO_3$ phosphite matrix [89].

- **Stage 4: below 0.4 V**

Below a potential of 0.4 V until the end of discharge processes, the peaks intensities of β-Sn are completely disappeared at the end of the discharge step. This behavior can be due to the amorphization of phosphite matrix in the electrode material during lithiation presses and the

subsequent formation of the lithium tin alloys (Li_xSn). Tin is then cycled reversibly and forms lithium tin-alloys. The reversible reaction of lithium with tin [105] described in following redox reaction below:

(4) $xLi^+ + Sn + xe^- \rightarrow Li_xSn$

Schema on **Figure A.III.10.c** summarized structure evolution of the $SnHPO_3$ during the first cycle of discharge.

- **Stage 5 (charging process)**

During the charging process no peaks reappear in X-Ray diffractogramm, the material stays amorphous electrochemically active. These phenomena can be due to the amorphization and re-oxidation of tin phosphite. Any other phase recrystallized in the electrode material during the charging process. The subsequent dealloying of Li_xSn to metallic Sn and Li according to the following RedOx reversible reaction:

(5) $Li_xSn \rightarrow xLi^+ + xe^- + Sn$

III.2 Characterizations of tin phosphite/reduced graphene oxide composites ($SnHPO_3$/RGO)

III.2.1 Structural and morphological characterizations of $SnHPO_3$/RGO composites

III.2.1.1 X-Ray Diffraction (XRD)

Figure A.III.11 shows X-Ray patterns resulting from various $SnHPO_3$/RGO composites containing different amounts of reduced graphene oxide (RGO). For comparison the pattern of pure RGO has been added. All composite samples containing 3%, 5%, 8% and 10% of RGO show the presence of the $SnHPO_3$ diffraction peaks with no secondary phase. The characteristic peak of reduced graphene oxide ($2\theta = 24.2°$) is not visible on these composites due its low amount. However, the sample with 90% of RGO shows only the peak corresponding to RGO due to the low amount of $SnHPO_3$ present.

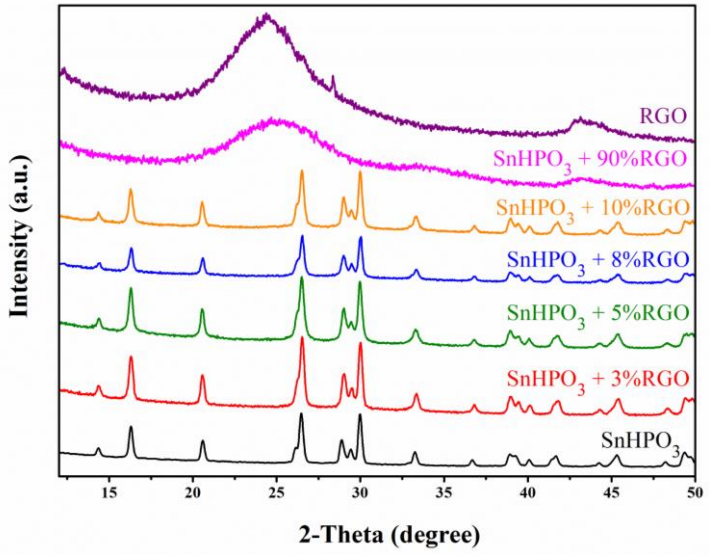

Figure A.III.11. XRD pattern of pristine $SnHPO_3$ and $SnHPO_3$/RGO composites

III.2.1.2 Fourier Transform Infrared Spectroscopy (FTIR)

Figure A.III.12 presents the FTIR spectrum of the $SnHPO_3$/RGO composites with 3%, 5%, 8% and 10% of RGO in comparison with pure RGO. The bands corresponding to the vibrations of the phosphite oxo-anions are still observed in all the composites as shown in **Figure A.III.2** The spectrum of RGO indicates specific bands at 1996 cm^{-1} and 2100 cm^{-1} corresponding to C=C bond [108]. These two bands are present in all the composites.

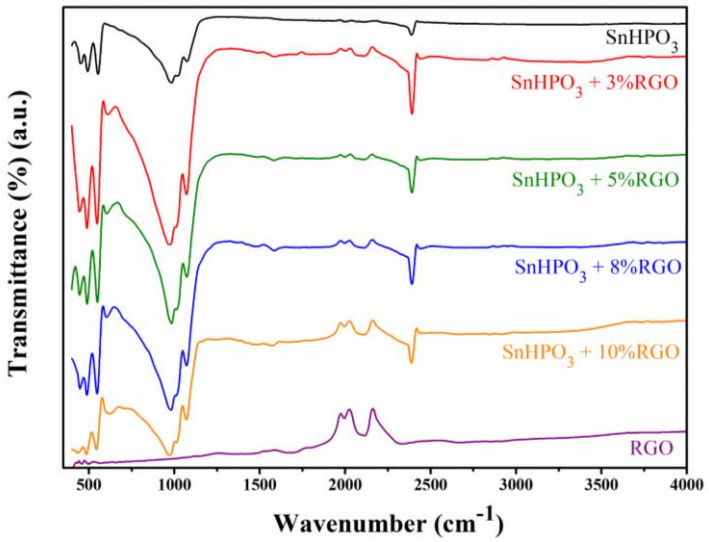

Figure A.III.12. FTIR spectrum of raw $SnHPO_3$ and $SnHPO_3$/RGO composites

Table A.III.3. Wavenumbers and attributions of vibration modes of $SnHPO_3$/RGO composites

Wavenumbers (cm^{-1})	**Assignments**	**Reference**
2391	υ(P-H)	[103]
2100	υ(C=C)	[108]
1996	υ(C=C)	[108]
1071	υ_{as}(P-O)	[104]
1019	δ(P-H)	[103]
970	υ_{s}(P-O)	[104]
550 - 451	δ_{s}(P-O) and δ_{as}(P-O)	[104]

III.2.1.3 Scanning Electron Microscopy (SEM)

SEM images of all $SnHPO_3$/RGO composites with 3%, 5%, 8% and 10% of RGO at different magnifications ×5000, ×10000 and ×20000 are shown in **Figure A.III.13**. All the composite samples have been grinded manually using agate mortar before analysis. This random grinding causes a difference on the powders aspect. All the composite samples have shown particles of different shapes and sizes. However, overlapping sheets observed in pristine $SnHPO_3$ are still present even after adding reduced graphene oxide. Neither the transparent RGO sheets nor their effect on the particles morphology are visible on the images. This can be due to the low amount of GO added to the composite.

The EDX mapping was carried out for Sn, P, O and C elements for all composites. **Figure A.III.14** shows the corresponding results. Areas colored with white and pink represent the high percentage of these elements in the sample.

Element mapping of Sn, P and O show a homogeneous distribution of these elements in all the composites surfaces. The images can be even overlapped showing the presence of $SnHPO_3$ phase. As for carbon element, it seems to be homogeneous with the other elements in 3%, 5% and 10% composites but not in the 8% one. The distorted distribution of carbon element in this last sample is probably due to the presence of the conductive carbon adhesive tape on the upper right of the image.

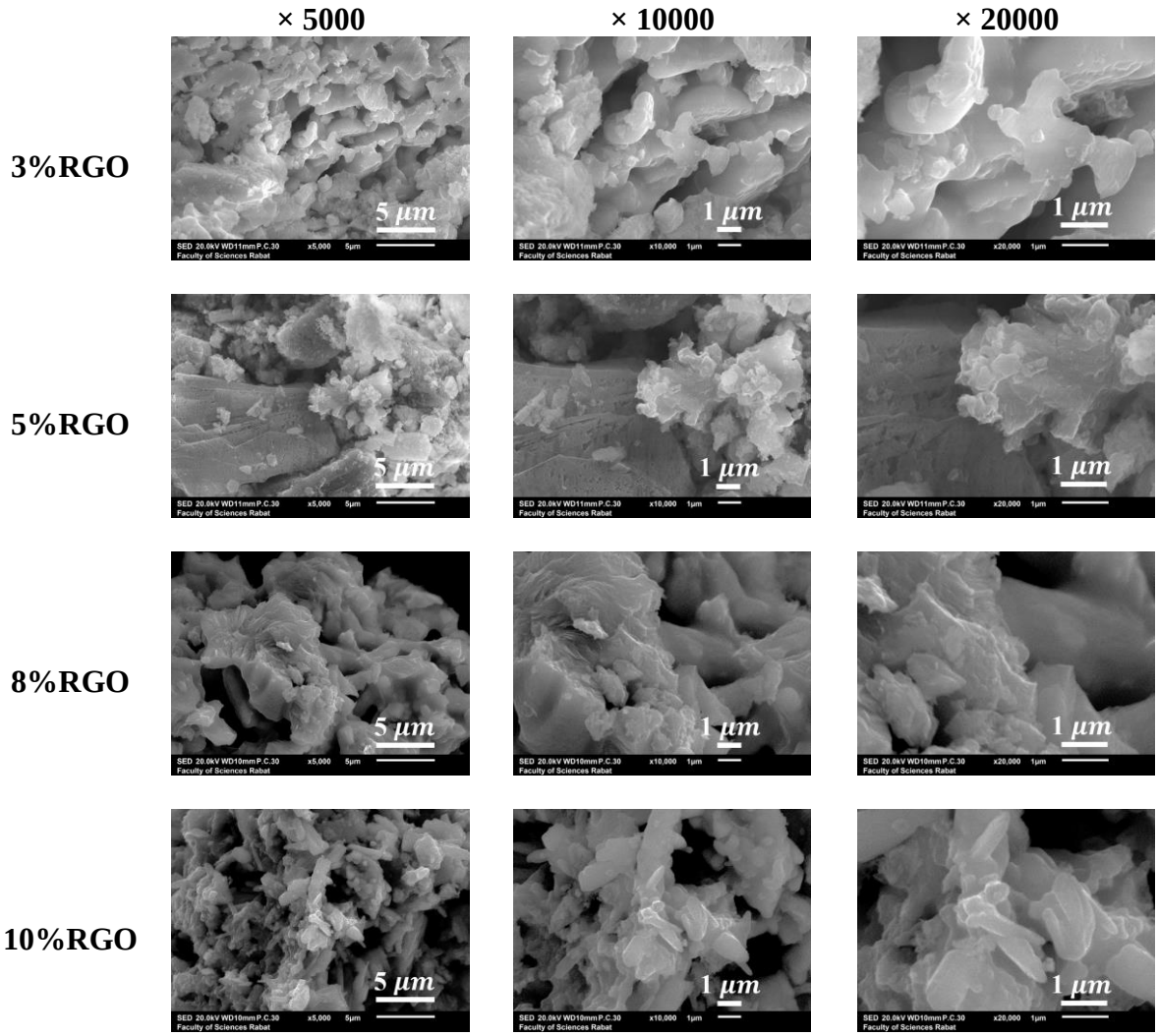

Figure A.III.13. SEM images of $SnHPO_3$/RGO composite with 3%RGO, 5%RGO, 8%RGO and 10% RGO, Magnifications ×5000, ×10000 and ×20000

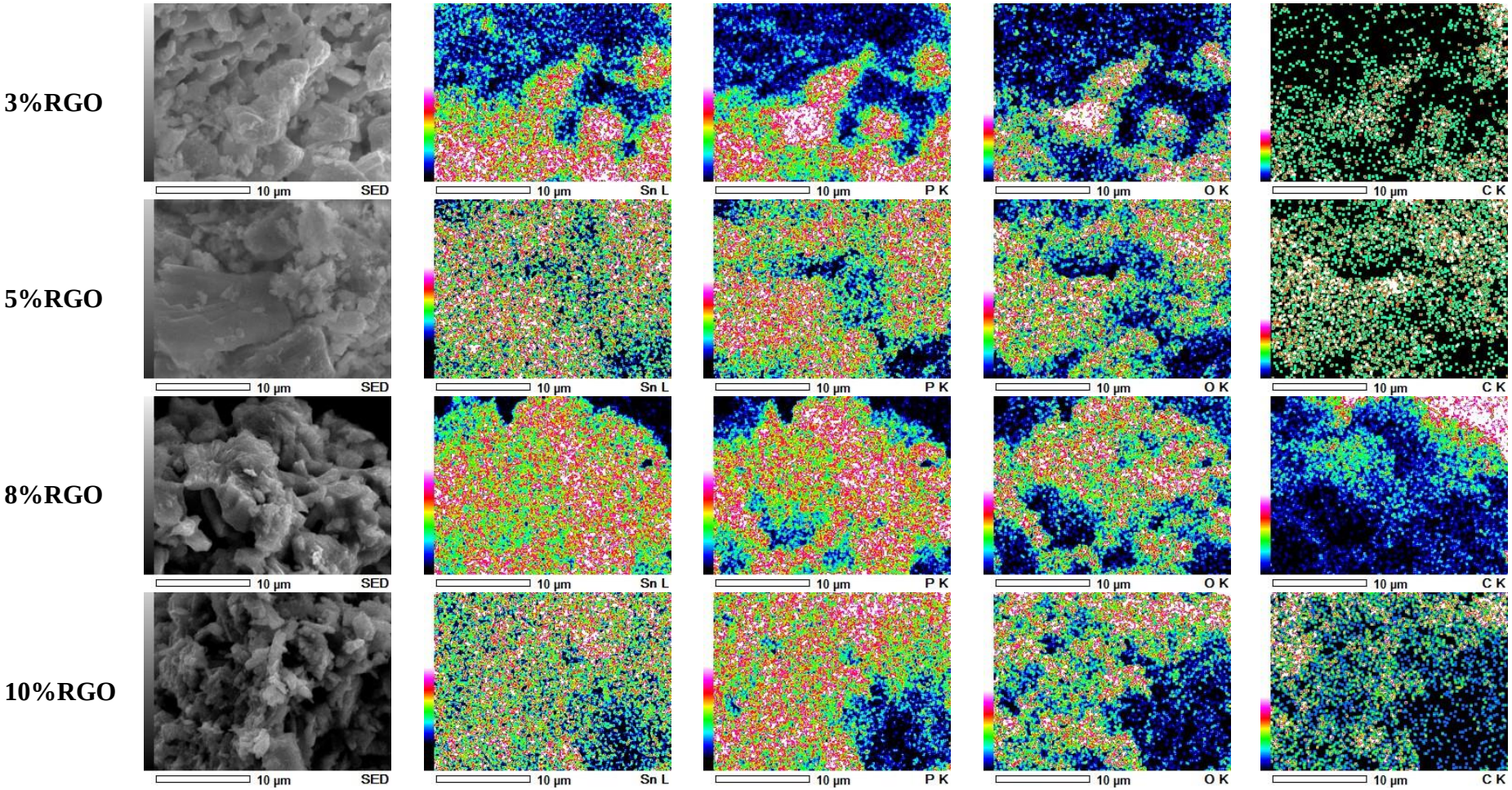

Figure A.III.14. SED image of $SnHPO_3$/RGO composite with 3%RGO, 5%RGO, 8%RGO and 10%RGO, and EDX mapping of Sn, P and O in $SnHPO_3$. The color scale varies from low (black) to high (white) concentration

III.2.2 Electrochemical measurements of $SnHPO_3$/RGO composites

Electrochemical measurements for $SnHPO_3$/RGO composites has been carried out using CMC binder. In this section, we present galvanostatic cycling and cyclic voltammetry results of $SnHPO_3$/RGO composite with different percentage of reduced graphene oxide (RGO): 3%, 5%, 8%, 10% and pure reduced graphene oxide (RGO).

III.2.2.1 Cyclic Voltammetry (CV)

Figure A.III.15 shows the cyclic voltammetry (CV) of the 1st three cycles for $SnHPO_3$/RGO composites scanned in a potential range of 0.01 V - 2.5 V with a scan rate of 0.01 mV/s using CMC binder. All potentials are referred to Li^+/Li electrode.

One can note that the intensity of CV profiles are quite different when adding RGO. Redox peaks seem to be more intense with higher RGO quantities showing a better reactivity within the composite. When it comes to the peaks position, the $SnHPO_3$/RGO composites with 3%, 5%, 8% and 10% of RGO present a similar mechanism compared to the one of raw $SnHPO_3$. The first irreversible cathodic peak at 1.3 V, which corresponds to the decomposition of tin phosphite, is also observed in the $SnHPO_3$/RGO composites with 3%, 5%, 8% and 10% of RGO and as the percentage of RGO increase the peak is more intense. As for the pure RGO, this peak disappears completely.

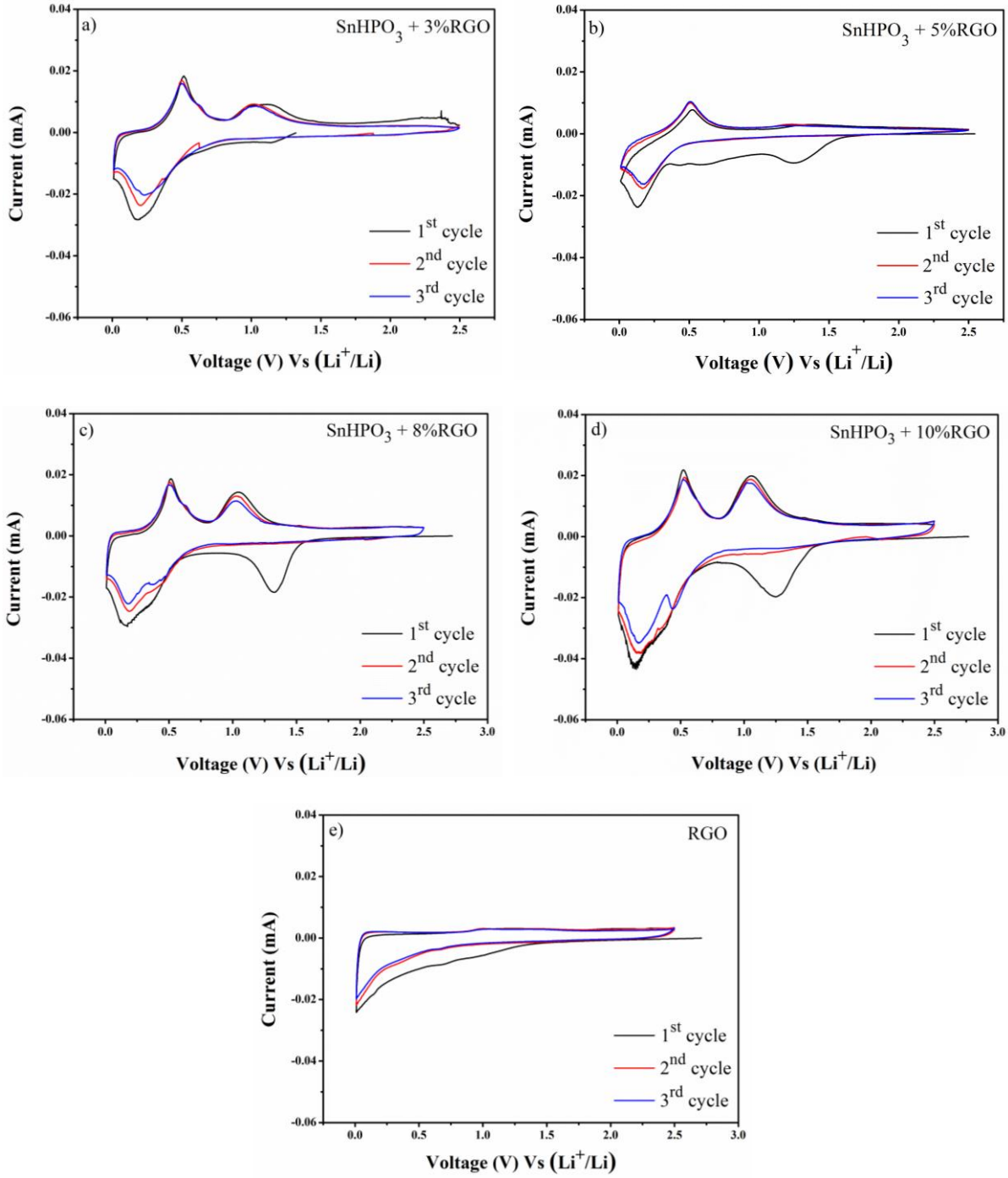

Figure A.III.15. Cyclic voltammograms (CV) results of tin phosphite $SnHPO_3$/RGO composites using CMC binder Vs Li^+/Li at 0.01 mV/s scan rate and 0.01 V - 2.5 V Vs Li^+/Li as voltage range **a.** $SnHPO_3$ + 3%RGO **b.** $SnHPO_3$ + 5%RGO **c.** $SnHPO_3$ + 8%RGO **d.** $SnHPO_3$ + 10%RGO **e.** Reduced graphene oxide (RGO)

III.2.2.2 Cycling performance

Figure A.III.16 shows a comparison of the 1st cycle of both pristine tin phosphite $SnHPO_3$ and tin phosphite composite $SnHPO_3$/RGO with 3% of RGO using CMC binder at C/10, and supposing the insertion of one Li (x=1). The processes occurring during the lithium ions insertion-de-insertion observed in **Figure A.III.6** are present in the two profiles, with the increasing of the discharge and charge capacities after adding reduced graphene oxide. These results prove that reduced graphene oxide play an important role in enhancing the electrochemical performance of the tin phosphite electrode.

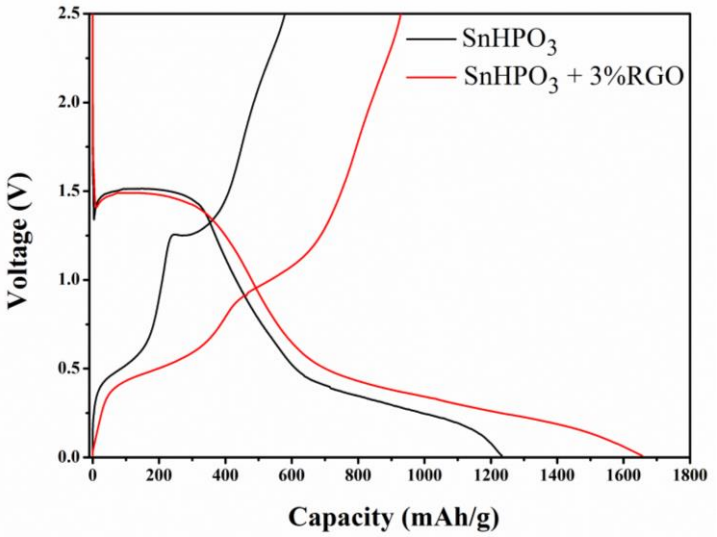

Figure A.III.16. Discharge-charge curves results of the first cycle of $SnHPO_3$ and $SnHPO_3$ + 3%RGO using CMC binder at C/10 Vs Li^+/Li and a voltage range of 0.01 V - 2.5 V Vs Li^+/Li

The cycling performance of all the $SnHPO_3$/RGO composites at C/10 is compared in **Figure A.III.17**. As it can be seen, all composites show a quite similar profile compared to the raw $SnHPO_3$. One can observe that $SnHPO_3$/RGO composites with 5% and 8% of RGO deliver the highest discharge capacity during the first cycle, reaching 2387 mAh/g. In the second and third cycles, $SnHPO_3$/RGO composite with 8% of RGO presents higher discharge capacities compared to $SnHPO_3$/RGO composite with 5% of RGO.

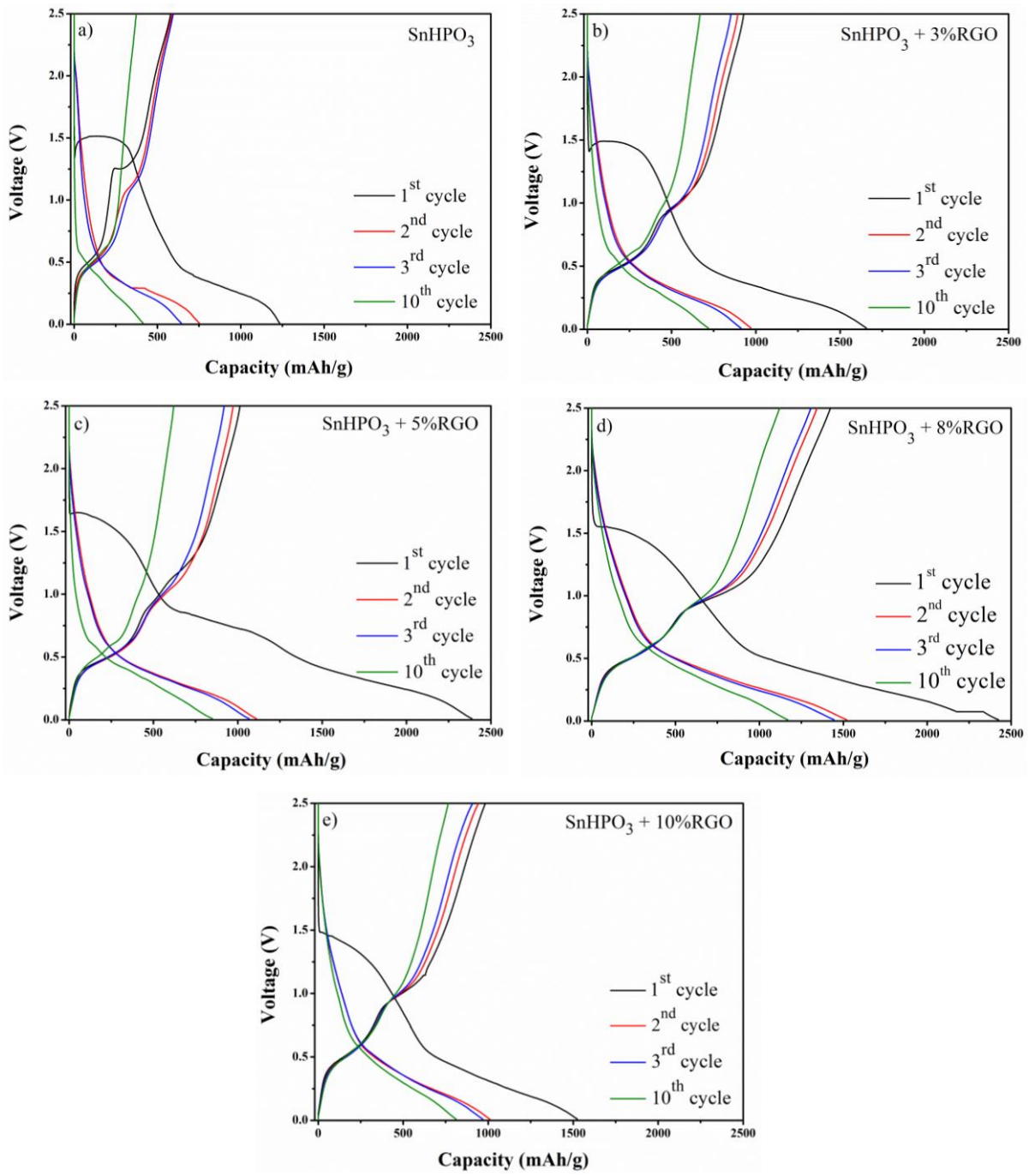

Figure A.III.17. Discharge-charge curves results of tin phosphite $SnHPO_3$/RGO composites using CMC binder at C/10 Vs Li^+/Li and a voltage range of 0.01 V - 2.5 V Vs Li^+/Li **a.** $SnHPO_3$ **b.** $SnHPO_3$ + 3%RGO **c.** $SnHPO_3$ + 5%RGO **d.** $SnHPO_3$ + 8%RGO and **e.** $SnHPO_3$ + 10%RGO

Figure A.III.18 compares the cyclability of the $SnHPO_3$/RGO composites. The sample with 8%RGO shows a rapid fade of its capacity to 17 mAh/g over the 100th cycle. It is the

$SnHPO_3$/RGO composite with 5% of RGO that shows the most stable cycling performance compared to the other composites. As the electrode reaches the 15th cycle, the discharge capacity remains stable at ≈ 500 mAh/g. It still can deliver this capacity over the 100th cycle. These results proves that the optimal amount of RGO that can be added to the pristine $SnHPO_3$ is 5% to obtain a stable electrochemical performance and higher capacity retention.

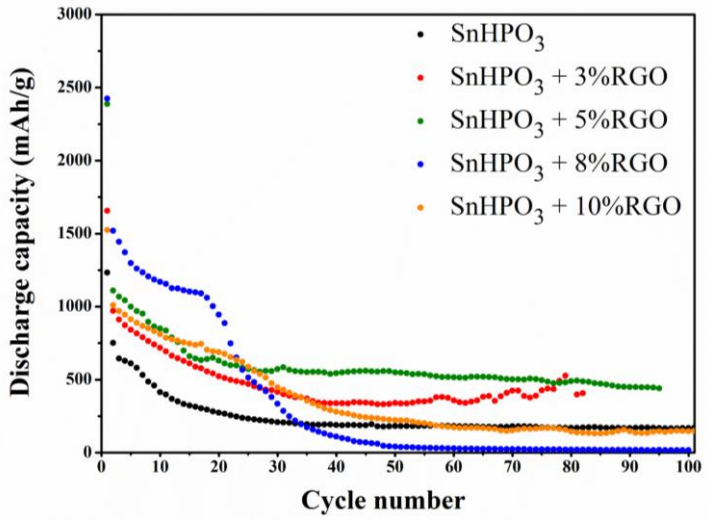

Figure A.III.18. Discharge capacity Vs cycle number results of tin phosphite $SnHPO_3$/RGO composites using CMC binder at C/10 Vs Li^+/Li and a voltage range of 0.01 V - 2.5 V Vs Li^+/Li

Conclusion

Tin phosphite $SnHPO_3$ synthesized using the hydrothermal method has been tested for the first time by our team as anode material for LIBs. The structural and morphological characterizations and the electrochemical performances of this electrode have been investigated.

Structural characterization of the active material shows good agreement between experimental and simulated patterns in XRD. Phosphite groups have been confirmed by FTIR analysis.

Understanding the electrochemical behavior mechanism have been comparatively investigated using traditional binder PVDF and water-soluble binder CMC. Cyclic voltammetry and galvanostatic cycling results obtained showed clearly that CMC binder has allowed a better behavior of $SnHPO_3$ as anode material in comparison with PVDF binder. This is due to its volume change accommodation in tin phosphite electrode during cycling, also to the lower irreversible capacity during the first cycle allowing a higher reversible capacity during the following cycles. As a result, CMC, thanks to its chemical formula, further improves the electric conductivity, mechanical strength and thus, the cycle performance of the battery. Thereby, the use of CMC binder is efficient and beneficial for the $SnHPO_3$ material to achieve good anode performance and to develop cost effective and sustainable batteries.

To further optimize the electrochemical performances of tin phosphite electrode, we have synthesized other tin phosphite based materials using graphene oxide and with the same hydrothermal method. The choice of this composite is based on the high theoretical capacity of tin, on the open framework structure of phosphite and on the good electronic conductivity of graphene.

The obtained results proved that reduced graphene oxide plays an important role in enhancing the electrochemical performance of tin phosphite electrode. The $SnHPO_3$/RGO composite with 5% of RGO showed the most stable cycling performance compared to the other composites, which can deliver higher and stable discharge capacity of ≈ 500 mAh/g over the 100^{th} cycle compared to other composites with different percentage of RGO.

The good cycling stability and the high discharge capacity of this electrode make our material a potential candidate as an anode for Li-ion batteries. The originality of this work was to propose tin phosphites $SnHPO_3$ and $SnHPO_3$/RGO as a new class of anode material for lithium-ion batteries.

In order to investigate the depth of the lithium extraction/insertion mechanism in tin phosphite $SnHPO_3$ electrode, *in situ* X-Ray measurements were performed and discussed. This analysis showed that the lithiation delithation of tin phosphite proceeded into a complex Redox reaction sequence, started at high potential by progressive incorporation of Li into the tin phosphite host structure, and $SnHPO_3$ reacted with Li to form a lithium phosphite matrix. Then the phosphite matrix amorphized, and the lithium tin alloys (Li_xSn) reversible system occurred at low potential of discharge processes. De-alloying of Li_xSn to metallic Sn and Li are also detected in the charging process without any phase recrystallized. The existence of the amorphous, in situ X-Ray measurements are limited to detect the nature and chemical composition of the alloys and the amorphous phase formed during lithiation/delithiation of tin phosphate. Therefore, the perspectives of our work will consist in completing these studies by in situ Sn Mossbauer and ex situ FTIR measurements and optimizing all the parameters necessary for the development of new high performance composite materials.

Part B:

Oxygen reduction reaction (ORR) on doped and un-doped reduced graphene oxide

Introduction

Metal-air batteries have been targeted as a promising technology to meet the energy requirements for future electric vehicles and other energy demanding devices, thanks to their various advantages such as high energy density, light weight and environmental friendliness [109], [110].

Oxygen reduction reaction (ORR) is one of the key steps in these systems. The development of efficient electrocatalysts for the oxygen reduction reaction (ORR) with good quality, low price and environmental friendliness is highly urgent for the commercialization of metal-air batteries [111]. Traditional Platinum-based catalysts are the most active ORR catalysts. However, the rareness and high cost of Pt limit the large-scale production and commercialization of the metal-air battery technology [112]. Therefore, it is extremely desirable and challenging to explore low cost, stable and high performance electrocatalysts for oxygen reduction reaction (ORR) to accelerate the practical applications of metal-air batteries. Thus, many research studies on non-precious metal catalysts have been developed as alternatives for the expensive platinum /carbon catalysts [113], [114].

Graphene, one of the most promising 2D materials, stands out as a new-generation carbon support owing to its high electrical conductivity, high thermal and chemical stabilities, high surface area, and strong adhesion to active catalyst nanoparticles [115], [116]. Graphene itself is a great alternative as an electrocatalyst for ORR. However, 2D graphene sheets easily reaggregate or restack during drying due to physical interactions (e.g. van der Waals forces and π-π stacking). Which significantly reduces the accessible surface area and limits electron transport. Besides, graphene usually possess a limited number of reactive sites, which result in a low catalytic activity. Therefore, there is still a big challenge to further optimize its electrocatalytic performance [117].

Major efforts have been made to use electrode materials based on it. Many promising noble metal-free catalysts for ORR application are synthesized. As an example, doping graphene with nitrogen, which demonstrates outstanding ORR activity and good stability in alkaline solution, as published in recent reviews [118]–[120]. Phosphorus as well, is considered as a great candidate for doping graphene, since it has a lower electronegativity than carbon and a higher electron-donating ability [121]. Thus, it is of great interest to explore the unique properties of phosphorus doped graphene.

Co-doping graphene is also interesting. It has been demonstrated that ORR activity was improved by modifying the electronic properties and surface polarities using co-doped graphene with nitrogen and another heteroatom (B, S or P) [122], [123]. Other materials containing non-precious metals (Co, Fe, Mn...) supported on carbon have been successfully synthesized to form catalytic active sites. Iron (Fe), in particular, in its oxide, carbide or hydroxide forms, has demonstrated its effect to enhance the ORR activity of the neighboring graphitic carbon [124]–[126].

To further improve the ORR activity, some researchers have studied and demonstrated the use of transition metal into N-doped graphene [127], [128]. Experimentally, the synergistic effect between the N-doped graphene and transition metal results in a much better catalytic activity compared to either N-doped graphene or transition metal only [129].

The aim of this work is to study and compare the electro-catalytic properties of the prepared reduced graphene oxide (RGO) based materials using the oxygen reduction reaction (ORR). We report a facile synthesis, characterization and ORR tests for reduced graphene oxide doped with nitrogen (N-RGO), phosphorus (P-RGO), both nitrogen/phosphorus (PN-RGO) and both iron oxide/nitrogen (Fe_3O_4/N-RGO) composite.

The first chapter contains a brief description of metal-air batteries that involve the oxygen reduction reaction. The mechanism reaction of this latter is presented. A brief review regarding the most efficient catalysts for the oxygen reduction reaction is discussed. This chapter also introduces a literature survey on graphene, as an interesting catalyst for the oxygen reduction reaction and present an original biological synthesis method using different types of bacterial species for RGO production.

The second chapter focuses on the experimental procedure to prepare the reduced graphene oxide based materials for ORR application and also on a biological route to synthesize reduced graphene oxide. The characterization techniques principles and electrochemical measurement methods are addressed.

In the third chapter, we investigate the results of structural and electrochemical characterizations for the prepared materials.

Chapter I: Literature survey

I.1 Metal-air batteries (MABs)

I.1.1 Electrochemical principles of a metal-air battery

Metal-air batteries (MABs) are mostly investigated for their much higher energy densities than lithium-ion batteries and for so many other attractive advantages [130].

This type of batteries generates electricity through a Redox reaction between metal and oxygen in air. They are featured with open cell structure, which admits the supply of the cathode active material - oxygen - continuously and almost infinitely from an external source (air).

Metal-air electrochemical cells are batteries that use a pure metal electrode as anode and air electrode as cathode, typically with a separator soaked in metal-ion conducting electrolyte [131]. During discharging of a metal-air electrochemical cell, metal is oxidized and transformed to metallic ions at the anode. The released electrons circulate through the external circuit. At the same time, oxygen from the surrounding air diffuses into the cathode, accepts the electrons from the anode and is reduced to hydroxide ions, as illustrated in **Figure B.I.1**. When the cell is charged, the process is reversed, with metal plating at the anode and oxygen evolving at the cathode [132].

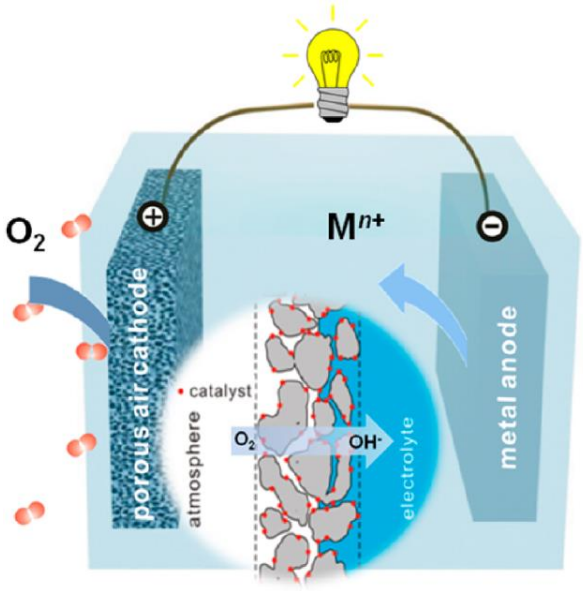

Figure B.I.1. Schematic configuration and working principle of an aqueous metal-air battery. The insert illustrates the oxygen reduction reaction taking place at the porous air cathode [133]

Electrode reactions of rechargeable metal-air batteries vary with the metal electrode and the type of electrolyte used. Generally, for metal-air batteries with aqueous electrolytes the electrode reactions are in the following form [134]:

At the anode: $M \leftrightarrow M^{n+} + ne^-$

At the cathode: $O_2 + 2H_2O + 4e^- \leftrightarrow 4OH^-$

Where M stands for the metal (Zn, Al, Mg, Fe, etc.) and n represents the metal ion charge number.

I.1.2 Different types of metal-air batteries

A series of metals have been used including zinc (Zn), aluminum (Al), magnesium (Mg), iron (Fe), lithium (Li), sodium (Na) and potassium (K) because of their stable oxidized states. The characteristics of several MABs are summarized in **Table B.I.1** [135].

Table B.I.1. Comparison of different types of metal-air batteries [135]

Battery types	Li-air	Na-air	K-air	Mg-air	Al-air	Fe-air	Zn-air
Theoretical voltage (V)	2.96	2.27	2.48	3.09	2.71	1.28	1.65
Practical voltage (V)	~2.6	~2.2	~2.4	~1.6	~1.8	~1.0	~1.2
Theoretical specific energy (Wh kg^{-1})[a]	3458[b]	1106[c]	935[d]	4110[e]	4274[f]	955[g]	1086[h]
Practical energy density (Wh kg^{-1})	400-800	/	/	~700	~500	~80	~500
Electrolyte for batteries	Aprotic	Aprotic	Aprotic	Saline	Saline & Alkaline	Alkaline	Alkaline
Rechargeable	Yes	Yes	Yes	No	No	Yes	Yes

[a] oxygen uptake inclusive; [b] based on Li_2O_2 at the end of discharge in non-aqueous medium; [c] based on NaO_2; [d] based on KO_2; [e] based on $Mg(OH)_2$, electrolyte inclusive; [f] based on $Al(OH)_3$, electrolyte inclusive; [g] based on $Fe(OH)_2$, electrolyte inclusive; [h] based on ZnO.

All the MABs described in **Table B.I.1** have relatively high theoretical specific energy, approximately two to ten times higher than that of LIBs. Among them, the Al-air (4274 Wh/kg), Mg-air (4110 Wh/kg) and Li-air (3458 Wh/kg) batteries have higher theoretical specific energy than other batteries. Research in the field of Na-air, K-air and Fe-air batteries is still in its infancy, while Li-air, Zn-air, Mg-air, and Al-air are the most promising for production scale development in the near future [136].

Most MABs of Li, Na, and K use aprotic electrolytes. Compared to aqueous MAB, nonaqueous metal-air batteries are not yet sufficiently developed and suffer from even more serious challenges. First, suitable electrolytes for nonaqueous metal-air batteries are yet to be identified. This is because the superoxide or peroxide product is oxidative and would cause the decomposition of most common electrolytes used in conventional lithium-ion batteries. Second,

improving battery discharge performance would require the integral optimization of the electrolyte-cathode couple [133].

On the other side, metals such as Li, Mg, Al and Zn can react violently in acidic medium with a great deal of released heat. The resulting severe anode corrosion and complicated thermal management make the acidic electrolyte inappropriate for practical application. In addition, there are few electrocatalytic materials that are stable under the strongly acidic circumstances and the aggressive oxidizing environments at oxygen cathode. Thus, alkaline solutions are commonly used for aqueous electrolyte-based metal–air batteries [131].

I.2 Oxygen reduction reaction (ORR)

Oxygen reduction reaction (ORR) is of major importance to energy-converting systems, in particular in the metal-air batteries (MABs). It has been the subject of extensive investigation over the last century because it allows to determine the performance of MABs, namely their cyclability, energy efficiency and cycle life [137].

I.2.1 ORR mechanism reaction

ORR is a two-part reaction that requires an electron donator and an electron acceptor, which typically occurs at the cathode and anode of metal-air devices. The reactions at the cathode and anode are primarily controlled by the electrolyte solution, which can be alkaline or acidic. In both media, ORR occurs between hydrogen and oxygen to produce electron flow and power.

Oxygen reduction in alkaline aqueous solutions occurs mainly through two different pathways: the direct four-electron transfer pathway from O_2 to hydroxide ions (OH^-) or the two-electron transfer pathway from O_2 to hydrogen peroxide H_2O_2 as an intermediate step, followed by further reduction to form OH^- with another $2e^-$ release. In metal-air batteries, a four-electron transfer pathway is preferred because the reduction is done directly without going through intermediates and results in a high energy efficiency. Besides, the peroxide ion formed during the reduction in the two-electron transfer pathway is corrosive and will cause battery degradation [138].

The reaction pathways of ORR in alkaline aqueous electrolyte and their corresponding thermodynamic electrode potentials Vs SHE at standard conditions are presented below [139]:

Direct four-electron transfer pathway:

$O_2 + H_2O + 4e^- \leftrightarrow 4OH^-$ (E° = 0.401 V)

Two-electron transfer pathway:

$O_2 + H_2O + 2e^- \leftrightarrow HO_2^- + OH^-$ (E° = − 0.065 V)

$HO_2^- + H_2O + 2e^- \leftrightarrow 3OH^-$ (E° = 0.867 V)

It is desirable for the ORR to occur at potentials close to thermodynamic potentials as much as possible. For the thermodynamic potentials to be obtained, the charge transfer kinetics of the ORR must be quick.

I.2.2 ORR catalysts

The kinetics of the ORR at the cathode are very important, as they are the factor for the performance of metal-air batteries. Unfortunately, the ORR kinetics is normally very slow which results in reducing the ORR performance. Therefore, to achieve the large-scale commercialization of metal-air batteries, the ORR kinetics at the cathode must be overcome. For this reason, tremendous efforts have been made to explore efficient oxygen electrocatalysts for the ORR [140].

Even though Pt-based catalyst is considered to be one of the best electrocatalysts for ORR, there are several significant limitations that hinder its widespread utilization, namely its scarcity and high cost. This has led to more research being conducted in an effort to develop stable, inexpensive and non-precious ORR electrocatalysts with an excellent catalytic performance [141]. The alternative electrocatalysts explored included noble metals and alloys, transition metal materials and carbon-based materials.

- **Noble metals**

One promising set of catalysts that have been widely used as cathode materials for ORR are Pt, Pd, Ag, Rh, Ir and Ru. These materials have been recognized as the most active electrocatalyst for ORR, and they remain the benchmark in the evaluation for new electrocatalysts [142]. Among these, Pd, which has the same electron configuration and lattice constant as Pt, as they belong to the same row in the periodic table, showed the most improved ORR towards alcohol in an alkaline medium, while it is reported to be inactive in an acid medium.

Several methods to reduce the cost and enhance the activity of the Pt-based catalysts are continuous exploiting, including decreasing the particle size, reducing the thickness of Pt layers, alloying with transition metals and enhancing the synergistic effect [143].

- **Transition metal oxide**

Among low-cost alternatives to state-of-the-art Pt noble-metal electrocatalysts, transition metal oxides such as Mn, Co, Cu, Ni, Fe oxides have drawn extensive attention due to their abundant reserves, environment friendliness, low cost and excellent catalytic activity, making them more convenient for practical application. Transition metal oxides were proposed among the best ORR catalysts to substitute the noble metal catalysts in alkaline solution. Therefore, they have inspired a new wave of research on the transition-metal-oxides-based catalysts for ORR [144].

Although drawbacks such as poor conductivity and insufficient stability still existed, the relatively high catalytic performance, excellent corrosion resistance in various electrolyte media and outstanding catalytic selectivity still make them potential electrocatalysts for ORR. Numerous efforts have been concentrated on transition metal-based catalysts in the past decade, by adopting methods of nanosizing, heteroatom doping and loading conductive substrate, the catalytic activity, conductivity and the sluggish kinetics of transition metal catalysts have been greatly improved [145].

- **Carbon-based materials**

Carbon materials are a new kind of electrocatalysts that is expected to have extensive applications. They have demonstrated to show multiple advantages, including high electronic conductivities, large surface area, tunable molecular structures, abundance, and strong tolerance to acidic and alkaline environments [146].

This family of materials includes graphite nanoplatelets, carbon nanotubes (CNTs), graphene sheets and three-dimensional (3D) carbon architectures like fullerenes [147]. The sp2-type carbon materials possess high electroconductivity, which are suitable for supports of catalysts. Extensive efforts have so far been devoted to carbon-based ORR catalysts. Recently, carbon materials doped with heteroatoms such as nitrogen, boron, sulfur, etc. have attracted increasing attention as efficient metal-free ORR catalysts. When the carbon materials are doped with heteroatoms, especially by N atom, they can exhibit high catalytic activity for ORR [148].

Transition metal and nitrogen co-doped carbonaceous catalysts (M/N/C, M = transition metal) are a category of non-precious metal catalysts that are recognized as the most promising substitutes for the expensive Pt-based catalysts currently used. M/N/C catalysts have high activity toward the oxygen reduction reaction, are much cheaper than precious metal catalysts, and use abundant rather than scarce resources [149]. Unsurprisingly, they have become one of the most important subjects of research in this area during the past decade. M/N/C catalysts have excellent ORR performance in both acidic and alkaline media and it has been proved by many research works that the metal air batteries MABs with M/N/C catalysts as air cathode exhibited excellent activity and stability. The application of M/N/C catalysts in various kinds of MABs has been widely and intensively explored, including in Li-air batteries, Zn-air batteries, Al-air batteries, and Mg-air batteries. M/N/C catalysts generally exhibit good performance in these types of batteries, comparable to that of precious-metal catalysts [150].

I.3 Graphene as electrocatalyst for oxygen reduction reaction (ORR)

Graphene, the first two-dimensional (2D) atomic crystal, is one of the most recent carbon nanomaterials that have attracted widespread attention because of its fascinating properties and enormous potential for various applications [151].

There is a constant research for highly efficient renewable energy technologies, and it would be surprising if graphene were not involved in this race. The prospect of using graphene in energy harvesting and storage devices such as metal-air batteries is being considered particularly interesting. Therefore, to meet the increasing demand for high-energy density batteries, much effort has been made to explore this material [152].

Studies have showed that graphene and doping graphene with other elements could improve ORR activity up to three times higher than platinum and display greater chemical stability [147].

I.3.1 Structure of graphene

Many two-dimensional (2D) crystalline materials have been identified and analyzed. The first material in this new class is graphene, a nanomaterial consisting of a single atomic layer of carbon [153].

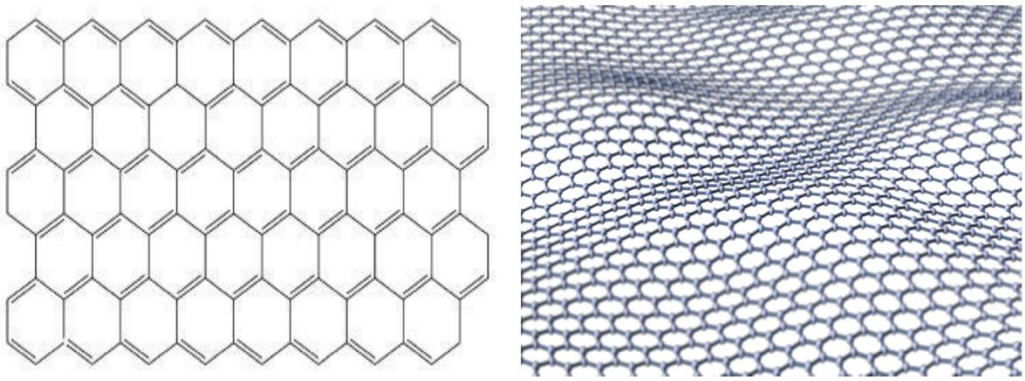

Figure B.I.2. Structure of graphene [154]

It can be considered as a surface consisting of sp2 hybridized carbon atoms arranged in a hexagonal (honeycomb) lattice, with a carbon-carbon distance of 0.142 nm [155]. In graphene planes, each carbon atom has four bonds, three σ bonds with its three nearest neighbors and one π bond that is oriented out of plane, this is what makes graphene a metal conductor [156].

Graphene forms a basic structure of other carbon materials like graphite, carbon nanotubes and fullerenes.

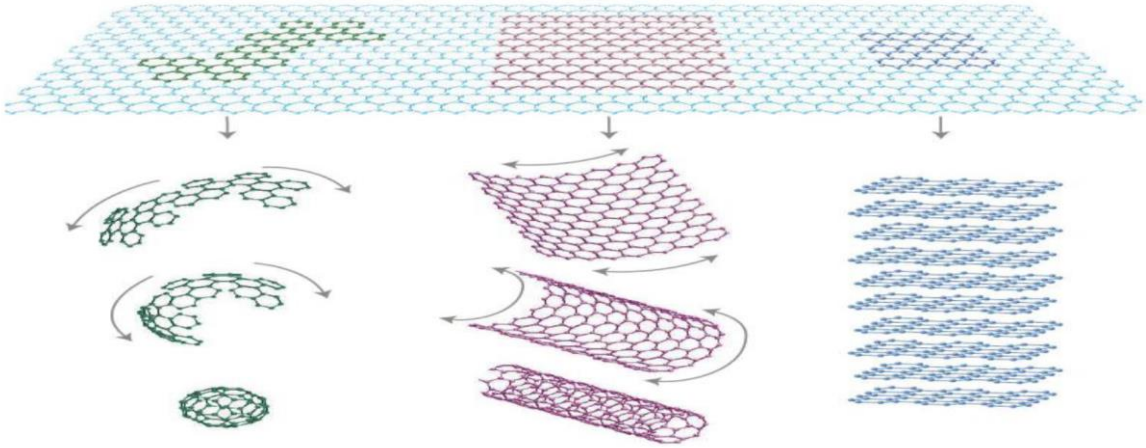

Figure B.I.3. Structure of fullerene C_{60} molecule, carbon nanotube and graphite; can all be thought of as being formed from graphene sheets [157]

For example, graphite (carbon allotrope of 3D) consists of graphene sheets stacked on each other and separated by a distance of 0.34 nm, with a 60° rotation of a plane relative to the other. The fullerene C_{60} (carbon allotrope of 0D) may be considered to be made by wrapping a graphene sheet section. Carbon nanotubes (CNTs) (carbon allotropes of 1D) can be made by

rolling graphene sheets. However, in reality these carbon allotropes are not synthesized from graphene [158].

I.3.2 Properties of graphene

This one-atom-thick material of carbon has revealed various novel properties. It uniquely combines extreme mechanical strength, exceptionally high electronic and thermal conductivities, impermeability to gases, as well as many other supreme properties, all of which make it an exciting material and highly attractive for numerous applications [159].

- Graphene is practically transparent conductor. In the optical region, it absorbs only 2.3% of the light. Thus, suspended graphene does not have any color, and its optical transmittance is ≈ 97.7% [160].

- The electron mobility of graphene depends weakly on temperature, suggesting that an ultrahigh mobility could be realized in graphene at room temperature. By minimizing impurity scattering, mobility in excess of 2×10^5 cm^2 V^{-1} s^{-1} was achieved in suspended graphene, an exceptionally high value [161].

- Graphene has remarkable mechanical properties. It is substantially 100 times stronger than steel and it is very stretchable, with intrinsic strength of 130 GPa, and high Young's modulus ≈ 1.0 TPa [162]. It has a perfect periodic structure, even if the procedures for realization are very basic. The perfect crystalline order seems to derive strong interatomic bonds, which gives a more resistant material than diamond, yet very flexible [163].

- Graphene has a very high electrical conductivity (≈ 6000 S/cm), because electrons can flow without being slowed down by network defects [164].

- The thermal conductivity of graphene has been measured to be approximately 5000 Wm^{-1} K^{-1}, which is ten times than that of copper (401 Wm^{-1} K^{-1}) at room temperature [165].

- Graphene has a large theoretical specific surface area ≈ 2600 m^2/g [166].

These exceptional properties have made graphene one of the most interesting topics of study at the moment, which suggest that graphene could replace other materials in existing applications.

I.3.3 Graphene as electrocatalyst for ORR

Several reports on graphene-based electrocatalysts for ORR are currently being widely studied [167], [168].

Domga et al [169] have reported the synthesis of nitrogen and phosphorus co-doped graphene (NPG) using ammonium dihydrogen phosphate as both nitrogen and phosphorus precursor. The obtained results demonstrated that, the reduction mechanism of oxygen follows nearly four-electron transfer process in O_2 saturated alkaline medium. In addition, this catalyst exhibited higher ORR stability than the commercial Pt/C. The large N and P content in the catalyst with all the active sites have facilitated faster ORR kinetics as well as it stability. Thus, the NPG is a highly economical, promising and sustainable alternative electrocatalytic material.

Liao et al [170] have developed a Cu-containing nitrogen-doped reduced graphene oxide (Cu/N-RGO) composite as a promising electrocatalyst for ORR. By investigating its catalytic performances, it was found that the 3%Cu/N-rGO catalyst could provide superior catalytic activity for ORR being close to that of the traditional Pt-C electrocatalyst and displayed a four-electron pathway. Such outstanding catalytic properties are attributed to the abundant active sites and the synergy between Cu and N in Cu/N-RGO.

I.4 Synthesis of reduced graphene oxide (RGO)

Graphene has been prepared in various ways such as micromechanical exfoliation of graphite [171], epitaxial growth [172], chemical vapor deposition (CVD) [173] and reduction of graphene oxide (GO) [174]. From the aforementioned methods the most suitable for large-scale graphene production is reduction of graphene oxide (GO). This method is based on oxidation of graphite to obtain graphite oxide (GTO), followed by exfoliation into graphene oxide using a treatment of sonication. GO can be regarded as a monolayer or a few stacked layers of graphite oxide. After that, the GO sheets are reduced to remove the oxygen-containing groups on the surface and the edges of graphene oxide to obtain reduced graphene oxide (RGO) [154].

Several methods have been developed to reduce graphene oxide in order to prepare RGO nanosheets in large quantities with high structural quality and high thermal stability. The reduction can be performed thermally, chemically, electrochemically, biologically etc. [158].

I.4.1 Chemical route synthesis

Chemical reduction of graphene oxide has been performed with several reducing agents, such as hydrazine [175], hydroquinone [176], sodium borohydride [177], and ascorbic acid [178]. However, it often needs to introduce excessive reducing agents and brings impurity contamination, also it requires a reaction time of many hours, high temperature, and hazardous hydrazine as a reducing agent. Thus, this technique is not a green approach to the production of reduced graphene oxide [179].

I.4.2 Biological route synthesis

Most of the research has been focused on large-scale production of graphene through the chemical reduction of chemically derived graphene oxide (GO). However, these approaches may cause environmental or economic concerns when large-scale production is considered [180].

In order to overcome the toxicity problem, many efforts have been attempted to explore green, environment-friendly and effective routes to achieve the reduction of GO. These have included methods involving bacterial respiration [181].

The use of living biological systems to produce graphene have been recently investigated. The implementation of such greener, more sustainable alternatives for the synthesis of graphene in large quantities via biological reduction of graphene oxide can thus produce highly stable, conductive, large areas of graphene sheets [182].

Recently, there have been several reports on the microbial reduction of GO to produce graphene. This approach needs the use of bacterial species as reducing agents such as Shewanella cells [183], Azotobacter chroococcum cells [184] and E.coli cells etc. [185]. Such biological paths have shown some promising results for GO reduction.

I.5 Research context

In this thesis work we have chosen to investigate and compare the electro-catalytic activity of the different reduced graphene oxide (RGO) based materials doped with heteroatoms and metals using oxygen reduction reaction (ORR).

We demonstrated that these materials could be a good alternative to the preparation of active, efficient and inexpensive catalysts. In addition, we have studied the bacterial reduction effect on graphene oxide using different types of bacterial species.

The work presented in this thesis is the result of a collaboration between Mohammed Vth University and "Institut National de la Recherche Scientifique (INRS)" Canada. This work is financially supported from Moroccan Ministry of National Education, Vocational Training, Higher Education and Scientific Research-Mohammed Vth University under project PPR (Development of new nanomaterial for electrochemical energy storage: Na-air and Li-ion batteries).

Chapter II: Experimental setup

In this chapter, we report a facile synthesis methods to prepare the graphene oxide (RGO) based materials: reduced graphene oxide doped with nitrogen (N-RGO), doped with phosphorus (P-RGO), doped with both nitrogen and phosphorus (PN-RGO) and doped with both iron oxide and nitrogen (Fe_3O_4/N-RGO) composite.

II.1 Chemical synthesis of reduced graphene oxide based materials

The reduced graphene oxide based materials are synthesized using graphite oxide (GTO) as the starting material. This latter is prepared using the Hummers method as described in part A.

II.1.1 Nitrogen doped reduced graphene oxide (N-RGO) synthesis

Graphite oxide (1 g) was stirred in ethanol (50 mL) for 1 h, and treated with the ultrasound for 30 min. Then, ammonium nitrate NH_4NO_3 (1 g) was added into the suspension as nitrogen precursor. The mixture was stirred and heated at 60 °C to evaporate ethanol. The dried mixture was finely grinded and transferred into a muffle furnace and calcined at 350 °C for 1 h to obtain N-RGO [186].

II.1.2 Phosphorus doped reduced graphene oxide (P-RGO) synthesis

P-RGO was prepared following the same procedure as for N-RGO using Ammonium dihydrogen phosphate $NH_4H_2PO_4$ as phosphorus precursor.

II.1.3 Phosphorus, Nitrogen co-doped reduced graphene oxide (PN-RGO) synthesis

PN-RGO was also synthesized following the same procedure as for N-RGO using Ammonium dihydrogen phosphate $NH_4H_2PO_4$ and ammonium nitrate NH_4NO_3 as phosphorus and nitrogen precursors respectively.

II.1.4 Iron oxide and Nitrogen co-doped reduced graphene oxide (Fe_3O_4/N-RGO) synthesis

Graphite oxide (80 mL) aqueous dispersion with a concentration of 1.5 mg/mL was added to iron (III) acetate $[Fe_3O(CH_3CO_2)_6(H_2O)_3]CH_3CO_2$ (133.3 mg) and firstly treated with the ultrasound for 5 min, then polypyrrole (266.6 mg) was slowly added to form a stable complex solution by sonication for 10 min. Subsequently, the stable suspension was hydrothermally treated at 180 °C for 12 h. After that, the as-prepared sample was freeze-dried

overnight, followed by thermal treatment at 600 °C for 3 h under Argon atmosphere to obtain Fe_3O_4/N-RGO [187].

II.2 ORR electrochemical measurements

II.2.1 Catalyst ink preparation

The as-prepared reduced graphene oxide based catalysts (10 mg) were mixed with Nafion (95 µL) which serves as a binder and ethanol (350 µL). The mixture was mixed using vortex mixer and sonicated for 1 h. Then, 9 µl of this ink were taken and deposited on the surface of the glassy carbon electrode, dried at room temperature and used as a working electrode for all the electrochemical tests.

II.2.2 Electrochemistry testing

Electrochemical measurements were performed on a computer-controlled Pine (AFRDE4) potentiostat with a three-electrode electrochemical cell. A platinum wire, saturated calomel electrode (SCE) and rotating ring disk electrode (RRDE) with a collection efficiency of 0.37, were used as counter electrode, reference electrode and working electrode respectively. All of the experiments were conducted at room temperature using O_2 and N_2 saturated 0.1 M KOH alkaline electrolyte.

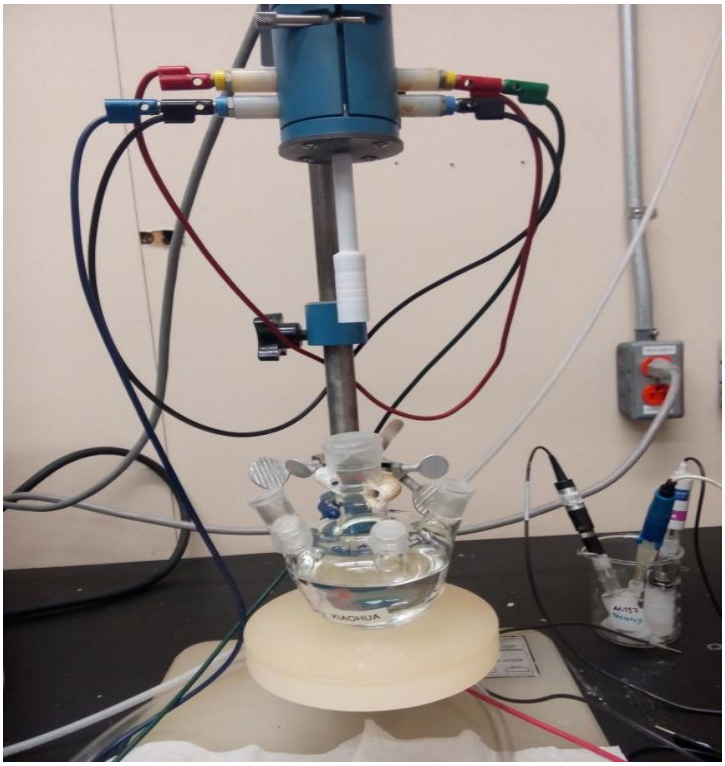

Figure B.II.1. A photograph of an electrochemical cell with three electrodes

The catalytic activity of the samples was evaluated by cyclic voltammetry (CV) and linear sweep voltammetry (LSV) techniques. The potential range was scanned between −1 V and 0.2 V Vs SCE at a scan rate of 50 mV/s for CV and 10 mV/s for LSV. The rotating speed of the working electrode for the LSV was 1600 rpm.

The potential shown in the results was converted to reversible hydrogen electrode (RHE).

II.3 Biological synthesis of reduced graphene oxide based materials

In this study, the bacterial reduction of graphene oxide is investigated using two protocols. The first one consists of testing different bacterial strains and study their reduction effect on graphene oxide (GO). The second protocol is to test the strain that delivered the highest reduction rate of graphene oxide (GO) and to investigate its reduction effect using different samples in order to study the bacterial reduction ability and to confirm the obtained results in the first protocol.

II.3.1 The first protocol

In this test, the bacterial reduction of graphene oxide is tested using fourteen different strains of extremophilic/thermophilic bacteria originated from the desert of Morocco with

references 253, 306, 155, 2, 30, 79, 339, 85, 24, 45, 46, 61, 76 and 177 and two different concentrations of graphene oxide 0.5 mg/ml and 1 mg/ml. The protocol was realized through the following steps.

II.3.1.1 Preparation of bacterial biomass

First, we prepare the Luria Broth (LB) culture medium that is designed to support the growth of bacteria. It is a medium that must provide a source of energy and elements such as carbon, nitrogen, sulfur, phosphorus and growth factors. It is prepared exclusively with pure chemicals by mixing tryptone (10 g), sodium chloride (10 g), yeast extract (5 g) and distilled water (1 L). After mixing the reagents, the medium is buffered with hydrochloric acid (HCl) and sodium hydroxide (NaOH). The pH of the medium is measured, then it is adjusted using HCl and NaOH until a fixed neutral pH of 7 is obtained. Finally, the culture medium is sterilized in an autoclave at 120 °C overnight.

Each of the fourteen bacterial strains were cultured in the medium and incubated on a rotary shaker at 37 °C and 180 rpm for one day.

In order to compare the bacterial reduction effect, all the strains used must have the same optical density (OD) that is the growth state of a bacterial culture. This will help ensure that cells are harvested at an optimum point that corresponds to an appropriate density of live cells.

First, we measure the initial optical density for each strain using an UV-Visible spectrophotometer (OD_i). Then, to have a final optical density (OD_f) of 0.7 for all strains, we calculate the volume of the bacterial culture (V_b) needed for each strain for a final volume (V_f) of 20 ml, using the following equation:

$$OD_i \,.\, V_b = OD_f \,.\, V_f \quad \rightarrow \quad V_b = (OD_f \,.V_f)/OD_i$$

The OD of 0.7 corresponds to 7.108 Colony Forming Units per milliliter (CFU/mL); that is the number of viable bacteria in a sample, which has the ability to multiply via binary fission under the controlled conditions.

Therefore, for each bacterial culture the calculated volume (V_b) was pipetted and then the biomass of the bacteria was recovered by centrifugation (5000 rpm, 20 min). Afterwards, the biomass was washed twice with sterile water to remove traces of the culture medium.

II.3.1.2 Reduction of graphene oxide (GO)

Suspensions of graphene oxide (GO) (10 ml) with two different concentrations (0.5 and 1 mg/ml) are prepared using graphite oxide (GTO). This latter is mixed with distilled water and treated with the ultrasound for 1 h. Then, the GO suspensions are added to each of the prepared bacterial biomass and incubated on a rotary shaker at 37 °C and 180 rpm for 5 days.

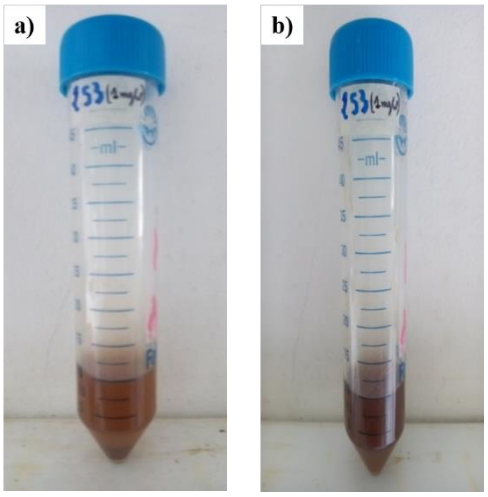

Figure B.II.2. A photograph of a GO suspension (1 mg/ml) mixed with bacterial biomass (253 strain) before **a.** and after **b.** incubation

II.3.1.3 Lysis of bacteria

To separate bacteria from reduced graphene oxide, the thermal shock method for the lysis of the bacteria by its bursting are tested. The bacteria disintegrates and its density decreases. Subsequently, after centrifugation, the graphene precipitates downwards and the bacteria remains in the supernatant.

The mixture reduced graphene oxide-bacteria is frozen at −20 °C for 2 h and is then thawed using a water bath at 100 °C for 15 min. Next, the mixture is centrifuged at 2000 rpm for 15 min. However, good separation of bacteria from reduced graphene oxide could not be obtained and bacteria were precipitated down with RGO.

Therefore, a sucrose solution is used to separate bacteria from reduced graphene oxide, since a density value of 1.6 g/ml is obtained for the sucrose solution. This value is between 2.2 g/ml of graphene density and ≈ 1 g/ml of bacteria density, thus allowed a better separation.

II.3.1.4 Separation of bacteria from reduced graphene oxide by sucrose solution

A 20% sucrose solution is prepared, sterilized in an autoclave at 120 °C overnight and poured into the centrifuge tubes (35 ml). 10 ml of reduced graphene oxide-bacteria mixture is then pipetted and slowly added to the solution in order to remain at the surface of the tube without mixing. The tubes are next centrifuged at 5000 rpm for 30 min.

After centrifugation, three different colored zones are noticed: at the bottom reduced graphene oxide precipitate, in the middle sucrose solution and above a brown supernatant that contains bacterial debris. Finally, the obtained reduced graphene oxide precipitate is washed with ultrapure water for three times.

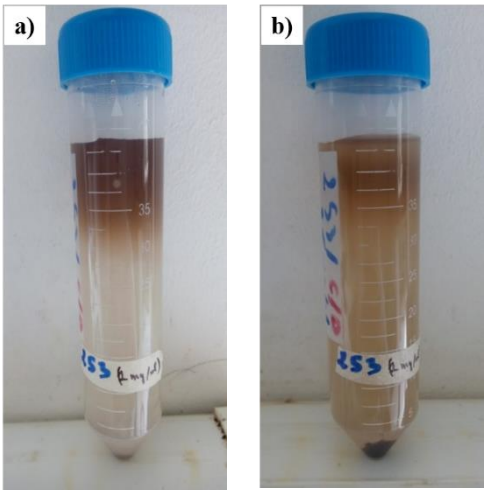

Figure B.II.3. A photograph of the tube before **a.** and after **b.** centrifugation

II.3.1.5 Calculate the percentage of reduced graphene oxide

In order to know the percentage of graphene oxide remaining and the percentage of reduced graphene oxide formed after the reduction, the optical density OD of graphene oxide is measured using the UV-Visible spectrophotometer at 230 nm (the wavelength corresponding to the maximum absorbance of graphene oxide).

The curve of the optical density (OD) is plotted as a function of GO concentrations: The Beer-Lambert law [188].

Table B.II.1. Measurement of the optical density (OD) of graphene oxide as a function of its different concentrations

C (mg/mL)	0.02	0.035	0.05	0.07	0.09	0.1	0.15
OD	0.6028	0.9556	1.3251	1.7462	2.2308	2.3889	3.2960

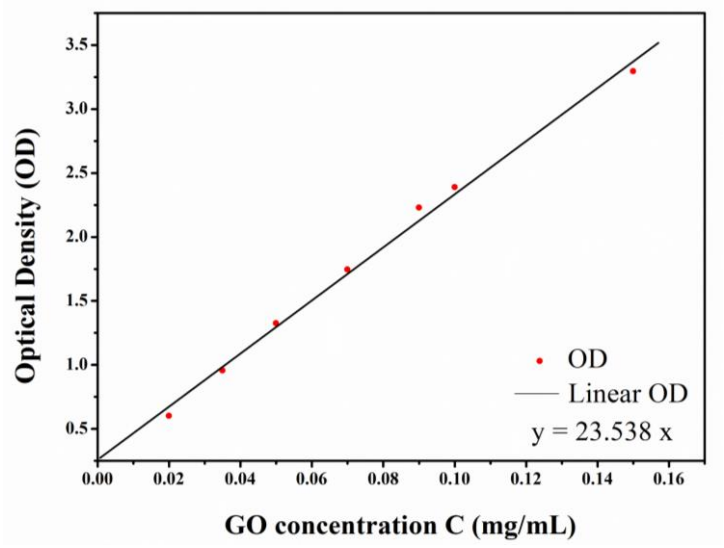

Figure B.II.4. Optical density (OD) curve as a function of GO concentrations

The concentration of graphene oxide remaining [GO remaining] corresponding to the OD measured after reduction is obtained from the curve in **Figure B.II.4**.

Finally, the concentration of reduced graphene oxide formed [RGO formed] is calculated by the difference with graphene oxide remaining [GO remaining].

$$[\text{GO initial}] \rightarrow 100\%\ \text{GO}$$

$$[\text{GO remaining}] \rightarrow \%\text{GO remaining}$$

$$\%\text{GO remaining} = [\text{GO remaining}] / [\text{GO initial}] \times 100\%$$

$$\%\text{RGO} = 100\% - \%\text{GO remaining}$$

II.3.2 The second protocol

In order to be sure that the color change of GO during reduction is due to the bacteria and not to the temperature or other parameters, a second test is realized with only 253 bacterial strain, which delivered the highest percentage of reduced graphene oxide in comparison with other strains, and using different samples.

The bacterial culture and graphene oxide (GO) suspensions 0.5 and 1 mg/ml are prepared through the same procedure as the 1st test.

In this test, the following five prepared samples are:

- Graphene oxide (GO) suspension, the control sample: GO control.
- Graphene oxide (GO) suspension mixed with the bacterial biomass: GO + 253 biomass.
- Graphene oxide (GO) suspension mixed with the bacterial culture (bacteria biomass in the presence of its culture medium LB): GO + 253 biomass + LB.
- Graphene oxide (GO) suspension mixed with only the culture medium sterilized (without bacteria): GO + LB sterilized.
- Graphene oxide (GO) suspension mixed with only the culture medium after bacterial growth (without bacteria): GO + LB after growth.

Each of the samples is incubated on a rotary shaker at 37 °C and 180 rpm for 5 days, same as the 1st test. Next, only the samples that contain bacteria (GO + 253 biomass and GO + 253 biomass + LB) are frozen at −20 °C for 2 h and is then thawed using a water bath at 100 °C for 15 min for bacteria lysis. After that, the 20% sucrose solution is used to separate between reduced graphene oxide and the bacteria, as showed in the 1st test.

Finally, all the five samples are washed with ultrapure water for three times.

The optical density OD of the samples after the reduction are measured and then the percentages of reduced graphene oxide are calculated using the Beer Lambert law.

Chapter III: Results and discussions

III.1 Characterizations of reduced graphene oxide based materials synthesized by chemical route

III.1.1 Structural and morphological characterizations of reduced graphene oxide based materials

III.1.1.1 X-Ray Diffraction (XRD)

The structure of the prepared reduced graphene oxide based materials is analyzed by XRD. As shown in **Figure B.III.1**, GO exhibits a strong peak (002) at 2θ = 10° typical of graphene oxide corresponding to an interlayer distance of 0.88 nm, which is due to the presence of various oxygen-functional groups and water molecules originated from the oxidation process of graphite [189].

N-RGO pattern shows a new broad peak (002) at 2θ = 25.56° with a decrease of the interlayer spacing to 0.34 nm. This result shows that the reduction of GO is completed [190], and that most of the functional groups were removed after doping with nitrogen.

Same for P-RGO, the characteristic peak of GO is replaced by a broader and weaker peak (002) at 2θ = 24.3° with an interlayer spacing of 0.36 nm, higher than that of N-RGO, suggesting that the phosphorus creates higher disorder than nitrogen [191].

Concerning the PN-RGO pattern, the peak is located at the same position as for P-RGO 2θ = 24.3°.

For Fe_3O_4/N-RGO XRD pattern, both Fe_3O_4 (JCPDS No. 65-3107) [192] and reduced graphene oxide peaks are observed showing the probable high amount of graphene. It is interesting to observe that the diffraction hump of graphene appears at 2θ = 25.5° as for N-RGO, confirming a composite formation.

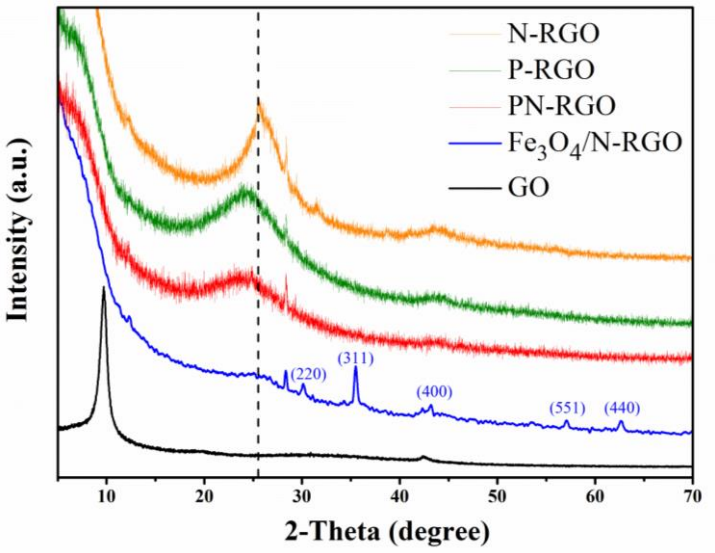

Figure B.III.1. XRD patterns of the prepared reduced graphene oxide based materials

III.1.1.2 ThermoGravimetric Analysis (TGA)

To determine the amount of Fe_3O_4 in the composite, ThermoGravimetric Analysis (TGA) and Differential Scanning Calorimetry (DSC) of Fe_3O_4/N-RGO composite were realized (**Figure B.III.2**). Two kinds of weight loss are observed. The first one of 5.30% (wt.%) from 25 °C to 300 °C is corresponding to the liberation of the chemically and physically adsorbed water molecules in the sample surface.

The second weight loss of 82% (wt.%) is accompanied with two exothermic peaks which are attributed to the combustion of graphene and nitrogen. This result suggests that the amount of Fe_3O_4 in the composite is only 9% (wt.%).

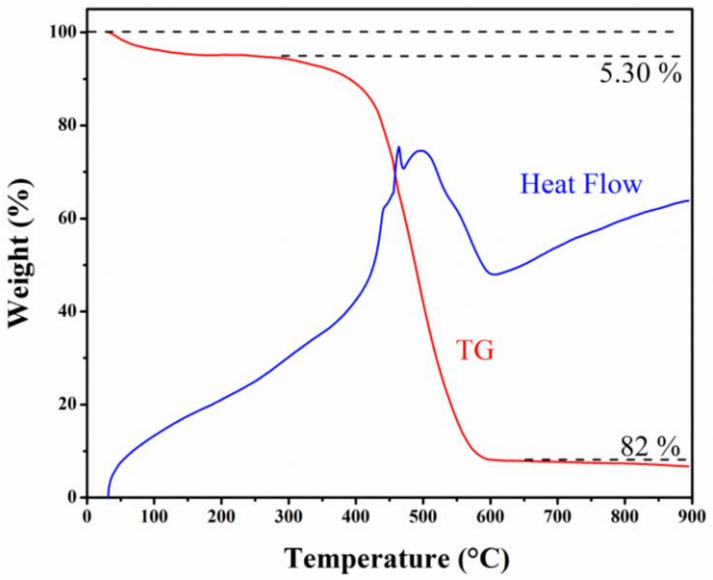

Figure B.III.2. TGA and DSC curves of Fe_3O_4/N-RGO composite oxidation in air with a heating rate of 10 °C/min

III.1.1.3 Fourier Transform Infrared Spectroscopy (FTIR)

To show the reduction of graphene oxide and the doping by nitrogen, a comparison between FTIR spectra of GO and N-RGO is investigated in **Figure B.III.3**. GO sample exhibits a broad band centered at ≈ 3304 cm^{-1}, assigned to the stretching vibration of hydroxyl group (-OH), an intense band at approximately 1731 cm^{-1} assigned to (C=O) stretching of carbonyl and/or carboxyl groups (COOH) situated at the edges and defects of graphene oxide, a peak at 1628 cm^{-1} corresponding to the sp2-hybridized carbon (C=C) skeletal vibration of unoxidized graphitic domain and (O-H) bending and a band at ≈ 1360 cm^{-1} attributed to the (C-OH) stretching. In addition, the bands at 1230 cm^{-1} and 1068 cm^{-1} can be attributed to (C-O-C) stretching and to (C-O) vibration of epoxy groups, respectively [193].

For N-RGO, it can be seen that most of the oxygen groups are removed from the surface of reduced graphene oxide (RGO). However a weak peak at 1731 cm^{-1} is observed, which is due to the residual C=O groups remaining after the reduction. Two other peaks at 1562 cm^{-1} and 1137 cm^{-1} are observed. The first one corresponding to C=C vibrations which has been shifted from 1628 cm^{-1} to 1562 cm^{-1} resulting from the superposition of the vibrations of C=C and C=N. This confirms the incorporation of nitrogen into the structure. The second peak is assigned to the stretching vibration of C-N [194], [195] .

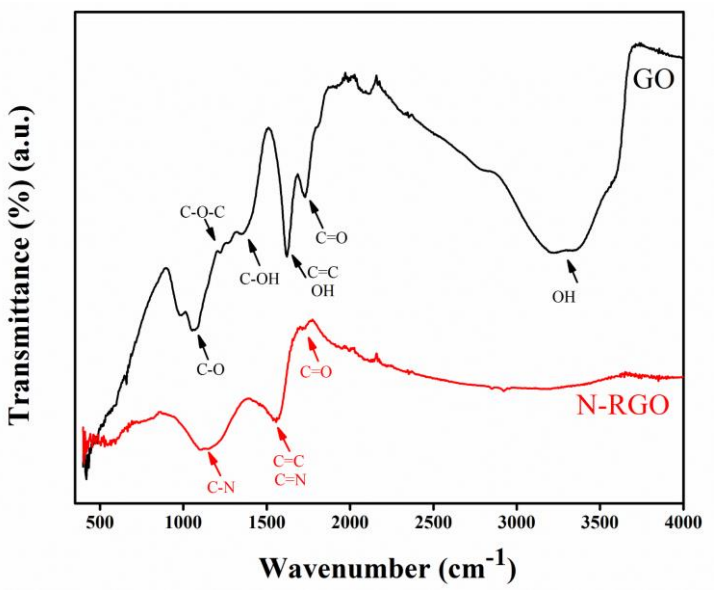

Figure B.III.3. FTIR spectra of GO and N-RGO

III.1.2 Electrocatalytic activity of the reduced graphene oxide based materials

III.1.2.1 Cyclic Voltammetry (CV)

To investigate the electrocatalytic activity of the prepared reduced graphene oxide based materials for ORR, cyclic voltammetry (CV) in a nitrogen N_2-saturated or oxygen O_2-saturated aqueous solution of 0.1 M KOH was carried out.

As can be seen in **Figure B.III.4**, a cathodic peak appears in the CV for all samples in the presence of oxygen, whereas no noticeable response was observed under nitrogen, which demonstrates pronounced electrocatalytic activity for ORR. Furthermore, it can also be seen that for nitrogen doped reduced graphene oxide N-RGO, the CV curves are much broader and larger compared to the other electrodes, which means that the material has a very high surface area caused by the defects sites created from doping with nitrogen.

The Fe_3O_4/N-RGO electrode outperformed the other reduced graphene oxide based materials. As can be seen, the cathodic peak is well defined compared to the other samples.

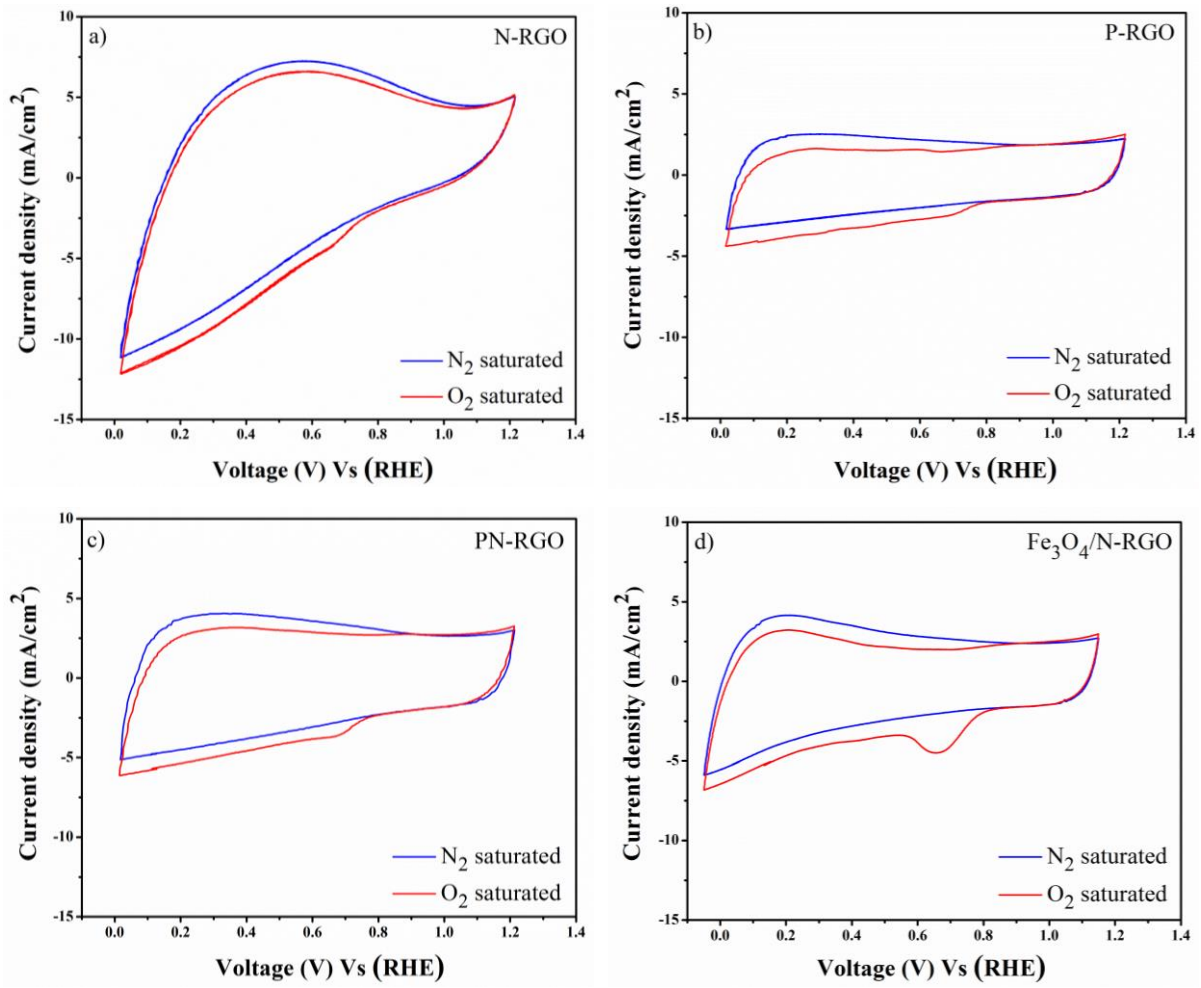

Figure B.III.4. Typical cyclic voltammograms for the ORR at the **a.** N-RGO, **b.** P-RGO, **c.** PN-RGO and **d.** Fe_3O_4/N-RGO electrodes in an aqueous solution of 0.1 M KOH saturated by nitrogen or oxygen gas. Scan rate: 50 mV/s

III.1.2.2 Linear sweep voltammetry (LSV)

To better understand the electrocatalytic performance of these samples during the ORR process, linear sweep voltammograms (LSVs) on a rotating ring disk electrode (RRDE) are recorded at a rotation rate of 1600 rpm in a solution of O_2-saturated 0.1 M KOH and a scan rate of 10 mV/s (**Figure B.III.5**). For all electrodes, the LSV curves show a single-step wide platform, indicating a four-electron ORR process.

The onset potential of Fe_3O_4/N-RGO electrode for the ORR is more positive than those of other samples. Furthermore, the current density reaction of this electrode is also much higher than those of the N-RGO, P-RGO and PN-RGO electrodes, which reached −5 mA/cm^2. This value is also higher than that reported in the study of Wu et al. [187] which has reached only

−4.5 mA/cm^2 at the same rotating speed 1600 rpm. This result is probably due to the amount of graphene in our composite, which is higher than that of the one used by Wu et al. [187] and confirmed by XRD and TGA analyses.

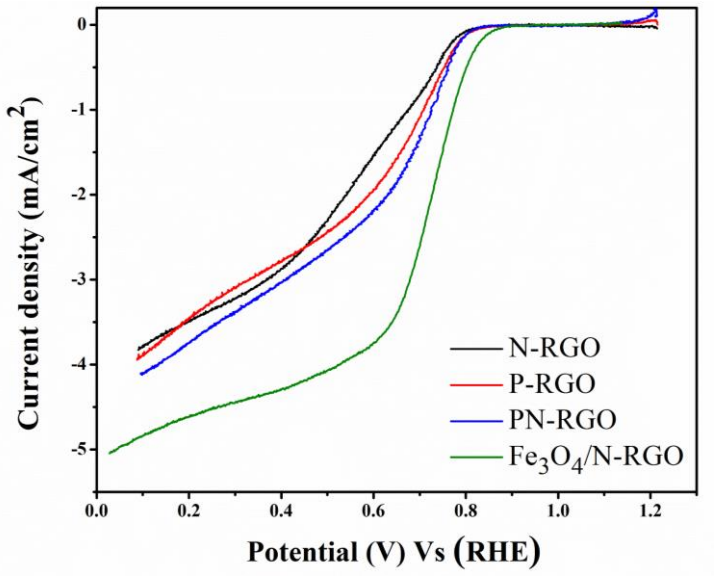

Figure B.III.5. Linear-sweep voltammograms of all samples: N-RGO, P-RGO, PN-RGO and Fe_3O_4/N-RGO electrodes at a rotation rate of 1600 rpm with a scan rate of 10 mV/s

Figure B.III.6 shows the hydrogen peroxide (H_2O_2) percentage formed during the oxygen reduction reaction. It is clearly visible that the Fe_3O_4/N-RGO electrode shows the lowest percentage of H_2O_2 than the other samples (lower than 10%), which confirms the interesting catalytic activity of this material.

The electron transfer number (n) calculated is about ≈ 3.8, indicating a four-electron process toward ORR on the Fe_3O_4/N-RGO electrode. This value is much higher than the other prepared reduced graphene oxide based electrodes.

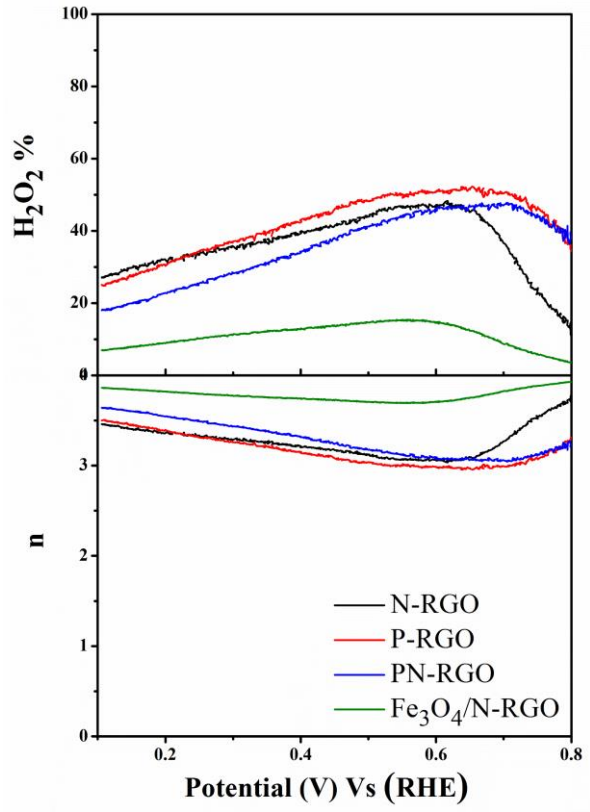

Figure B.III.6. Electron transfer numbers (n) and hydrogen peroxide H_2O_2 yields of the prepared samples obtained from the RRDE data

III.2 Reduction results of reduced graphene oxide using bacteria

III.2.1 The first protocol

Fourteen extremophilic/thermophilic bacterial strains are tested to investigate their reduction effect of graphene oxide (GO) suspensions.

After the reduction, the color of the GO suspensions changed from brown to dark brown for all strains, which proves that graphene oxide is partially reduced to graphene.

The reduction percentages are calculated using the optical density (OD) measurements before and after testing for each strain of bacteria and each GO concentration.

Table B.III.1. Percentages of the reduced graphene oxide obtained for different strains

Bacterial strain	%RGO	
	0.5 mg/mL	**1 mg/mL**
253	94.4%	97.7%
306	95.6%	96.2%
2	92%	97.3%
155	98.2%	93.8%
30	93.4%	96.4%
79	92.8%	95%
339	89.2%	94.7%
85	91.6%	96.3%
24	86.8%	87.5%
45	93.2%	92.4%
46	92.6%	91.6%
61	86.8%	87.1%
76	87.2%	90.6%
177	83.8%	85.8%

Almost all strains showed a satisfactory reducing effect with reduced graphene oxide percentage varying between 83% and 98%. The highest percentage of graphene formed is obtained using the 155 strain for 0.5 mg/ml of GO (98.2%) and 253 strain for the 1 mg/ml of GO (97.7%).

III.2.2 The second protocol

The test of bacterial reduction effect of graphene oxide is repeated to ensure the obtained results in the 1st test, using only the 253 strain and two concentrations of GO (0.5 and 1 mg/ml). Different samples are tested: GO control, GO + 253 biomass, GO + 253 biomass + LB, GO + LB sterilized and GO + LB after growth.

The color of samples GO + 253 biomass, GO + 253 biomass + LB, GO + LB sterilized and GO + LB after growth became darker after reduction compared to graphene oxide alone (GO control), which indicates the partial reduction of graphene oxide to reduced graphene oxide. These results prove that the reduction was achieved by bacteria and not because of temperature.

The samples containing graphene oxide with the culture medium sterilized and after bacterial growth changed color too. This can possibly mean that the culture medium is also a reducer of graphene oxide.

The reduction percentage are calculated using the OD measurements before and after testing for each sample.

Table B.III.2. Percentages of reduced graphene oxide obtained for different samples

Bacterial strain 253	**%RGO**	
	0.5 mg/mL	**1 mg/mL**
GO + LB sterilized	82.24%	88.66%
GO + LB after growth	79.56%	78.76%
GO + 253 biomass	94.84%	94.69%
GO + 253 biomass + LB	57.52%	85.32%

From the obtained results, one can conclude that the culture medium is also a reducing agent of graphene oxide with percentages that are close to those of reduced graphene oxide obtained by bacteria.

The highest percentage of RGO formed is obtained in the GO + 253 biomass sample (94%). Although the color did not change much, the bacteria reduced the majority of GO compared to other samples containing the culture medium.

III.2.3 X-Ray Diffraction (XRD)

The GO + 253 biomass, GO + 253 biomass + LB and GO control samples were characterized using X-Ray diffraction (XRD). In **Figure B.III.7**, we can note the presence of the bump at ≈ 25° significant of the formation of graphene, which shows that graphene oxide has been reduced to graphene for both spectra GO + 253 biomass and GO + 253 biomass + LB.

We also note that the peak at 10° (characteristic of graphene oxide GO) is still present for the three spectrum, which shows that graphene oxide has not been reduced in the GO control sample and that it has not been fully reduced in the GO + 253 biomass and GO + 253 biomass + LB samples. However, this peak in the GO + 253 biomass spectrum is less intense in comparison with the one in the GO + 253 biomass + LB spectrum. These results

demonstrate that the sample that delivered the highest amount of reduced graphene oxide is the GO + 253 biomass.

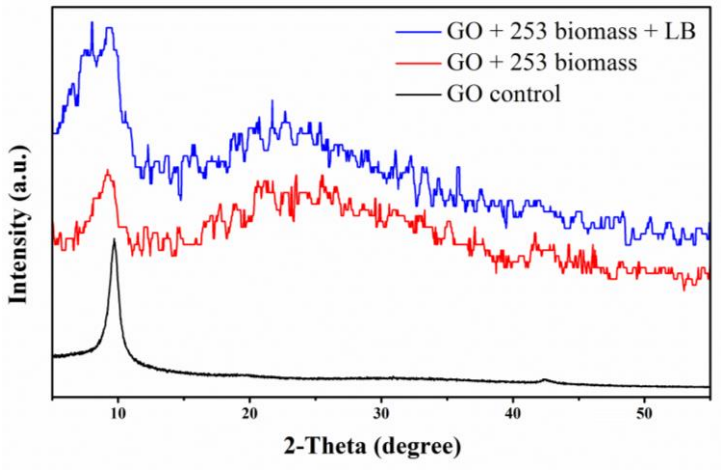

Figure B.III.7. XRD patterns of the prepared GO + 253 biomass, GO + 253 biomass + LB and GO control samples

Conclusion

In this study, doping reduced graphene oxide with nitrogen (N-RGO), phosphorus (P-RGO), both nitrogen/phosphorus (PN-RGO) and a Fe_3O_4/N-RGO composite are successfully synthesized by chemical route and tested as electrocatalysts for oxygen reduction reaction. XRD patterns showed complete reduction of GO after doping and formation of Fe_3O_4/N-RGO composite with considerable amount of N-RGO. This last result has been confirmed by TGA and DSC analyses.

The FTIR results demonstrated the reduction of graphene oxide and the doping by nitrogen in the N-RGO sample by the removal of most oxygen groups the surface of reduced graphene oxide (RGO) and confirmed the incorporation of nitrogen into the structure.

Electrochemical tests have shown that Fe_3O_4/N-RGO composite has the best catalytic activity for ORR in alkaline solution compared to N-RGO, P-RGO and PN-RGO catalysts. This behavior is even better than the one reported in the literature in terms of current density. Also, it exhibits a lower hydrogen peroxide (H_2O_2) percentage and a higher electron transfer number which favors the four-electron pathway to reduce oxygen molecules. Fe_3O_4/N-RGO composite can therefore be an efficient and non-expensive ORR catalyst for metal air batteries.

To conclude, the perspectives in relation to the different materials studied during this work should be considered. It will be more instructive to test other characterization techniques such as scanning electron microscopy (SEM) or X-Ray photoelectron spectrometry (XPS) to confirm the doping of heteroatoms as well as their morphologies and concentration within the graphene matrix. Furthermore, testing of other elements for GO doping such as boron, sulfur, etc, and other metals to study their catalytic effect and compare with the prepared reduced graphene oxide based materials.

The bacterial reduction effect on graphene oxide has been tested in this study using different strains of bacteria and different samples. The obtained XRD results and the measurement of the optical density before and after reduction confirmed that bacteria can partially reduce graphene oxide up to 98.2%.

The first protocol demonstrated that almost all strains has showed a satisfactory reducing effect, with the 253 strain that delivered the highest yield of reduced graphene oxide formation.

The second protocol has showed that the culture medium can also reduce graphene oxide. However, the highest percentage of RGO formed is obtained for the sample containing graphene oxide with the bacteria alone. These results prove that the bacteria have reduced the majority of graphene oxide in comparison with the other samples containing the culture medium.

The originality of this study was to realize other tests by increasing the bacterial concentration to have a higher reduction rate. Also, it will be interesting, after reduction process, drying the RGO in the presence of the bacteria without separation which can possibility deliver graphene doping with the components of the bacteria (N, P, etc.). In addition, prepare a large quantity of graphene reduced by bacteria to perform other characterizations.

General conclusion

During this thesis work, we were interested in different materials likely to be used as negative electrode in lithium-ion batteries, and as electrocatalysts for the oxygen reduction reaction in metal-air batteries. Tin phosphite $SnHPO_3$ based materials as anode for LIBs and reduced graphene oxide based materials as electrocatalysts for ORR.

Electrochemical results obtained showed that CMC binder has allowed a better behavior of $SnHPO_3$ as anode material in comparison with PVDF binder. Thanks to its chemical formula, CMC further improves the electric conductivity, mechanical strength and thus, the cycle performance of the battery. The obtained results for $SnHPO_3$/RGO composites proved that reduced graphene oxide plays an important role in enhancing the electrochemical performance of tin phosphite electrode. The good cycling stability and the high discharge capacity of this electrode make our material a potential candidate as an anode for Li-ion batteries.

Electrochemical tests have shown that Fe_3O_4/N-RGO composite has the best catalytic activity for ORR in alkaline solution compared to the other prepared samples. It exhibits a lower hydrogen peroxide (H_2O_2) percentage and a higher electron transfer number which favors the four-electron pathway to reduce oxygen molecules. Fe_3O_4/N-RGO composite can therefore be an efficient and non-expensive ORR catalyst for metal air batteries.

The obtained results for bacterial reduction effect on graphene oxide confirmed that bacteria can partially reduce graphene oxide up to 98.2%.

List of references

[1] X. Li *et al.*, "Review on comprehending and enhancing the initial Coulombic efficiency of anode materials in lithium-ion/sodium-ion batteries," *Nano Energy*, vol. 77, p. 105143, 2020.

[2] N. P. Shetti, S. Dias, and K. R. Reddy, "Nanostructured organic and inorganic materials for Li-ion batteries: A review," *Mater. Sci. Semicond. Process.*, vol. 104, no. February, p. 104684, 2019.

[3] C. Sun, X. Zhang, C. Li, K. Wang, X. Sun, and Y. Ma, "Recent advances in prelithiation materials and approaches for lithium-ion batteries and capacitors," *Energy Storage Mater.*, vol. 32, pp. 497–516, 2020.

[4] G. Zubi, R. Dufo-lópez, M. Carvalho, and G. Pasaoglu, "The lithium-ion battery : State of the art and future perspectives," *Renew. Sustain. Energy Rev.*, vol. 89, no. March, pp. 292–308, 2018.

[5] J. M. Tarascon and M. Armand, "Issues and challenges facing rechargeable lithium batteries," *Nature*, vol. 414, no. 6861. pp. 359–367, 15-Nov-2001.

[6] L. Jabbour, R. Bongiovanni, D. Chaussy, C. Gerbaldi, and D. Beneventi, "Cellulose-based Li-ion batteries: A review," *Cellulose*, vol. 20, no. 4, pp. 1523–1545, 2013.

[7] D. Cao, X. Sun, Q. Li, A. Natan, P. Xiang, and H. Zhu, "Lithium Dendrite in All-Solid-State Batteries: Growth Mechanisms, Suppression Strategies, and Characterizations," *Matter*, vol. 3, no. 1, pp. 57–94, 2020.

[8] A. Eftekhari, "Lithium-Ion Batteries with High Rate Capabilities," *ACS Sustain. Chem. Eng.*, vol. 5, no. 4, pp. 2799–2816, 2017.

[9] B. Huang, Z. Pan, X. Su, and L. An, "Recycling of lithium-ion batteries: Recent advances and perspectives," *J. Power Sources*, vol. 399, no. July, pp. 274–286, 2018.

[10] Y. Xia, S. Han, Y. Zhu, Y. Liang, and M. Gu, "Stable cycling of mesoporous Sn4P3/SnO2@C nanosphere anode with high initial coulombic efficiency for Li-ion batteries," *Energy Storage Mater.*, vol. 18, pp. 125–132, 2019.

[11] X. Liang *et al.*, "Fabrication of uniform Si-incorporated SnO 2 nanoparticles on graphene sheets as advanced anode for Li-ion batteries," *Appl. Surf. Sci.*, vol. 476, no. September 2018, pp. 28–35, 2019.

[12] Y. Li, Q. Li, H. Wang, L. Zhang, D. P. Wilkinson, and J. Zhang, "Recent progresses in oxygen reduction reaction electrocatalysts for electrochemical energy applications," *Electrochem. Energy Rev.*, vol. 2, no. 4, pp. 518–538, 2019.

[13] J. Wu, "Nanostructured non-precious oxygen reduction reaction catalysts for electrochemical energy applications," University of Waterloo, Ontario, Canada, 2015.

[14] G. J. Cordova, "Mechanism of oxygen reduction reaction on transition metal oxide catalysts for high temperature fuel cells," Massachusetts Institute of Technology, 2008.

[15] K. Oishi, "Oxygen reduction reaction on palladium-cobalt alloy catalysts for polymer electrolyte fuel cells," Université de Montréal, 2012.

[16] Z. Sofer, O. Jankovsky, P. Simek, K. Klimova, A. Mackova, and M. Pumera, "Uranium- and thorium-doped graphene for efficient oxygen and hydrogen peroxide reduction," *Am. Chem. Soc.*, vol. 8, no. 7, pp. 7106–7114, 2014.

[17] Y. Sha, "The mechanisms of the fuel cell oxygen reduction reaction on Pt and other 8-11 column metal surfaces," California Institute of Technology, Pasadena, California, 2011.

[18] J. Zhang, Z. Zhao, Z. Xia, and L. Dai, "A metal-free bifunctional electrocatalyst for oxygen reduction and oxygen evolution reactions," *Nat. Nanotechnol.*, vol. 10, no. 5, pp. 444–452, 2015.

[19] M. Stanley Whittingham, "Electrical Energy Storage and Intercalation Chemistry," *Science (80-.).*, vol. 192, pp. 1126–1127, 1976.

[20] J. O. Besenhard, "The electrochemical preparation and properties of ionic alkali metal- and NR4-graphite intercalation compounds in organic electrolytes," *Carbon N. Y.*, vol. 14, no. 2, pp. 111–115, 1976.

[21] S. Basu, C. Zeller, P. J. Flanders, C. D. Fuerst, W. D. Johnson, and J. E. Fischer, "Synthesis and properties of lithium-graphite intercalation compounds," *Mater. Sci.*

Eng., vol. 38, no. 3, pp. 275–283, 1979.

[22] R. Yazami and P. Touzain, "A reversible graphite-lithium negative electrode for electrochemical generators," *J. Power Sources*, vol. 9, no. 3, pp. 365–371, 1983.

[23] A. Yoshino, "The birth of the lithium-ion battery," *Angew. Chemie - Int. Ed.*, vol. 51, no. 24, pp. 5798–5800, 2012.

[24] V. Pavitra, U. R. Harini, and R. V. B. M. Praveen, "Sonochemical synthesis of - SnO 2 – CuO nanocomposite : diverse applications on Li - ion battery , electrochemical sensing and photocatalytic activity," *J. Mater. Sci. Mater. Electron.*, no. 0123456789, 2020.

[25] Y. K. Lee, D. B. Mahadik, T. Kim, W. Han, H. H. Cho, and H. H. Park, "Effect of differentiated textural properties of tin oxide aerogels on anode performance in lithium-ion batteries," *J. Alloys Compd.*, vol. 732, pp. 511–517, 2018.

[26] H. Chen *et al.*, "Crystalline SnO2 @ amorphous TiO2 core-shell nanostructures for high-performance lithium ion batteries," *Electrochim. Acta*, vol. 310, pp. 203–212, 2019.

[27] H. Bi, X. Li, and J. Chen, "Ultrahigh nitrogen-doped carbon / superfine-Sn particles for lithium ion battery anode," *J. Mater. Sci. Mater. Electron.*, 2020.

[28] M. K. Kim, A. Y. Kim, J. Y. Woo, J. C. Lim, B. J. Jeon, and J. K. Lee, "Employment of SnO2:F@Ni3Sn2/Ni nanoclusters composites as an anode material for lithium-ion batteries," *J. Alloys Compd.*, vol. 680, pp. 744–751, 2016.

[29] M. O. Guler *et al.*, "Freestanding nano crystalline Tin@carbon anode electrodes for high capacity Li-ion batteries," *Appl. Surf. Sci.*, vol. 446, pp. 122–130, 2018.

[30] L. Ao *et al.*, "A novel Sn particles coated composite of SnOx/ZnO and N-doped carbon nanofibers as high-capacity and cycle-stable anode for lithium-ion batteries," *J. Alloys Compd.*, vol. 819, no. xxxx, p. 153036, 2020.

[31] L. Li, Z. Yuan, R. Fan, T. Luo, and C. Fan, "Low - temperature synthesis of pyrolytic - PVDF - coated - SnO 2 @ hard carbon nanocomposite anodes for Li - ion batteries," *J. Mater. Sci. Mater. Electron.*, no. 0123456789, 2020.

[32] I. Bezza *et al.*, "Understanding the lithiation/delithiation process in SnP2O7 anode material for lithium-ion batteries," *Electrochim. Acta*, vol. 252, pp. 446–452, 2017.

[33] C. M. Costa, E. Lizundia, and S. Lanceros-Méndez, "Polymers for advanced lithium-ion batteries: State of the art and future needs on polymers for the different battery components," *Prog. Energy Combust. Sci.*, vol. 79, p. 100846, 2020.

[34] H. Popp, M. Koller, M. Jahn, and A. Bergmann, "Mechanical methods for state determination of Lithium-Ion secondary batteries: A review," *J. Energy Storage*, vol. 32, no. September, p. 101859, 2020.

[35] J. Chen, J. Wu, X. Wang, A. Zhou, and Z. Yang, "Research progress and application prospect of solid-state electrolytes in commercial lithium-ion power batteries," *Energy Storage Mater.*, vol. 35, pp. 70–87, 2020.

[36] J. B. Goodenough and K. S. Park, "The Li-ion rechargeable battery: A perspective," *J. Am. Chem. Soc.*, vol. 135, no. 4, pp. 1167–1176, 2013.

[37] C. Liu, Z. G. Neale, and G. Cao, "Understanding electrochemical potentials of cathode materials in rechargeable batteries," *Biochem. Pharmacol.*, vol. 19, no. 2, pp. 109–123, 2016.

[38] H. Flåten Andersen, "New materials for lithium-ion batteries," Würzburg University, 2013.

[39] M. Yang, "Strategies To Improve the Electrochemical Performance of Electrodes For Li-ion Batteries," University of Florida, 2012.

[40] L. Croguennec and M. R. Palacin, "Recent achievements on inorganic electrode materials for lithium-ion batteries," *J. Am. Chem. Soc.*, vol. 137, no. 9, pp. 3140–3156, 2015.

[41] A. Tomaszewska *et al.*, "Lithium-ion battery fast charging: A review," *eTransportation*, vol. 1, p. 100011, 2019.

[42] K. S. Chen, I. Balla, N. S. Luu, and M. C. Hersam, "Emerging Opportunities for Two-Dimensional Materials in Lithium-Ion Batteries," *ACS Energy Lett.*, vol. 2, no. 9, pp. 2026–2034, 2017.

[43] S. Clark, "The Synthesis and Characterisation of High Performance Electrode Materials for Li-ion Batteries," University of Oxford, 2017.

[44] B. Liu *et al.*, "Safety issues and mechanisms of lithium-ion battery cell upon mechanical abusive loading: A review," *Energy Storage Mater.*, vol. 24, no. April, pp. 85–112, 2020.

[45] P. Lyu *et al.*, *Recent advances of thermal safety of lithium ion battery for energy storage*, vol. 31. Elsevier B.V., 2020.

[46] A. Manthiram, "Materials challenges and opportunities of lithium ion batteries," *J. Phys. Chem. Lett.*, vol. 2, no. 3, pp. 176–184, 2011.

[47] C. Liao, "Electrolytes and Additives for Batteries Part I: Introduction and Insights on Cathode Degradation Mechanisms," *eTransportation*, 2020.

[48] J. Zhang, X. Yao, R. K. Misra, Q. Cai, and Y. Zhao, "Progress in electrolytes for beyond-lithium-ion batteries," *J. Mater. Sci. Technol.*, vol. 44, pp. 237–257, 2020.

[49] M. Yuan and K. Liu, "Rational design on separators and liquid electrolytes for safer lithium-ion batteries," *J. Energy Chem.*, vol. 43, pp. 58–70, 2020.

[50] R. Borah, F. R. Hughson, J. Johnston, and T. Nann, "On battery materials and methods," *Mater. Today Adv.*, vol. 6, p. 100046, 2020.

[51] K. Wang *et al.*, "Recent advances and historical developments of high voltage lithium cobalt oxide materials for rechargeable Li-ion batteries," *J. Power Sources*, vol. 460, no. April, p. 228062, 2020.

[52] M. K. Shobana, "Metal oxide coated cathode materials for Li ion batteries - A review," *J. Alloys Compd.*, vol. 802, pp. 477–487, 2019.

[53] P. Guan *et al.*, "Recent progress of surface coating on cathode materials for high-performance lithium-ion batteries," *J. Energy Chem.*, vol. 43, pp. 220–235, 2020.

[54] X. Zhu, J. Tang, H. Huang, T. Lin, and B. Luo, "Hollow structured cathode materials for rechargeable batteries," *Sci. Bull.*, 2019.

[55] Q. Cheng, D. Sun, and X. Yu, "Metal hydrides for lithium-ion battery application: A

review," *J. Alloys Compd.*, vol. 769, pp. 167–185, 2018.

[56] Y. Lu, L. Yu, and X. W. (David) Lou, "Nanostructured Conversion-type Anode Materials for Advanced Lithium-Ion Batteries," *Chem*, vol. 4, no. 5, pp. 972–996, 2018.

[57] L. Zhang and C. Chen, "Electrode materials for lithium ion battery," *Prog. Chem.*, vol. 23, no. 2–3, pp. 275–283, 2011.

[58] A. Eftekhari, "Low voltage anode materials for lithium-ion batteries," *Energy Storage Mater.*, vol. 7, no. January, pp. 157–180, 2017.

[59] H. Yamauchi *et al.*, "Performance of Lithium-Ion Battery with Tin-Phosphate Glass Anode and Its Characteristics," *J. Electrochem. Soc.*, vol. 160, no. 10, pp. A1725–A1730, 2013.

[60] J. Wang, I. D. Raistrick, and R. A. Huggins, "Behavior of some binary lithium alloys as negative electrodes in organic solvent based electrolytes," *J. Electrochem. Soc.*, vol. 133, pp. 475–460, 1986.

[61] A. G. Morachevskii, "Thermodynamic properties and electrochemical studies of lithium-tin alloys," *Russ. J. Appl. Chem.*, vol. 88, no. 7, pp. 1087–1105, 2015.

[62] Z. Edfouf, "Étude de nouveaux matériaux composites de type Si / Sn-Ni / Al / C pour électrode négative de batteries lithium ion," Université Paris-Est, 2011.

[63] Z. Edfouf, M. J. Aragón, B. León, C. P. Vicente, and J. L. Tirado, "Tin phosphate electrode materials prepared by the hydrolysis of tin halides for application in lithium ion battery," *J. Phys. Chem. C*, vol. 113, no. 13, pp. 5316–5323, 2009.

[64] J. G. Lee, D. Son, C. Kim, and B. Park, "Electrochemical properties of tin phosphates with various mesopore ratios," *J. Power Sources*, vol. 172, no. 2, pp. 908–912, 2007.

[65] B. Huang, Z. Pan, X. Su, and L. An, "Tin-based materials as versatile anodes for alkali (earth)-ion batteries," *J. Power Sources*, vol. 395, no. March, pp. 41–59, 2018.

[66] B. M. Azmi, S. M. Hasanaly, and M. Zakaria, "Mesoporous tin phosphate as anode material for lithium-ion cells," *Adv. Mater. Res.*, vol. 545, pp. 175–181, 2012.

[67] Q. Tan *et al.*, "Synthesis of SnO2/graphene composite anode materials for lithium-ion batteries," *Appl. Surf. Sci.*, vol. 485, pp. 314–322, 2019.

[68] K. Wu *et al.*, "SnO2 quantum dots @ 3D sulfur-doped reduced graphene oxides as active and durable anode for lithium ion batteries," *Electrochim. Acta*, vol. 291, pp. 24–30, 2018.

[69] M. Wang, Y. Huang, Y. Zhu, X. Wu, N. Zhang, and H. Zhang, "Binder-free flower-like SnS2 nanoplates decorated on the graphene as a flexible anode for high-performance lithium-ion batteries," *J. Alloys Compd.*, vol. 774, pp. 601–609, 2019.

[70] J. S. Song *et al.*, "Fabrication of multilayer graphene-encapsulated Sn/SnO2 nanocomposite as an anode material for lithium-ion batteries and its electrochemical properties," *Appl. Surf. Sci.*, vol. 481, no. February, pp. 736–740, 2019.

[71] M. Zuo, M. Zhou, D. Hu, F. Gao, S. Dong, and L. Huang, "A novel 3D framework indium phosphite-oxalate based on a pcu-type topology," *J. Solid State Chem.*, vol. 237, pp. 219–224, 2016.

[72] X. Zhang, X. Li, and J. Zhang, "Solvothermal synthesis, crystal structures and characterization of open-framework metal (CoII and MnII) phosphites with helical channels and 16-membered rings," *Inorg. Chem. Commun.*, vol. 84, pp. 77–80, 2017.

[73] F. Hamchaoui *et al.*, "Hydrothermal synthesis, structural and thermal characterizations of three open-framework gallium phosphites," *J. Solid State Chem.*, vol. 255, no. July, pp. 8–12, 2017.

[74] U. C. Chung *et al.*, "Mn(HPO3): A new manganese (II) phosphite with a condensed structure," *J. Solid State Chem.*, vol. 178, no. 9, pp. 2913–2921, 2005.

[75] J. L. Song, C. L. Hu, X. Xu, F. Kong, and J. G. Mao, "Synthesis, crystal structures and properties of lead phosphite compounds," *J. Solid State Chem.*, vol. 231, no. 3, pp. 198–203, 2015.

[76] J. L. Song, J. H. Zhang, and J. G. Mao, "Non-noble metal vanadium phosphites with broad absorption for photocatalytic hydrogen evolution," *J. Solid State Chem.*, vol. 237, pp. 371–377, 2016.

[77] Y. K. Han, J. Yoo, and T. Yim, "Distinct reaction characteristics of electrolyte additives for high-voltage lithium-ion batteries: Tris(trimethylsilyl) phosphite, borate, and phosphate," *Electrochim. Acta*, vol. 215, pp. 455–465, 2016.

[78] Z. D. Li *et al.*, "Trimethyl phosphite as an electrolyte additive for high-voltage lithium-ion batteries using lithium-rich layered oxide cathode," *J. Power Sources*, vol. 240, pp. 471–475, 2013.

[79] S. Mai *et al.*, "Tris(trimethylsilyl) phosphite as electrolyte additive for high voltage layered lithium nickel cobalt manganese oxide cathode of lithium ion battery," *Electrochim. Acta*, vol. 147, pp. 565–571, 2014.

[80] Z. Zhou *et al.*, "Triphenyl phosphite as an electrolyte additive to improve the cyclic stability of lithium-rich layered oxide cathode for lithium-ion batteries," *Electrochim. Acta*, vol. 216, pp. 44–50, 2016.

[81] T. H. Nam, E. G. Shim, J. G. Kim, H. S. Kim, and S. I. Moon, "Diphenyloctyl phosphate and tris(2,2,2-trifluoroethyl) phosphite as flame-retardant additives for Li-ion cell electrolytes at elevated temperature," *J. Power Sources*, vol. 180, no. 1, pp. 561–567, 2008.

[82] S. S. Zhang, K. Xu, and T. R. Jow, "Tris(2,2,2-trifluoroethyl) phosphite as a co-solvent for nonflammable electrolytes in Li-ion batteries," *J. Power Sources*, vol. 113, pp. 166–172, 2003.

[83] U. Chung *et al.*, "Li1.43[FeII4.43FeIII0.57(HPO3)6] . 1.5H2O: A phosphite oxoanion-based compound with lithium exchange capability and spin-glass magnetic behavior," *Chem. Mater.*, vol. 23, pp. 4317–4330, 2011.

[84] H. Yaghoobnejad Asl and A. Choudhury, "Phosphite as polyanion-based cathode for Li-ion battery: Synthesis, structure, and electrochemistry of LiFe(HPO3)2," *Inorg. Chem.*, vol. 54, no. 13, pp. 6566–6572, 2015.

[85] H. Y. Asl, K. Ghosh, M. P. Vidal Meza, and A. Choudhury, "Li3Fe2(HPO3)3Cl: An electroactive iron phosphite as a new polyanionic cathode material for Li-ion battery," *J. Mater. Chem. A*, vol. 3, no. 14, pp. 7488–7497, 2015.

[86] A. Lallaoui, Z. Edfouf, O. Benabdallah, S. Idrissi, M. Abd-Lefdil, and F. Cherkaoui El Moursli, "New titanium (III) phosphite structure and its application as anode for lithium ion batteries," *Int. J. Hydrogen Energy*, vol. 45, no. 19, pp. 1–9, 2018.

[87] F. Cherkaoui El Moursli, A. Lallaoui, Z. Edfouf, I. Saadoune, and A. L. Mohammed, "Nouveau matériau composite Ti2(HPO3)3/Graphène pour batteries," 2017.

[88] F. Cherkaoui El Moursli, A. Lallaoui, Z. Edfouf, I. Saadoune, and A. L. Mohammed, "Nouveau matériau d'insertion pour batteries rechargeables, le phosphite de titane (III) et de lithium LiTi(HPO3)2," 2019.

[89] J. L. Song, X. R. Zhang, and R. F. Lu, "Facile synthesis of tin phosphite nanosheets via exfoliated bulk crystals: Electronic structure and piezoelectric property," *J. Colloid Interface Sci.*, vol. 475, pp. 192–195, 2016.

[90] C. Mcdonald Robert and Eriks Klaas, "Crystallographic Studies of Tin(I1) Compounds. 2. Structures," *Inorg. Chem.*, vol. 19, pp. 1237–1241, 1980.

[91] H. L. Huang, Y. C. Lai, Y. W. Chiang, and S. L. Wang, "Intrinsic optical properties and divergent doping effects of manganese(II) on luminescence for tin(II) phosphite grown from a deep-eutectic solvent," *Inorg. Chem.*, vol. 51, no. 4, pp. 1986–1988, 2012.

[92] M. Dahbi *et al.*, "Sodium carboxymethyl cellulose as a potential binder for hard-carbon negative electrodes in sodium-ion batteries," *Electrochem. commun.*, vol. 44, pp. 66–69, 2014.

[93] Z. Ma, Y. Lyu, H. Yang, Q. Li, B. Guo, and A. Nie, "Systematic investigation of the Binder's role in the electrochemical performance of tin sulfide electrodes in SIBs," *J. Power Sources*, vol. 401, no. June, pp. 195–203, 2018.

[94] T. C. Nirmale, B. B. Kale, and A. J. Varma, "A review on cellulose and lignin based binders and electrodes: Small steps towards a sustainable lithium ion battery," *Int. J. Biol. Macromol.*, vol. 103, pp. 1032–1043, 2017.

[95] L. Yin *et al.*, "Effects of binders on electrochemical properties of the SnS2nanostructured anode of the lithium-ion batteries," *J. Alloys Compd.*, vol. 698, pp.

828–834, 2017.

[96] G. Liu, X. Shen, K. Ui, L. Wang, and N. Kumagai, “Influence of the binder types on the electrochemical characteristics of tin nanoparticle negative electrode for lithium secondary batteries,” *J. Power Sources*, vol. 217, pp. 108–113, 2012.

[97] L. Wei, C. Chen, Z. Hou, and H. Wei, “Poly (acrylic acid sodium) grafted carboxymethyl cellulose as a high performance polymer binder for silicon anode in lithium ion batteries,” *Sci. Rep.*, vol. 6, no. September 2015, pp. 1–8, 2016.

[98] G. Yang and S. J. Park, “Conventional and microwave hydrothermal synthesis and application of functional materials: A review,” *Materials (Basel).*, vol. 12, no. 7, 2019.

[99] J. B. Felder, “Hydrothermal Synthesis : A Gateway To Metastable Crystals With Unusual Properties,” University of South Carolina, 2018.

[100] Y. X. Gan, A. H. Jayatissa, Z. Yu, X. Chen, and M. Li, “Hydrothermal Synthesis of Nanomaterials,” *J. Nanomater.*, vol. 2020, 2020.

[101] F. Hamchaoui, V. Alonzo, D. Venegas-Yazigi, H. Rebbah, and E. Le Fur, “Six novel transition-metal phosphite compounds, with structure related to yavapaiite: Crystal structures and magnetic and thermal properties of A I[MIII(HPO3)2] (A=K, NH4, Rb and M=V, Fe),” *J. Solid State Chem.*, vol. 198, pp. 295–302, 2013.

[102] W. S. Hummers and R. E. Offeman, “Preparation of Graphitic Oxide,” *J. Am. Chem. Soc.*, vol. 80, no. 6, p. 1339, 1958.

[103] H. Yaghoobnejad Asl and A. Choudhury, “Phosphite as Polyanion-Based Cathode for Li-Ion Battery: Synthesis, Structure, and Electrochemistry of LiFe(HPO3)2,” *Inorg. Chem.*, vol. 54, no. 13, pp. 6566–6572, 2015.

[104] D. B. Xiong *et al.*, “Hydrothermal synthesis, crystal structure and physical properties of a new gadolinium phosphite hydrate,” *Inorganica Chim. Acta*, vol. 362, no. 9, pp. 3013–3018, 2009.

[105] I. A. Courtney, “Electrochemical and In Situ X-Ray Diffraction Studies of the Reaction of Lithium with Tin Oxide Composites,” *J. Electrochem. Soc.*, vol. 144, no. 6, p. 2045, 1997.

[106] I. Bezza *et al.*, "Electrochemical lithiation/delithiation of SnP2O7 observed by in situ XRD and ex situ 7Li/31P NMR, and 119Sn Mössbauer spectroscopy," *Phys. Chem. Chem. Phys.*, vol. 18, no. 15, pp. 10375–10382, 2016.

[107] I. Sandu, T. Brousse, D. M. Schleich, and M. Danot, "The chemical changes occurring upon cycling of a SnO2 negative electrode for lithium ion cell: In situ Mössbauer investigation," *J. Solid State Chem.*, vol. 179, no. 2, pp. 476–485, 2006.

[108] N. Kumar and V. C. Srivastava, "Simple Synthesis of Large Graphene Oxide Sheets via Electrochemical Method Coupled with Oxidation Process," *ACS omega*, vol. 3, no. 8, pp. 10233–10242, Aug. 2018.

[109] J. B. Goodenough, "Evolution of strategies for modern rechargeable batteries," *Acc. Chem. Res.*, vol. 46, pp. 1053–1061, 2013.

[110] P. Pei, K. Wang, and Z. Ma, "Technologies for extending zinc-air battery's cyclelife : A review," *Appl. Energy*, vol. 128, pp. 315–324, 2014.

[111] T. Yang, S. Venkatesan, C. Lien, J. Chang, and J. Zen, "Nafion/lead oxide-manganese oxide combined catalyst for use as a highly efficient alkaline air electrode in zinc-air battery," *Electrochim. Acta*, vol. 56, no. 17, pp. 6205–6210, 2011.

[112] M. Shao, Q. Chang, J. Dodelet, and R. Chenitz, "Recent advances in electrocatalysts for oxygen reduction reaction," *Chem. Rev.*, vol. 116, pp. 3594–3657, 2016.

[113] Y. Wang, N. Zhao, B. Fang, H. Li, X. T. Bi, and H. Wang, "Carbon-supported Pt-based alloy electrocatalysts for the oxygen reduction reaction in polymer electrolyte membrane fuel cells: particle size, shape, and composition manipulation and their impact to activity," *Chem. Rev.*, vol. 115, pp. 3433–3467, 2015.

[114] W. Xia, A. Mahmood, Z. Liang, R. Zou, and S. Guo, "Earth-abundant nanomaterials for oxygen reduction," *Angew. Chemie - Int. Ed.*, vol. 55, pp. 2650–2676, 2016.

[115] Q. Liu, H. Zhang, H. Zhong, S. Zhang, and S. Chen, "N-doped graphene/carbon composite as non-precious metal electrocatalyst for oxygen reduction reaction," *Electrochim. Acta*, vol. 81, pp. 313–320, 2012.

[116] L. Sun *et al.*, "Nitrogen-doped graphene with high nitrogen level via a one-step

hydrothermal reaction of graphene oxide with urea for superior capacitive energy storage," *R. Soc. Chem.*, vol. 2, pp. 4498–4506, 2012.

[117] S. Wang, E. Iyyamperumal, A. Roy, Y. Xue, D. Yu, and L. Dai, "Vertically Aligned BCN Nanotubes as Efficient Metal-Free Electrocatalysts for the Oxygen Reduction Reaction: A Synergetic Effect by Co-Doping with Boron and Nitrogen," *Angew. Chemie Int. Ed.*, vol. 50, no. 49, pp. 11756–11760, Dec. 2011.

[118] J. Shui, M. Wang, F. Du, and L. Dai, "N-doped carbon nanomaterials are durable catalysts for oxygen reduction reaction in acidic fuel cells," *Sci. Adv.*, vol. 1, pp. 1–8, 2015.

[119] M. Zhou, H. Wang, and S. Guo, "Towards high-efficiency nanoelectrocatalysts for oxygen reduction through engineering advanced carbon nanomaterials," *Chem. Soc. Rev.*, vol. 45, pp. 1273–1307, 2016.

[120] C. Zhu, H. Li, S. Fu, and Y. Lin, "Highly efficient nonprecious metal catalysts towards oxygen reduction reaction based on three-dimensional porous carbon nanostructures," *Chem. Soc. Rev.*, vol. 45, pp. 517–531, 2016.

[121] D. Yang, D. Bhattacharjya, S. Inamdar, J. Park, and J. Yu, "Phosphorus-doped ordered mesoporous carbons with different lengths as efficient metal-free electrocatalysts for oxygen reduction reaction in alkaline media," *J. Am. Chem. Soc.*, vol. 134, pp. 16127–16130, 2012.

[122] Y. Xue *et al.*, "Three-dimensional B,N-doped graphene foam as a metal-free catalyst for oxygen reduction reaction," *Phys. Chem. Chem. Phys.*, vol. 15, pp. 12220–12226, 2013.

[123] Y. Jiao, Y. Zheng, M. Jaroniec, and S. Z. Qiao, "Origin of the electrocatalytic oxygen reduction activity of graphene-based catalysts: A roadmap to achieve the best performance," *J. Am. Chem. Soc.*, vol. 136, pp. 4394–4403, 2014.

[124] D. Deng *et al.*, "Iron encapsulated within pod-like carbon nanotubes for oxygen reduction reaction," *Angew. Chemie - Int. Ed.*, vol. 52, pp. 371–375, 2013.

[125] J. Liu, X. Sun, P. Song, Y. Zhang, W. Xing, and W. Xu, "High-performance oxygen

reduction electrocatalysts based on cheap carbon black, nitrogen, and trace iron," *Adv. Mater.*, vol. 25, no. 47, pp. 6879–6883, 2013.

[126] M. Wang, W. Yang, H. Wang, C. Chen, Z. Zhou, and S. Sun, "Pyrolyzed Fe-N-C composite as an efficient non-precious metal catalyst for oxygen reduction reaction in acidic medium," *Am. Chem. Soc. Catal.*, vol. 4, pp. 3928–3936, 2014.

[127] T. Palaniselvam, V. Kashyap, S. N. Bhange, and J. Baek, "Nanoporous graphene enriched with Fe/Co-N active sites as a promising oxygen reduction electrocatalyst for anion exchange membrane fuel cells," *Adv. Funct. Mater.*, vol. 26, pp. 2150–2162, 2016.

[128] M. E. Scofield, H. Liu, and S. S. Wong, "A concise guide to sustainable PEMFCs: Recent advances in improving both oxygen reduction catalysts and proton exchange membranes," *Chem. Soc. Rev.*, vol. 44, pp. 5836–5860, 2015.

[129] Y. Wu *et al.*, "Nitrogen-doped graphene-supported cobalt carbonitride@oxide core-shell nanoparticles as a non-noble metal electrocatalyst for oxygen reduction reaction," *J. Mater. Chem. A*, vol. 3, pp. 1142–1151, 2015.

[130] L. Ye *et al.*, "Recent advances in flexible fiber-shaped metal-air batteries," *Energy Storage Mater.*, vol. 28, no. March, pp. 364–374, 2020.

[131] F. Cheng and J. Chen, "Metal–air batteries: from oxygen reduction electrochemistry to cathode catalysts," *Chem. Soc. Rev.*, vol. 41, no. 6, pp. 2172–2192, 2012.

[132] C. Wang *et al.*, "Recent Progress of Metal–Air Batteries—A Mini Review," *Appl. Sci.*, vol. 9, pp. 1–22, 2019.

[133] Y. Li and J. Lu, "Metal-Air Batteries: Will They Be the Future Electrochemical Energy Storage Device of Choice?," *ACS Energy Lett.*, vol. 2, no. 6, pp. 1370–1377, 2017.

[134] H. F. Wang and Q. Xu, "Materials Design for Rechargeable Metal-Air Batteries," *Matter*, vol. 1, no. 3, pp. 565–595, 2019.

[135] Y. Xue, S. Sun, Q. Wang, Z. Dong, and Z. Liu, "Transition metal oxide based oxygen reduction reaction electrocatalysts for energy conversion systems with aqueous electrolytes," *J. Mater. Chem. A*, vol. 6, no. 23, pp. 10596–10626, 2018.

[136] X. Chen *et al.*, "A review on recent advancement of nano-structured-fiber-based metal-air batteries and future perspective," *Renew. Sustain. Energy Rev.*, vol. 134, no. July, p. 110085, 2020.

[137] M. Zimmermann, "Oxygen Reduction Reaction Mechanism on Glassy Carbon in Aprotic Organic Solvents," Université Grenoble Alpes, 2006.

[138] F. Si *et al.*, *Electrochemical Oxygen Reduction Reaction*. Elsevier B.V., 2014.

[139] X. Wen, Q. Zhang, and J. Guan, "Applications of metal–organic framework-derived materials in fuel cells and metal-air batteries," *Coord. Chem. Rev.*, vol. 409, p. 213214, 2020.

[140] S. Yan, Y. Xue, S. Li, G. Shao, and Z. Liu, "Improving catalytic activity of layered lithium transition metal oxides for oxygen electrode in metal-air batteries," *Int. J. Hydrogen Energy*, vol. 45, no. 3, pp. 1846–1856, 2020.

[141] F. Shi, X. Zhu, and W. Yang, "Micro-nanostructural designs of bifunctional electrocatalysts for metal-air batteries," *Chinese J. Catal.*, vol. 41, no. 3, pp. 390–403, 2020.

[142] Q. Liu, Z. Pan, E. Wang, L. An, and G. Sun, "Aqueous metal-air batteries: Fundamentals and applications," *Energy Storage Mater.*, vol. 27, pp. 478–505, 2020.

[143] S. Yan, Y. Xue, G. Shao, and Z. Liu, "Activity-structure relationship of electrocatalysts derived from lithium cobalt oxides for metal-air batteries," *J. Power Sources*, vol. 478, no. April, p. 228773, 2020.

[144] E. Marini, L. Jörissen, and S. Brimaud, "Rational design of a low-cost, durable and efficient bifunctional oxygen electrode for rechargeable metal-air batteries," *J. Power Sources*, vol. 482, no. September 2020, p. 228900, 2021.

[145] L. Wei *et al.*, "Recent advances of transition metal based bifunctional electrocatalysts for rechargeable zinc-air batteries," *J. Power Sources*, vol. 477, no. July, p. 228696, 2020.

[146] N. Xu, Y. Zhang, T. Zhang, Y. Liu, and J. Qiao, "Efficient quantum dots anchored nanocomposite for highly active ORR/OER electrocatalyst of advanced metal-air

batteries," *Nano Energy*, vol. 57, pp. 176–185, 2019.

[147] A. Mason, "Investigation of oxygen reduction reaction in carbon-based electrocatalysts," University of Nebraska - Lincoln, 2019.

[148] T. Murata, K. Kotsuki, H. Murayama, R. Tsuji, and Y. Morita, "Metal-free electrocatalysts for oxygen reduction reaction based on trioxotriangulene," *Commun. Chem.*, vol. 2, no. 1, p. 45, 2019.

[149] L. Khotseng, "Oxygen Reduction Reaction," in *Electrocatalysts for Fuel Cells and Hydrogen Evolution - Theory to Design*, 2018, p. 27.

[150] B. Chi, X. Zhang, M. Liu, S. Jiang, and S. Liao, "Applications of M/N/C analogue catalysts in PEM fuel cells and metal-air/oxygen batteries: Status quo, challenges and perspectives," *Prog. Nat. Sci. Mater. Int.*, vol. 30, no. 6, pp. 807–814, 2020.

[151] K. S. Novoselov, V. I. Fal′ko, L. Colombo, P. R. Gellert, M. G. Schwab, and K. Kim, "A roadmap for graphene," *Nature*, vol. 490, no. 7419, pp. 192–200, 2012.

[152] R. Raveendran- Nair *et al.*, "Fine Structure Constant Defines Visual Transparency of Graphene," *Science (80-.).*, vol. 320, p. 1308, Jul. 2008.

[153] Y. Zhu *et al.*, "Graphene and Graphene Oxide: Synthesis, Properties, and Applications," *Adv. Mater.*, vol. 22, no. 46, pp. 3906–3924, 2010.

[154] A. Lerf, H. He, M. Forster, and J. Klinowski, "Structure of Graphite Oxide Revisited," *J. Phys. Chem. B*, vol. 102, no. 23, pp. 4477–4482, Jun. 1998.

[155] K. S. Novoselov *et al.*, "Electric field effect in atomically thin carbon films.," *Science (80-.).*, vol. 306, no. 5696, pp. 666–669, Oct. 2004.

[156] L. Grande, V. Chundi, D. Wei, C. Bower, P. Andrew, and T. Ryhänen, "Graphene for energy harvesting/storage devices and printed electronics," *Particuology*, vol. 10, pp. 1–8, Feb. 2012.

[157] A. K. Geim and K. S. Novoselov, "The rise of graphene," *Nat. Mater.*, vol. 6, no. 3, pp. 183–191, 2007.

[158] S. Pei and H.-M. Cheng, "The reduction of graphene oxide," *Carbon N. Y.*, vol. 50, no.

9, pp. 3210–3228, 2012.

[159] S. Cheekati, Y. Xing, Y. Zhuang, and H. Huang, "Lithium Storage Characteristics in Nano- Graphene Platelets," in *Materials Challenges in Alternative and Renewable Energy: Ceramic Transactions*, vol. 224, 2011, pp. 117–127.

[160] W. Cai, Y. Zhu, X. Li, R. D. Piner, and R. S. Ruoff, "Large area few-layer graphene/graphite films as transparent thin conducting electrodes," *Appl. Phys. Lett.*, vol. 95, no. 12, p. 123115, Sep. 2009.

[161] S. V Morozov *et al.*, "Giant Intrinsic Carrier Mobilities in Graphene and Its Bilayer," *Phys. Rev. Lett.*, vol. 100, no. 1, p. 16602, Jan. 2008.

[162] C. Lee, X. Wei, J. W. Kysar, and J. Hone, "Measurement of the elastic properties and intrinsic strength of monolayer graphene.," *Science (80-.).*, vol. 321, no. 5887, pp. 385–388, Jul. 2008.

[163] K. I. Bolotin *et al.*, "Ultrahigh electron mobility in suspended graphene," *Solid State Commun.*, vol. 146, no. 9, pp. 351–355, 2008.

[164] X. Li *et al.*, "Transfer of Large-Area Graphene Films for High-Performance Transparent Conductive Electrodes," *Nano Lett.*, vol. 9, no. 12, pp. 4359–4363, Dec. 2009.

[165] J. Hou, Y. Shao, M. W. Ellis, R. B. Moore, and B. Yi, "Graphene-based electrochemical energy conversion and storage: fuel cells, supercapacitors and lithium ion batteries," *Phys. Chem. Chem. Phys.*, vol. 13, no. 34, pp. 15384–15402, 2011.

[166] M. D. Stoller, S. Park, Y. Zhu, J. An, and R. S. Ruoff, "Graphene-Based Ultracapacitors," *Nano Lett.*, vol. 8, no. 10, pp. 3498–3502, Oct. 2008.

[167] Q. Wang, W. Hu, and Y. Huang, "Nitrogen doped graphene anchored cobalt oxides efficiently bi-functionally catalyze both oxygen reduction reaction and oxygen revolution reaction," *Int. J. Hydrogen Energy*, vol. 42, no. 9, pp. 5899–5907, 2017.

[168] C. Zhai, M. Sun, M. Zhu, S. Song, and S. Jiang, "A new method to synthesize sulfur-doped graphene as effective metal-free electrocatalyst for oxygen reduction reaction," *Appl. Surf. Sci.*, vol. 407, pp. 503–508, 2017.

[169] T. Domga, G. B. Noumi, M. J. Sieliechi, and J. B. Tchatchueng, "Synthesis of nitrogen and phosphorus co-doped graphene as efficient electrocatalyst for oxygen reduction reaction under strong alkaline media in advanced chlor-alkali cell," *Carbon Trends*, vol. 4, p. 100043, 2021.

[170] X. Liao, X. Wang, C. Huang, and L. Zhu, "Copper-and nitrogen-codoped graphene with versatile catalytic performances for fenton-like reactions and oxygen reduction reaction," *Catalysts*, vol. 10, no. 11, pp. 1–14, 2020.

[171] H. Fredriksson, D. Chakarov, and B. Kasemo, "Patterning of highly oriented pyrolytic graphite and glassy carbon surfaces by nanolithography and oxygen plasma etching," *Carbon N. Y.*, vol. 47, no. 5, pp. 1335–1342, 2009.

[172] X. Z. Yu, C. G. Hwang, C. M. Jozwiak, A. Köhl, A. K. Schmid, and A. Lanzara, "New synthesis method for the growth of epitaxial graphene," *J. Electron Spectros. Relat. Phenomena*, vol. 184, no. 3, pp. 100–106, 2011.

[173] J. Wintterlin and M.-L. Bocquet, "Graphene on metal surfaces," *Surf. Sci.*, vol. 603, no. 10, pp. 1841–1852, 2009.

[174] M. J. Fernández-Merino *et al.*, "Vitamin C Is an Ideal Substitute for Hydrazine in the Reduction of Graphene Oxide Suspensions," *J. Phys. Chem. C*, vol. 114, no. 14, pp. 6426–6432, Apr. 2010.

[175] S. Stankovich *et al.*, "Synthesis of graphene-based nanosheets via chemical reduction of exfoliated graphite oxide," *Carbon N. Y.*, vol. 45, no. 7, pp. 1558–1565, 2007.

[176] G. Wang *et al.*, "Facile Synthesis and Characterization of Graphene Nanosheets," *J. Phys. Chem. C*, vol. 112, no. 22, pp. 8192–8195, Jun. 2008.

[177] Y. Si and E. T. Samulski, "Synthesis of Water Soluble Graphene," *Nano Lett.*, vol. 8, no. 6, pp. 1679–1682, Jun. 2008.

[178] V. Dua *et al.*, "All-organic vapor sensor using inkjet-printed reduced graphene oxide," *Angew. Chem. Int. Ed. Engl.*, vol. 49, no. 12, pp. 2154–2157, Mar. 2010.

[179] Y. Shao, J. Wang, M. Engelhard, C. Wang, and Y. Lin, "Facile and controllable electrochemical reduction of graphene oxide and its applications," *J. Mater. Chem.*,

vol. 20, no. 4, pp. 743–748, 2010.

[180] S. Gurunathan, J. W. Han, V. Eppakayala, and J. H. Kim, "Microbial reduction of graphene oxide by Escherichia coli: A green chemistry approach," *Colloids Surfaces B Biointerfaces*, vol. 102, pp. 772–777, 2013.

[181] S. Gurunathan, J. W. Han, V. Eppakayala, and J. H. Kim, "Green synthesis of graphene and its cytotoxic effects in human breast cancer cells," *Int. J. Nanomedicine*, vol. 8, pp. 1015–1027, 2013.

[182] S. Raveendran *et al.*, "Ecofriendly route for the synthesis of highly conductive graphene using extremophiles for green electronics and bioscience," *Part. Part. Syst. Charact.*, vol. 30, no. 7, pp. 573–578, 2013.

[183] P. Bansal, S. Doshi, A. S. Panwar, and D. Bahadur, "Exoelectrogens Leading to Precise Reduction of Graphene Oxide by Flexibly Switching Their Environment during Respiration," *ACS Appl. Mater. Interfaces*, vol. 7, no. 37, pp. 20576–20584, 2015.

[184] Y. Chen *et al.*, "Microbial reduction of graphene oxide by Azotobacter chroococcum," *Chem. Phys. Lett.*, vol. 677, pp. 143–147, 2017.

[185] O. Akhavan and E. Ghaderi, "Escherichia coli bacteria reduce graphene oxide to bactericidal graphene in a self-limiting manner," *Carbon N. Y.*, vol. 50, no. 5, pp. 1853–1860, 2012.

[186] X. Duan, S. Indrawirawan, H. Sun, and S. Wang, "Effects of nitrogen-, boron-, and phosphorus-doping or codoping on metal-free graphene catalysis," *Catal. Today*, vol. 249, pp. 184–191, 2015.

[187] Z.-S. Wu, S. Yang, Y. Sun, K. Parvez, X. Feng, and K. Müllen, "3D Nitrogen-Doped Graphene Aerogel-Supported Fe3O4 Nanoparticles as Efficient Electrocatalysts for the Oxygen Reduction Reaction," *J. Am. Chem. Soc.*, vol. 134, no. 22, pp. 9082–9085, Jun. 2012.

[188] D. Tomar *et al.*, "ATR-FTIR Spectroscopy and Its Relevance to Probe the Molecular-Level Interactions Between Amino Acids and Metal-Oxide Nanoparticles at Solid/Aqueous Interface," in *Advances in Spectroscopy: Molecules to Materials*, 2019,

pp. 3–21.

[189] Z. Sui, Q.-H. Meng, J.-T. Li, J.-H. Zhu, Y. Cui, and B.-H. Han, "High surface area porous carbons produced by steam activation of graphene aerogels," *J. Mater. Chem. A*, vol. 2, p. 9891, Apr. 2014.

[190] D. Long, W. Li, L. Ling, J. Miyawaki, I. Mochida, and S.-H. Yoon, "Preparation of nitrogen-doped graphene sheets by a combined chemical and hydrothermal reduction of graphene oxide," *Langmuir ACS J. surfaces colloids*, vol. 26, no. 20, pp. 16096–16102, Oct. 2010.

[191] R. Li, Z. Wei, X. Gou, and W. Xu, "Phosphorus-doped graphene nanosheets as efficient metal-free oxygen reduction electrocatalysts," *RSC Adv.*, vol. 3, no. 25, pp. 9978–9984, 2013.

[192] W. Chen, S. Li, C. Chen, and L. Yan, "Self-Assembly and Embedding of Nanoparticles by In Situ Reduced Graphene for Preparation of a 3D Graphene/Nanoparticle Aerogel," *Adv. Mater.*, vol. 23, no. 47, p. 5679, 2011.

[193] C. Cheng *et al.*, "Biopolymer functionalized reduced graphene oxide with enhanced biocompatibility via mussel inspired coatings/anchors," *J. Mater. Chem. B*, vol. 1, no. 3, pp. 265–275, 2013.

[194] M. J. Ju *et al.*, "N-Doped graphene nanoplatelets as superior metal-free counter electrodes for organic dye-sensitized solar cells," *ACS Nano*, vol. 7, no. 6, pp. 5243–5250, 2013.

[195] Y. Xue *et al.*, "Nitrogen-Doped Graphene Foams as Metal-Free Counter Electrodes in High-Performance Dye-Sensitized Solar Cells," *Angew. Chemie Int. Ed.*, vol. 51, no. 48, pp. 12124–12127, Nov. 2012.

[196] M. Sahli, "Synthèse, élaboration et caractérisation des nanocomposites à base de magnésium pour le stockage solide d'hydrogène," Université des Frères Mentouri Constantine, 2015.

[197] M. Maccario, "Caractérisation de nanomatériaux C-LiFePO4 optimisés pour matériaux d'électrode positive pour batteries lithium – ion. Détermination du mécanisme de

désintercalation / intercalation du lithium à partir de cesmatériaux," Université Sciences et Technologies - Bordeaux I, 2007.

[198] N. Bouchaala, "Etude des propriétés structurale et physico- chimique des systèmes Nd-Fe-Co," Université Paris Est, 2017.

[199] M. Termtanun, "Photocatalytic degradation of pesticides using TiO2 nanoparticles," University of Nottingham, 2013.

[200] H. M. Rietveld, "A profile refinement method for nuclear and magnetic structures," *J. Appl. Crystallogr.*, vol. 2, no. 2, pp. 65–71, 1969.

[201] N. Marx, "Synthèse et caractérisation de nouveaux phosphates utilisés comme matériaux d'électrode positive pour batteries au lithium," Université Bordeaux 1, 2010.

[202] A. Salman, "Characterization of normal and malignant cells in culture and human colonic tissues using FTIR microspectroscopy, and advanced computational methods," Ben-Gurion University of the Negev, 2003.

[203] R. De Kloe, "Deformation mechanisms and melt nano-structures in experimentally deformed olivine-orthopyroxene rocks with low melt fractions," Utrecht University, 2001.

[204] I. Z. Jenei, "Scanning Electron Microscopy (SEM) analysis of tribofilms enhanced by fullerene-like nanoparticles," Stockholm University, 2012.

[205] E. Velasco, "Scanning Electron Microscope (SEM) as a means to determine dispersibility," Iowa State University, 2013.

[206] M. Christiaan Verbraeken, "Doped alkaline earth (nitride) hydrides," University of St Andrews, 2009.

[207] L. Bonell, "Thermogravimetric analysis and kinetic study of marine plastic litter," University of Natural Resources and Applied Life Sciences, Vienna, 2017.

[208] H. Stančin, "Samples property identification and study methodology of samples analysis," University of Zagreb, Croatia, 2018.

[209] M. A. Nieradko, "Development of novel anode materials for lithium ion batteries," The

University of Western Ontario, 2016.

[210] P. Reibisch, "Low-dimensional compounds and composites for lithium exchange as well for electronic and for ionic conductivity enhancements," Swiss Federal Institute of Technology in Zürich, 2014.

[211] Z. Guo, "Investigation on cathode materials for lithium-ion batteries," University of Wollongong, 2003.

[212] M. Velický, "Transfer of Small Molecules Across Membrane-Mimetic Interfaces," University of Manchester, England, 2011.

[213] T. Nilsson, "Construction and development of a multifunctional measuring device for biomedical applications," Umeå University, Sweden, 2016.

[214] Y. Uchida, "New Potential Waveforms for Cyclic and Linear-Sweep Voltammetry," University of Oxford, England, 2019.

Appendix 1: Structural and morphological characterization techniques

The prepared materials were characterized using different techniques. The crystallographic structure of the obtained materials is analyzed by X-Ray Diffraction (XRD). Diffraction patterns are analyzed by Rietveld method. The bands vibrations are studied using Fourier Transform Infrared spectroscopy (FTIR) and the morphology is observed by Scanning Electron Microscopy (SEM). Energy Dispersive X-Ray spectroscopy (EDX) is used to analyze the chemical composition of samples. Mass variations associated with phase transitions is measured with ThermoGravimetric Analysis (TGA).

X-Ray Diffraction (XRD)

Principle and measurements

Powder X-Ray Diffraction (XRD) is a characterization method commonly used for the characterization of solids. It allows the identification of crystalline phases present in a material and the determination of their crystallographic characteristics. The principle of this technique consists of the interaction of X-Rays, with the periodic arrangements of crystallized matter. When a monochromatic X-Ray beam of wavelength λ is radiated onto a crystalline material with an angle of incidence θ, the atomic planes (hkl) of the crystal, equidistant of d_{hkl}, will behave like parallel mirrors and reflect the electromagnetic wave, inducing a diffraction phenomenon [196]. Diffracted waves will constructively interfere in certain directions if they are in phase and therefore the diffracted intensity will be non-zero, this is the phase matching condition, known as the Bragg condition [197]:

$$2d_{hkl} \sin \theta_{hkl} = n\lambda$$

λ : Wavelength of incident X-Rays

d_{hkl} : Distance between planes of atoms

θ_{hkl} : Angle of incidence of the X-Rays (Bragg angle)

n : The order of diffraction (integer)

The diffracted intensity is recorded as a function of the 2θ angle of the incident beam and gives rise to a pattern (Intensity Vs 2θ) of diffraction peaks of which correspond to the different families of planes (hkl). This intensity contains essential information on the structural

arrangement, in particular the position of atoms in the lattice and the atomic displacement factors (isotropic or anisotropic) [198].

The diffraction lines of the compound, specific to each crystal structure, indicate the nature of the phases in the compound. From the Bragg relation, the value of d_{hkl} can be deduced to determine the phases present qualitatively, by comparing them with a PDF2-2010 database from the ICCD (International Center for Diffraction Data) using Bruker DIFFRAC plus EVA software.

X-Ray diffraction patterns of the materials were recorded on a Siemens D5000 diffractometer equipped with a copper anticathode X-Ray tube ($\lambda_{k\alpha1}$ = 1.54051 Å and $\lambda_{k\alpha1}$ = 1.54433 Å). The geometry is of the Bragg-Brentano type, and an θ - 2θ assembly is used.

For the preparation of the powder samples, the appropriate amount is grounded in an agate mortar. This allows for a random distribution of the grains in order to avoid that there are preferential orientations that would occur by reinforcement of certain families of diffraction lines. The sample is then placed on a sample holder, its surface is flattened with a glass slide. The sample, placed in the center of the goniometer, rotates at an angle θ, while the detector moves at an angle 2θ, as shown in **Figure appx.1** [199]. The diagrams of the synthesized materials were recorded in the angular domain 2θ = 5° - 60°, with a step size of 0.04° and 30 s per step.

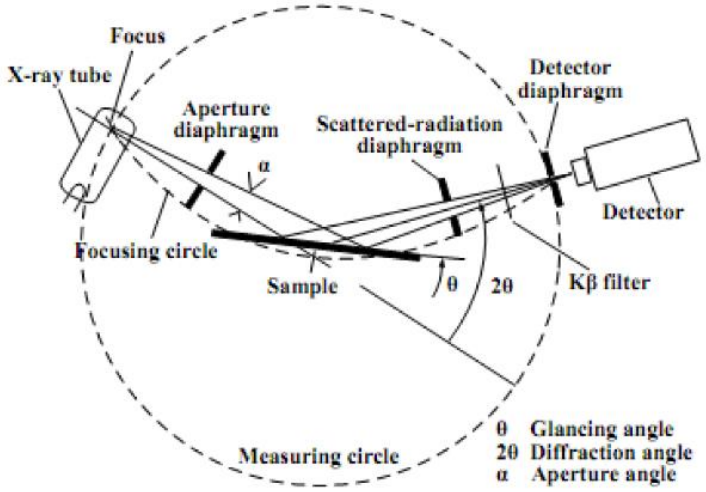

Figure appx.1. Schematic diagram of the working principle of a diffractometer in (θ - 2θ) mode

Rietveld refinement method

The Rietveld refinement, obtained using the Fullprof program, consists in comparing an experimental diffractogram with a theoretical one by the least-squares method. In this method, the difference between the theoretical diagram (calculated from the crystallographic data provided by the user) and the experimental diagram is determined by varying the structural parameters: lattice parameters, positions and occupancy of the atoms and thermal agitation factors.

The equation to minimize during the Rietveld refinement is as follows [200]:

$$\chi^2 = \Sigma\, w_i \left[y_{(\mathrm{exp})\,i} - y_{(calc)\,i}\right]^2$$

$y_{(\mathrm{exp})\,i}$: The experimental intensity at point i

$y_{(calc)\,i}$: The intensity calculated at point i

w_i : The weighting factor assigned to each intensity

Each intensity $y_{(calc)\,i}$ is calculated using the formula:

$$y_{(calc)\,i} = y_{bi} + \Sigma_{\emptyset} S_{\emptyset} \Sigma_k J_{\emptyset k} . L_{P\emptyset k} . \left| F_{\emptyset k} \right|^2 . \Omega_{i\emptyset k}$$

y_{bi} : The intensity of the background noise at point i

$S_{\emptyset}$: The scale factor of phase $\emptyset$ (it allows, among other, to calculate the mass proportions of the different phases)

k : Indexes the reflections h, k and l

$J_{\emptyset k}$: The multiplicity of the reflection k

$L_{P\emptyset k}$: The Lorentz polarization factor

$F_{\emptyset k}$: The structure factor corresponding to the reflection k

$\Omega_{i\emptyset k}$: The profile function responsible for distributing the integrated intensity of the reflection k as a function of 2θ

The agreement between the experimental diffractograms and those calculated is judged by the reliability factors R_{wp} and R_{Bragg} which are defined as follows [201]:

$$R_{wp} = \sqrt{\left[\frac{\sum_i w_i (y_i(obs) - y_i(cal))^2}{\sum_i w_i \, (y_i(obs))^2}\right]} \qquad R_{Bragg} = \frac{\sum_i |I_i(obs) - I_i(cal)|}{\sum_i I_i(obs)}$$

$y_i(obs)$: The observed intensity for an angle 2θi

$y_i(cal)$: The calculated intensity for the 2θi angle

I_i : The integrated intensity of reflection i

Fourier Transform Infrared spectroscopy (FTIR)

Principle and measurements

Fourier Transform Infrared (FTIR) spectroscopy is well known method in identifying chemical structures of various materials. It can also provide quantitative information, such as the concentration of a molecule in a sample. The infrared (IR) wavelength, which is absorbed by the sample depends upon the nature of the covalent bond, the atoms involved, the type of the bonds and the strength of the intermolecular interactions. When the matter absorbs IR radiation, the chemical bonds vibrate resulting in two oscillations types of the atoms. They correspond to the normal modes of vibration: stretching and bending. Stretching is a symmetric or antisymmetric rhythmical movement along the bond axis. The bending vibration occurs when the bond angle between two atoms or movement of a group of atoms might change, relative to the remainder of the molecule. As a result, the obtained FTIR spectra allow measuring complex molecular vibrational modes.

The molecule's absorbance of infrared radiation occurs under certain conditions: the radiation should have energy identical to one of the transitions between the discrete energy levels of the molecule. Moreover, there should be a change in dipole moment [202]. This latter can be written as a Taylor series expansion:

$$\vec{\mathrm{P}} = \vec{\mathrm{P}}_0 + \sum_{\mathrm{k}=1}^{3\mathrm{N}-6} \left[\frac{\partial \vec{\mathrm{P}}}{\partial \mathrm{Q_k}}\right]_0 \mathrm{Q_k}$$

The normal modes of vibrations for molecules with N atoms are given by 3N-5 for linear molecules and 3N – 6 for nonlinear molecules.

Room temperature infrared spectra of the prepared samples were recorded using Jasco FT/IR 4600 Fourier transform spectrophotometer in transmittance mode between 400 cm^{-1} and 4000 cm^{-1}, with a spectral resolution of 4 cm^{-1}.

Scanning Electron Microscopy (SEM)

Principle and measurements

Scanning Electron Microscopy (SEM) is a technique used to investigate the particle sizes and morphologies of the prepared samples. An electron beam is emitted from a tungsten filament cathode and hits the sample surface. The electrons emitted by the beam then interact with the atomic structure of the sample and generate topographic images. Different types of electrons are produced from the beam: backscattered primary electrons, auger electrons and secondary electrons (**Figure appx.2**). Secondary electrons make up the vast majority of the emitted electrons and are the electrons used to form the SEM images. They are generated close to the surface and can gain enough energy to escape from the sample, where they can be collected, thereby providing topological information about the sample. When the secondary electrons reach the detector a current is produced and recorded. The current is plotted against the probe position on the surface of the sample and an image is produced [203].

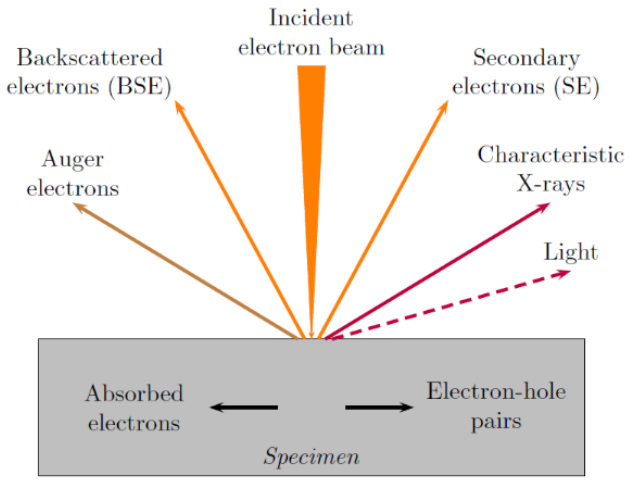

Figure appx.2. The electron interaction with the sample [204]

The contrast in the resultant image is dependent on multiple factors but the most significant is the surface morphology, therefore the image produced can be considered a direct image of the surface structure.

SEM imaging was performed on a JEOL JSM – IT 100 scanning electron microscope operating at an accelerating voltage of 15 kV.

Energy Dispersive X-Ray spectroscopy (EDX)

Energy Dispersive X-Ray spectroscopy (EDX) was carried out to perform the chemical analysis of samples as well as determine the specific location of the elements forming the structure. When a particle is bombarded with an electron beam, several different types of electron emissions are created. Of importance in an EDX analysis, auger electrons and consequently, X-Ray photon or characteristic X-Ray, are emitted from the sample. These X-Rays are produced by the movement of electrons within an atom.

To identify the elements present in a sample, EDX uses pulse height analysis. A detector emits pulses to the sample proportional in height to the characteristic X-Ray energy. Characteristic X-Rays produced from the transition of electrons due to pulses create ionization in the detector which induces an electrical charge. These charges are amplified and then converted into a spectrum using a multichannel pulse-height analyzer. The analyzer measures the energies of the incoming pulses and creates a histogram of the number of occurrences (counts) by energy height. The energy height can be calibrated with 31 references to known X-Ray lines and classified as certain elements. The reflection of secondary electrons is helpful in creating the topographic imagery of a sample [205].

ThermoGravimetric Analysis (TGA)

Principle and measurements

The ThermoGravimetric analysis is a technique, which measures the weight loss of a substance as a function of temperature in a controlled atmosphere and temperature program. Controlled atmosphere is achieved with sample purge gas, which flows over the sample. Purge gas can be inert or reactive. Mass is measured by thermobalance instrument, which has ability of simultaneous weighting and heating of a sample mass in a controlled atmosphere. Temperature range of a typical thermobalance device is from ambient temperature to 1000 - 1600 ºC [206].

Results gained from TGA are represented as a thermogravimetric measured curves. The TGA signal shows changes in the mass of the sample, if it is a stepwise change, and can detect the temperature when the mass loss curve displays specific losses or gains [207].

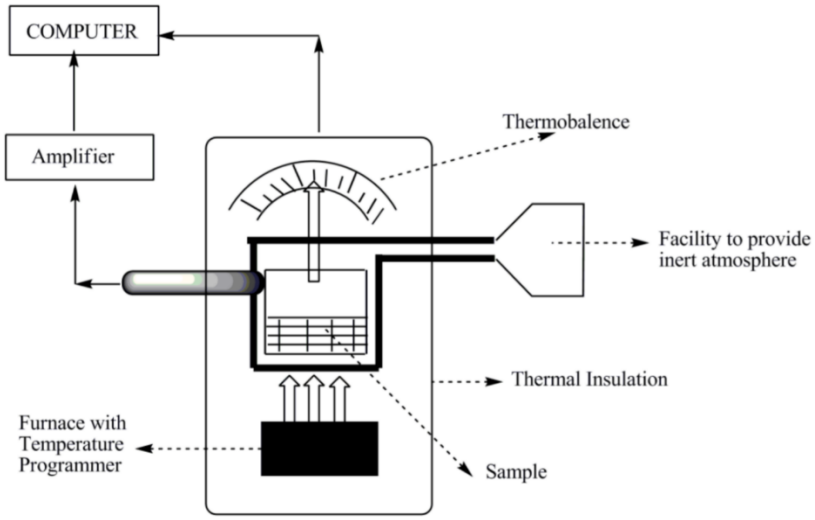

Figure appx.3. Schematic diagram of the working principle and main components of TGA apparatus [208]

This technique also helps confirm the number of water molecules present in a structure. Another advantage is that it makes it possible to determine the percentage by mass of graphene in our prepared composite materials. The TGA measurements were performed with the Labsys TM Evo (1F) Setaram device. The experiments were carried out starting from an initial mass of 15 ± 0.1 mg. The sample is placed in an alumina crucible and heated, under an air flow of 30 mL/min at a rate of 20 °C/min, from room temperature to 900 °C.

The coupling of DSC and TGA signal is advantageous because it measures physical transformation as evaporation, sublimation, drying, the physical property as heat flow, as well as the chemical properties required for the kinetics.

Appendix 2: Electrochemical characterization techniques

Galvanostatic cycling

Galvanostatic cycling is practically useful for simulating the real charge/discharge behavior of battery materials. The cycles involve a constant current being applied to a system while measuring the potential. This analysis allows determining the reversible capacity, the irreversible capacity, the cyclability and the insertion potential of Li^+ ions. When the current is applied, the system undergoes first a discharging (lithiation) step starting from the open-circuit voltage (OCV) and down to the minimum potential. Then, the reverse current is applied and a charging (delithiation) step occurs up to the maximum potential [209]. The current intensity is given by the following relation [210]:

$$I = \frac{Q}{\Delta t} = \frac{C \times m}{\Delta t} = \frac{\frac{F \times n}{M} \times m}{\Delta t}$$

Q : Electrical charge

C : Capacity

m : Mass of active material

F : Faraday Constant

n : Number of electrons exchanged

M : Molar mass of active material

Δt : The time, in hours, required for a full charge or discharge in the chosen potential range, also called the C-Rate.

Cyclic voltammetry (CV)

CV measurements consists of sweeping the potential linearly between two values, V1 and V2 (**Figure appx.4.a**) [147] and the resulting current is measured with a constant scan rate:

$$V = \frac{dE}{dt}$$

In a CV the system first typically sits at its open-circuit potential (OCP). Then a potential is applied between the working-counter electrode couple to sweep the system to more negative potentials. This produces cathodic currents associated with reduction processes occurring at the working electrode. Then the system is swept in the reverse direction to more positive potentials. This produces anodic currents associated with oxidation processes occurring at the working electrode [211]. A typical cyclic voltammogram record for a reversible single electrochemical reaction is shown in **Figure appx.4.b**, where the left-hand side represents reductive potentials and the right-hand side represents oxidative potentials.

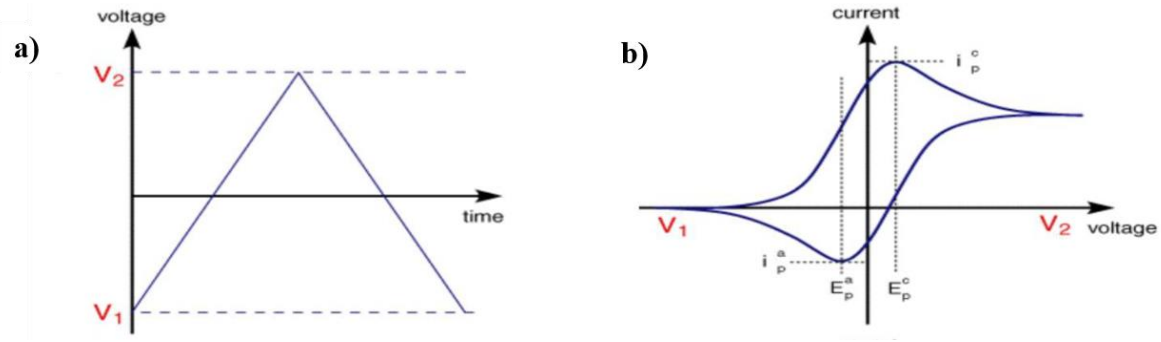

Figure appx.4.a. Graph of electrode voltage potential being swept between V1 and V2 at a constant rate **b.** Graph of electrode current changing with a voltage sweep going from reductive to oxidative and back to reductive potentials [147]

The forward and reverse potential sweeping of the system can be repeated to observe how redox features in the CV change with repeated scanning.

Linear sweep voltammetry (LSV)

Linear sweep voltammetry (LSV) is a voltammetric method where the current at a working electrode is measured, while the potential difference between the working electrode and a reference electrode is swept linearly over time [212].

The experimental apparatus for LSV includes a potentiostat and a three-electrode setup to deliver a potential and monitor the current change. The three-electrode setup consists of a working electrode, a counter electrode, and a reference electrode. The potential is delivered to the system through the working electrode, which is typically an RDE or an RRDE. This electrode is directly connected to the potentiostat, and ORR occurs on the surface of this electrode [213]. As the molecules on the surface of the working electrode are oxidized or

reduced, they move away from the surface. Then, new molecules come into contact with the surface of the working electrode due to diffusion and convection. The flow of electrons into or out of the electrode causes the current. The current is a direct measure of the rate at which electrons are being exchanged through the electrode-electrolyte interface. When this rate becomes higher than the rate at which the oxidizing or reducing species can diffuse from the bulk of the electrolyte to the surface of the electrode, the current reaches a limit, which is represented as a peak in current graphs of the experiment [214].

In LSV, a fixed potential range is determined and the voltage is swept at a constant rate from the lower limit, V1, to the upper limit, V2, in this range as seen in **Figure appx.5**.

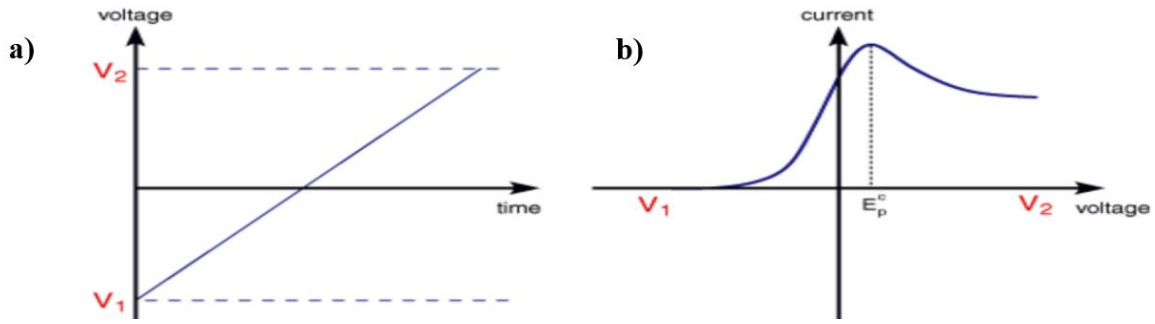

Figure appx.5.a. Graph of electrode voltage potential being swept from V1 to V2 at a constant rate **b.** Graph of electrode current changing with a voltage sweep goes from oxidative to reductive potentials [147]